ESKİŞEHİR TECHNICAL UNIVERSITY
JOURNAL OF SCIENCE AND TECHNOLOGY

A – Applied Sciences and Engineering

Eskişehir Technical University Journal of Science and Technology A - Applied Sciences and Engineering (Other variant title: **Estuscience-Se**) is a peer-reviewed and refereed international journal published by Eskişehir Technical University. Since 2000, it has been regularly published and distributed biannually and it has been published quarterly and only electronically since 2016.

The journal accepts only manuscripts written in English.
The journal issues are published electronically in **March, June**, **September**, and **December**.

Eskişehir Technical University Journal of Science and Technology A - Applied Sciences and Engineering is an international peer-reviewed and refereed journal published by Eskişehir Technical University.

The journal is dedicated to the dissemination of knowledge in applied sciences and engineering disciplines.

The journal aims to publish high quality, original international scientific research articles with specific contributions to the literature in the field of engineering and applied sciences. The journal publishes research papers in the fields of applied science and technology such as Physics, Biology, Mathematics, Statistics, Chemistry and Chemical Engineering, Environmental Sciences and Engineering, Civil Engineering, Earth and Atmospheric Sciences, Electrical and Electronical Engineering, Computer Science and Informatics, Materials Sciences and Engineering, Mechanical Engineering, Mining Engineering, Industrial Engineering, Aeronautics and Astronautics, Pharmaceutical Sciences.

The journal publishes original research articles and special issue articles. All articles are peer-reviewed and the articles that have been evaluated are ensured to meet with researchers as soon as possible.

"Anadolu Üniversitesi Bilim ve Teknoloji Dergisi A - Uygulamalı Bilimler ve Mühendislik (Anadolu University Journal of Science and Technology A - Applied Sciences and Engineering)" published within Anadolu University started to be published within Eskişehir Technical University which was established due to statute law 7141, in 2018. Hence, the name of the journal is changed to " Eskişehir Technical University Journal of Science and Technology A - Applied Sciences and Engineering (Eskişehir Teknik Üniversitesi Bilim ve Teknoloji Dergisi A - Uygulamalı Bilimler ve Mühendislik)".

The Journal's Other Variant Title: **Estusicence-Se;** aproved by ISSN National Centre for Türkiye on April 30, 2024.

Indexed by **ULAKBIM TR Dizin, EBSCO, Copernicus**

EDITOR-IN-CHIEF
Prof. Dr. Harun BÖCÜK
Eskişehir Technical University, Institute of Graduate Programs, 26555 - Eskişehir, TURKEY
Phone: +90 222 213 7470
e-mail: hbocuk@eskisehir.edu.tr

CO-EDITOR IN CHIEF
Prof. Dr. Tahir Hikmet KARAKOÇ
Eskişehir Technical University, Faculty of Aeronautics and Astronautics, 26555 - Eskişehir, TURKEY
Phone: +90 222 213 8466
e-mail: hkarakoc@eskisehir.edu.tr

CO-EDITOR IN CHIEF
Assit. Prof. Dr. Hüseyin Ersin EROL
Eskişehir Technical University, Institute of Graduate Programs, 26555 - Eskişehir, TURKEY
Phone: +90 222-213 7473
e-mail: heerol@eskisehir.edu.tr

CONTACT INFORMATION
Eskişehir Technical Unıversity Journal of Science and Technology
Eskişehir Technical University, Institute of Graduate Programs, 26555 Eskişehir, TURKEY
Phone: +90 222 213 7485
e-mail : btda@eskisehir.edu.tr

ABOUT

Eskişehir Technical University Journal of Science and Technology A - Applied Sciences and Engineering (**Estuscience-Se**) is a peer-reviewed and refereed international journal published by Eskişehir Technical University. Since 2000, it has been regularly published and distributed biannually and it has been published quarterly and only electronically since 2016.

The journal accepts only manuscripts written in English.

The journal issues are published electronically in **MARCH, JUNE, SEPTEMBER**, and **DECEMBER.**

AIM AND SCOPE

Eskişehir Technical University Journal of Science and Technology A - Applied Sciences and Engineering is an international peer-reviewed and refereed journal published by Eskişehir Technical University.

The journal is dedicated to the dissemination of knowledge in applied sciences and engineering disciplines.

The journal aims to publish high quality, original international scientific research articles with specific contributions to the literature in the field of engineering and applied sciences. The journal publishes research papers in the fields of applied science and technology such as Physics, Biology, Mathematics, Statistics, Chemistry and Chemical Engineering, Environmental Sciences and Engineering, Civil Engineering, Earth and Atmospheric Sciences, Electrical and Electronical Engineering, Computer Science and Informatics, Materials Sciences and Engineering, Mechanical Engineering, Mining Engineering, Industrial Engineering, Aeronautics and Astronautics, Pharmaceutical Sciences.

The journal publishes original research articles and special issue articles. All articles are peer-reviewed and the articles that have been evaluated are ensured to meet with researchers as soon as possible.

PEER REVIEW PROCESS

Manuscripts are first reviewed by the editorial board in terms of its its journal's style rules scientific content, ethics and methodological approach. If found appropriate, the manuscript is then send to at least two renown referees by editor. The decision in line with the referees may be an acceptance, a rejection or an invitation to revise and resubmit. Confidential review reports from the referees will be kept in archive. All submission process manage through the online submission systems.

OPEN ACCESS POLICY

This journal provides immediate open access to its content on the principle that making research freely available to the public supports a greater global exchange of knowledge. Copyright notice and type of licence : **CC BY-NC-ND.**

PRICE POLICY

Eskişehir Technical University Journal of Science and Technology A - Journal of Applied Sciences and Engineering is an English, peer-reviewed, scientific, free of charge open-access-based journal. The author is not required to pay any publication fees or article processing charges (APCs) for peer-review administration and management, typesetting, and open-access. Articles also receive Digital Object Identifiers (DOIs) from the CrossRef organization to ensure they are always available.

ETHICAL RULES
You can reach the Ethical Rules in our journal in full detail from the link below:

https://dergipark.org.tr/en/pub/estubtda/policy

Ethical Principles and Publication Policy

Policy & Ethics
Assessment and Publication

As a peer-reviewed journal, it is our goal to advance scientific knowledge and understanding. We have outlined a set of ethical principles that must be followed by all authors, reviewers, and editors.

All manuscripts submitted to our journals are pre-evaluated in terms of their relevance to the scope of the journal, language, compliance with writing instructions, suitability for science, and originality, by taking into account the current legal requirements regarding copyright infringement and plagiarism. Manuscripts that are evaluated as insufficient or non-compliant with the instructions for authors may be rejected without peer review.

Editors and referees who are expert researchers in their fields assess scientific manuscripts submitted to our journals. A blind peer review policy is applied to the evaluation process. The Editor-in-Chief, if he/she sees necessary, may assign an Editor for the manuscript or may conduct the scientific assessment of the manuscript himself/herself. Editors may also assign referees for the scientific assessment of the manuscript and make their decisions based on reports by the referees. Articles are accepted for publication on the understanding that they have not been published and are not going to be considered for publication elsewhere. Authors should certify that neither the manuscript nor its main contents have already been published or submitted for publication in another journal.

The Journal; Implements the Publication Policy and Ethics guidelines to meet high-quality ethical standards for authors, editors and reviewers:

Duties of Editors-in-Chief and co-Editors

The crucial role of the journal Editor-in-Chief and co-Editors is to monitor and ensure the fairness, timeliness, thoroughness, and civility of the peer-review editorial process. The main responsibilities of Editors-in-Chief are as follows:

• Selecting manuscripts suitable for publication while rejecting unsuitable manuscripts,
• Ensuring a supply of high-quality manuscripts to the journal by identifying important,
• Increasing the journal's impact factor and maintaining the publishing schedule,
• Providing strategic input for the journal's development,

Duties of Editors

The main responsibilities of editors are as follows:

• An editor must evaluate the manuscript objectively for publication, judging each on its quality without considering the nationality, ethnicity, political beliefs, race, religion, gender, seniority, or institutional affiliation of the author(s). Editors should decline any assignment when there is a potential for conflict of interest.
• Editors must ensure the document(s) sent to the reviewers does not contain information of the author(s) and vice versa.
• Editors' decisions should be provided to the author(s) accompanied by the reviewers' comments and recommendations unless they contain offensive or libelous remarks.
• Editors should respect requests (if well reasoned and practicable) from author(s) that an individual should not review the submission.
• Editors and all staff members should guarantee the confidentiality of the submitted manuscript.
• Editors should have no conflict of interest with respect to articles they reject/accept. They must not have a conflict of interest with the author(s), funder(s), or reviewer(s) of the manuscript.
• Editors should strive to meet the needs of readers and authors and to constantly improve the journal.

Duties of Reviewers/Referees

The main responsibilities of reviewers/referees are as follows:

• Reviewers should keep all information regarding papers confidential and treat them as privileged information.
• Reviews should be conducted objectively, with no personal criticism of the author.
• Reviewers assist in the editorial decision process and as such should express their views clearly with supporting arguments.
• Reviewers should complete their reviews within a specified timeframe (maximum thirty-five (35) days). In the event that a reviewer feels it is not possible for him/her to complete the review of the manuscript within a stipulated time, then this information must be communicated to the editor so that the manuscript could be sent to another reviewer.
• Unpublished materials disclosed in a submitted manuscript must not be used in a reviewer's personal research without the written permission of the author. Information contained in an unpublished manuscript will remain confidential and must not be used by the reviewer for personal gain.
• Reviewers should not review manuscripts in which they have conflicts of interest resulting from competitive, collaborative, or other relationships or connections with any of the authors, companies, or institutions connected to the papers.

• Reviewers should identify similar work in published manuscripts that has not been cited by the author. Reviewers should also notify the Editors of significant similarities and/or overlaps between the manuscript and any other published or unpublished material.

Duties of Authors
The main responsibilities of authors are as follows:

• The author(s) should affirm that the material has not been previously published and that they have not transferred elsewhere any rights to the article.
• The author(s) should ensure the originality of the work and that they have properly cited others' work in accordance with the reference format.
• The author(s) should not engage in plagiarism or in self-plagiarism.
• On clinical and experimental humans and animals, which require an ethical committee decision for research in all branches of science;
All kinds of research carried out with qualitative or quantitative approaches that require data collection from the participants by using survey, interview, focus group work, observation, experiment, interview techniques,
Use of humans and animals (including material/data) for experimental or other scientific purposes,
• Clinical studies on humans,
• Studies on animals,
• Retrospective studies in accordance with the law on the protection of personal data, (Ethics committee approval should have been obtained for each individual application, and this approval should be stated and documented in the article.)
Information about the permission (board name, date, and number) should be included in the "Method" section of the article and also on the first/last page.
During manuscript upload, the "Ethics Committee Approval" file should be uploaded to the system in addition to the manuscript file.
In addition, in case reports, it is necessary to include information on the signing of the informed consent/ informed consent form in the manuscript.
• The author(s) should suggest no personal information that might make the identity of the patient recognizable in any form of description, photograph, or pedigree. When photographs of the patient were essential and indispensable as scientific information, the author(s) have received consent in written form and have clearly stated as much.
• The author(s) should provide the editor with the data and details of the work if there are suspicions of data falsification or fabrication. Fraudulent data shall not be tolerated. Any manuscript with suspected fabricated or falsified data will not be accepted. A retraction will be made for any publication which is found to have included fabricated or falsified data.
• The author(s) should clarify everything that may cause a conflict of interests such as work, research expenses, consultant expenses, and intellectual property.
• The author(s) must follow the submission guidelines of the journal.
• The author(s) discover(s) a significant error and/or inaccuracy in the submitted manuscript at any time, then the error and/or inaccuracy must be reported to the editor.
• The author(s) should disclose in their manuscript any financial or other substantive conflicts of interest that might be construed to influence the results or interpretation of their manuscript. All sources of financial support should be disclosed under the heading of "Acknowledgment" or "Contribution".
• The corresponding author(s) must ensure that all appropriate co-authors are not included in the manuscript, that author names are not added or removed and that the authors' address information is not changed after the review begins and that all co-authors see and approve the

final version of the manuscript at every stage of the manuscript. All significant contributors should be listed as co-authors. Other individuals who have participated in significant aspects of the research work should be considered contributors and listed under "Author Contribution".

Cancellations/Returns

Articles/manuscripts may be returned to the authors in order to increase the authenticity and/or reliability and to prevent ethical breaches, and even if articles have been accepted and/or published, they can be withdrawn from publication if necessary. The Editor-in-Chief of the journal has the right to return or withdraw an article/manuscript in the following situations:

• When the manuscript is not within the scope of the journal,
• When the scientific quality and/or content of the manuscript do not meet the standards of the journal and a referee review is not necessary,
• When there is proof of ruling out the findings obtained by the research, (When the article/manuscript is undergoing an assessment or publication process by another journal, congress, conference, etc.,)
• When the article/manuscript was not prepared in compliance with scientific publication ethics,
• When any other plagiarism is detected in the article/manuscript,
• When the authors do not perform the requested corrections within the requested time (maximum twenty-one (21) days),
• When the author does not submit the requested documents/materials/data etc. within the requested time,
• When the requested documents/materials/data etc. submitted by the author are missing for the second time,
• When the study includes outdated data,
• When the authors make changes that are not approved by the editor after the manuscript was submitted,
• When an author is added/removed, the order of the authors is changed, the corresponding author is altered, or the addresses of the authors are changed in the article that is in the evaluation process,
• When a statement is not submitted indicating that approval of the ethics committee permission was obtained for the following (including retrospective studies):
• When human rights or animal rights are violated,

ETHICAL ISSUES
Plagiarism
The use of someone else's ideas or words without a proper citation is considered plagiarism and will not be tolerated. Even if a citation is given, if quotation marks are not placed around words taken directly from other authors' work, the author is still guilty of plagiarism. Reuse of the author's own previously published words, with or without a citation, is regarded as self-plagiarism.

All manuscripts received are submitted to iThenticate®, which compares the content of the manuscript with a database of web pages and academic publications. Manuscripts are judged to be plagiarized or self-plagiarized, based on the iThenticate® report or any other source of information, will be rejected. Corrective actions are proposed when plagiarism and/or self-plagiarism is detected after publication. Editors should analyze the article and decide whether a corrected article or retraction needs to be published.

Open-access theses are considered as published works and they are included in the similarity checks.

iThenticate® report should have a maximum of 11% from a single source, and a maximum of 25% in total.

AUTHOR GUIDELINES

All manuscripts must be submitted electronically.

You will be guided stepwise through the creation and uploading of the various files. There are no page charges. Papers are accepted for publication on the understanding that they have not been published and are not going to be considered for publication elsewhere. Authors should certify that neither the manuscript nor its main contents have already been published or submitted for publication in another journal. We ask a signed copyright to start the evaluation process. After a manuscript has been submitted, it is not possible for authors to be added or removed or for the order of authors to be changed. If authors do so, their submission will be cancelled.

Manuscripts may be rejected without peer review by the editor-in-chief if they do not comply with the instructions to authors or if they are beyond the scope of the journal. After a manuscript has been accepted for publication, i.e. after referee-recommended revisions are complete, the author will not be permitted to make any changes that constitute departures from the manuscript that was accepted by the editor. Before publication, the galley proofs are always sent to the authors for corrections. Mistakes or omissions that occur due to some negligence on our part during final printing will be rectified in an errata section in a later issue.

This does not include those errors left uncorrected by the author in the galley proof. The use of someone else's ideas or words in their original form or slightly changed without a proper citation is considered plagiarism and will not be tolerated. Even if a citation is given, if quotation marks are not placed around words taken directly from another author's work, the author is still guilty of plagiarism. All manuscripts received are submitted to iThenticateR, a plagiarism checking system, which compares the content of the manuscript with a vast database of web pages and academic publications. In the received iThenticateR report; The similarity rate is expected to be below 25%. Articles higher than this rate will be rejected.

Uploading Articles to the Journal

Authors should prepare and upload 2 separate files while uploading articles to the journal. First, the Author names and institution information should be uploaded so that they can be seen, and then (using the additional file options) a separate file should be uploaded with the Author names and institution information completely closed. When uploading their files with closed author names, they will select the "Show to Referee" option, so that the file whose names are closed can be opened to the referees.

Prepatation of Manuscript

Style and Format

Manuscripts should be **single column** by giving one-spaced with 2.5-cm margins on all sides of the page, in Times New Roman font (font size 11). Every page of the manuscript, including the title page, references, tables, etc., should be numbered. All copies of the manuscript should also have line numbers starting with 1 on each consecutive page.

Manuscripts must be upload as word document (*.doc, *.docx vb.). **Please avoid uploading** *texts in *.pdf format.*

Symbols, Units and Abbreviations

Standard abbreviations and units should be used; SI units are recommended. Abbreviations should be defined at first appearance, and their use in the title and abstract should be avoided. Generic names of chemicals should be used. Genus and species names should be typed in italic or, if this is not available, underlined.

Please refer to equations with capitalisation and unabbreviated (e.g., as given in Equation (1)).

Manuscript Content

Articles should be divided into logically ordered and numbered sections. Principal sections should be numbered consecutively with Arabic numerals (1. Introduction, 2. Formulation of problem, etc.) and subsections should be numbered 1.1., 1.2., etc. Do not number the Acknowledgements or References sections. The text of articles should be, if possible, divided into the following sections: Introduction, Materials and Methods (or Experimental), Results, Discussion, and Conclusion.

Title and contact information

The first page should contain the full title in sentence case (e.g., Hybrid feature selection for text classification), the full names (last names fully capitalised) and affiliations (in English) of all authors (Department, Faculty, University, City, Country, E-mail), and the contact e-mail address for the clearly identified corresponding author. The first page should contain the full title, abstract and keywords (both English and Turkish).

Abstract

The abstract should provide clear information about the research and the results obtained, and should not exceed 300 words. The abstract should not contain citations and must be written in Times New Roman font with font size 9.

Keywords

Please provide 3 to 5 keywords which can be used for indexing purposes.

Introduction

The motivation or purpose of your research should appear in the "Introduction", where you state the questions you sought to answer, and then provide some of the historical basis for those questions.

Methods

Provide sufficient information to allow someone to repeat your work. A clear description of your experimental design, sampling procedures, and statistical procedures is especially important in papers describing field studies, simulations, or experiments. If you list a product (e.g., animal food, analytical device), supply the name and location of the manufacturer. Give the model number for equipment used.

Results

Results should be stated concisely and without interpretation.

Discussion

Focus on the rigorously supported aspects of your study. Carefully differentiate the results of your study from data obtained from other sources. Interpret your results, relate them to the results of previous research, and discuss the implications of your results or interpretations.

Conclusion

This should state clearly the main conclusions of the research and give a clear explanation of their importance and relevance. Summary illustrations may be included.

Acknowledgments

Acknowledgments of people, grants, funds, etc. should be placed in a separate section before the reference list. The names of funding organizations should be written in full.

Conflict of Interest Statement

The authors are obliged to present the conflict of interest statement at the end of the article after the acknowledgments section.

CRediT Author Statement

Write the authors' contributions in detail using the specified CRediT notifications. Authors may have contributed in more than one role. The corresponding author is responsible for ensuring that descriptions are accurate and accepted by all authors.

CRediT Notifications	Explanation
Conceptualization	Ideas; formulation or evolution of overarching research goals and aims
Methodology	Development or design of methodology; creation of models
Software	Programming, software development; designing computer programs; implementation of the computer code and supporting algorithms; testing of existing code components

Validation	Verification, whether as a part of the activity or separate, of the overall replication/ reproducibility of results/experiments and other research outputs
Formal analysis	Application of statistical, mathematical, computational, or other formal techniques to analyse or synthesize study data
Investigation	Conducting a research and investigation process, specifically performing the experiments, or data/evidence collection
Resources	Provision of study materials, reagents, materials, patients, laboratory samples, animals, instrumentation, computing resources, or other analysis tools
Data Curation	Management activities to annotate (produce metadata), scrub data and maintain research data (including software code, where it is necessary for interpreting the data itself) for initial use and later reuse
Writing – Original Draft	Preparation, creation and/or presentation of the published work, specifically writing the initial draft (including substantive translation)
Writing – Review & Editing	Preparation, creation and/or presentation of the published work by those from the original research group, specifically critical review, commentary, or revision – including pre-or post-publication stages
Visualization	Preparation, creation and/or presentation of the published work, specifically visualization/ data presentation
Supervision	Oversight and leadership responsibility for the research activity planning and execution, including mentorship external to the core team
Project administration	Management and coordination responsibility for the research activity planning and execution
Funding acquisition	Acquisition of the financial support for the project leading to this publication

References

Writting Style; **AMA; References Writting format** should be used in the reference writing of our journal. If necessary, at this point, the reference writings of the articles published in our article can be examined.

Citations in the text should be identified by numbers in square brackets. The list of references at the end of the paper should be given in order of their first appearance in the text. All authors should be included in reference lists unless there are 10 or more, in which case only the first 10 should be given, followed by 'et al.'. Do not use individual sets of square brackets for citation numbers that appear together, e.g., [2,3,5–9], not [2], [3], [5]–[9]. Do not include personal communications, unpublished data, websites, or other unpublished materials as references,

although such material may be inserted (in parentheses) in the text. In the case of publications in languages other than English, the published English title should be provided if one exists, with an annotation such as "(article in Turkish with an abstract in English)". If the publication was not published with an English title, cite the original title only; do not provide a self-translation. References should be formatted as follows (please note the punctuation and capitalisation):

Journal articles
Journal titles should be abbreviated according to ISI Web of Science abbreviations.
Guyon I, Elisseeff A. An introduction to variable and feature selection. J Mach Learn Res 2003; 3: 1157-1182.

Izadpanahi S, Ozcınar C, Anbarjafari G, Demirel H. Resolution enhancement of video sequences by using discrete wavelet transform and illumination compensation. Turk J Elec Eng & Comp Sci 2012; 20: 1268-1276.

Books
Haupt RL, Haupt SE. Practical Genetic Algorithms. 2nd ed. New York, NY, USA: Wiley, 2004.
Kennedy J, Eberhart R. Swarm Intelligence. San Diego, CA, USA: Academic Press, 2001.

Chapters in books
Poore JH, Lin L, Eschbach R, Bauer T. Automated statistical testing for embedded systems. In: Zander J, Schieferdecker I, Mosterman PJ, editors. Model-Based Testing for Embedded Systems. Boca Raton, FL, USA: CRC Press, 2012. pp. 111-146.

Conference proceedings
Li RTH, Chung SH. Digital boundary controller for single-phase grid-connected CSI. In: IEEE 2008 Power Electronics Specialists Conference; 15–19 June 2008; Rhodes, Greece. New York, NY, USA: IEEE. pp. 4562-4568.

Theses
Boynukalın Z. Emotion analysis of Turkish texts by using machine learning methods. MSc, Middle East Technical University, Ankara, Turkey, 2012.

Tables and Figures
All illustrations (photographs, drawings, graphs, etc.), not including tables, must be labelled "Figure." Figures must be submitted in the manuscript.

All tables and figures must have a caption and/or legend and be numbered (e.g., Table 1, Figure 2), unless there is only one table or figure, in which case it should be labelled "Table" or "Figure" with no numbering. Captions must be written in sentence case (e.g., Macroscopic appearance of the samples.). The font used in the figures should be Times New Roman. If symbols such as ×, μ, η, or ν are used, they should be added using the Symbols menu of Word.

All tables and figures must be numbered consecutively as they are referred to in the text. Please refer to tables and figures with capitalisation and unabbreviated (e.g., "As shown in Figure 2…", and not "Fig. 2" or "figure 2").

The resolution of images should not be less than 118 pixels/cm when width is set to 16 cm. Images must be scanned at 1200 dpi resolution and submitted in jpeg or tiff format. Graphs and diagrams must be drawn with a line weight between 0.5 and 1 point. Graphs and diagrams with

a line weight of less than 0.5 point or more than 1 point are not accepted. Scanned or photocopied graphs and diagrams are not accepted.

Figures that are charts, diagrams, or drawings must be submitted in a modifiable format, i.e. our graphics personnel should be able to modify them. Therefore, if the program with which the figure is drawn has a "save as" option, it must be saved as *.ai or *.pdf. If the "save as" option does not include these extensions, the figure must be copied and pasted into a blank Microsoft Word document as an editable object. It must not be pasted as an image file (tiff, jpeg, or eps) unless it is a photograph.

Tables and figures, including caption, title, column heads, and footnotes, must not exceed 16 × 20 cm and should be no smaller than 8 cm in width. For all tables, please use Word's "Create Table" feature, with no tabbed text or tables created with spaces and drawn lines. Please do not duplicate information that is already presented in the figures.

Article Corrections and Uploading to the System
Authors should upload the desired edits for their articles without destroying or changing the Template file of the article, by selecting and specifying the relevant edits as Colored, and also submit the Clean version of the article in 2 separate files (using the Additional file option if necessary). * In case of submitting a corrected article, a separate File in Reply to the Referees must be prepared and the "Reply to the Referees" option in the Add additional file option should be checked and uploaded. If a separate file is not prepared in response to the referees, the Author will definitely be asked to upload the relevant file again and the evaluation will be in the pending phase.

CONTENTS

RESEARCH ARTICLE

SYNTHESIS AND SPECTROSCOPIC STUDIES OF COPPER(II)/COBALT(III) CYANIDE COMPOUNDS WITH IMIDAZOLE, 1-METHYLIMIDAZOLE, AND 2-METHYLIMIDAZOLE

Güneş Süheyla KÜRKÇÜOĞLU [1], Dursun KARAAĞAÇ [2, *], Seray KEKEÇ [3]

[1] Department of Physics, Faculty of Science, Eskişehir Osmangazi University TR-26040 Eskişehir, Türkiye
gkurkcuo@ogu.edu.tr - 0000-0003-3945-3085

[2] Department of Physics, Faculty of Engineering and Natural Sciences, Bursa Technical University, Bursa, Türkiye
dursun.karaagac@btu.edu.tr - 0000-0003-3504-6765

[3] Department of Physics, Faculty of Science, Eskişehir Osmangazi University TR-26040 Eskişehir, Türkiye
kekecseray@gmail.com - 0000-0001-7777-8257

Abstract

New Cu(II)/Co(III) cyanide compounds, $[Cu_3(L)_4Co_2(CN)_{12}]\cdot nH_2O$, with imidazole and methyl derivatives of imidazole have been synthesized in powder form and analyzed using elemental analyses, vibrational (FT-IR and Raman) spectroscopy, and powder X-ray diffraction (PXRD). The elemental analyses of all compounds for C, H, and N were performed and formulas of the compounds were calculated according to the results obtained. In addition, the phase purity of the compounds was confirmed through powder X-ray diffraction (PXRD) analysis. The results of PXRD patterns and vibrational spectroscopic show that the structural characteristics of Cu-Co-L [L = Imidazole(im), 1-methylimidazole(1-meim), and 2-methylimidazole(2-meim)] compounds are analogous to each other. The spectral properties of the Cu-Co-L compounds were obtained by considering the characteristic peak values of cyanide, imidazole, 1-methylimidazole, and 2-methylimidazole ligands.

1. INTRODUCTION

Imidazole and its derivatives are a group of organic molecules defined by a five-membered ring structure with two nitrogen atoms located at the 1st and 3rd positions. Imidazole has the formula $C_3H_4N_2$, and its structure is aromatic, similar to pyrrole and pyridine, making it a crucial component in many biological molecules, including histidine and biotin [1]. Derivatives of imidazole can have various substituents attached to the ring, which can significantly alter their chemical properties and biological activities [2]. Imidazole, 1-methylimidazole, and 2-methylimidazole ligands coordinate to the cobalt center via the nitrogen atom within the imidazole ring. The position and type of substitution (methyl group) on the imidazole ring affect the electronic properties and steric hindrance, which in turn influence the stability and structure of the resulting compound [3, 4]. The imidazole or its derivatives can coordinate directly to the $[Co(CN)_5]^{2-}$ unit, forming compounds such as $[Co(CN)_5]^{2-}\cdot(L)_n$ where L represents imidazole, 1-methylimidazole, or 2-methylimidazole, and n indicates the number of coordinated ligand molecule [5, 6]. These compounds can exhibit varying magnetic and electronic properties depending on the type of imidazole derivative and its coordination mode [7].

When imidazole or its derivatives form compounds with copper(II) (*e.g.*, [Cu(im)$_n$]$^{2+}$), these copper(II) compounds can further interact with the hexacyanocobaltate(III) ion, [Co(CN)$_6$]$^{3-}$, to form mixed-metal compounds. These compounds often have the general formula [Cu(L)$_n$][Co(CN)$_6$], where L can be imidazole, 1-methylimidazole, or 2-methylimidazole, and n represents the coordination number of the copper(II) ion [8-10]. The coordination of the copper(II) ion to imidazole derivatives can lead to either mononuclear or polynuclear compounds depending on the ligand's steric and electronic properties [11]. The [Co(CN)$_6$]$^{3-}$ anion typically serves as a bridge between the copper(II) centers, which can result in the formation of extended polymeric structures or discrete binuclear species [12].

In imidazole compounds, the position and presence of methyl groups can have significant effects. Methyl groups, being electron-donating groups, can increase the electron density on the nitrogen atom of the imidazole. This can affect the strength of the bond with the coordinating metal ion. When 1-methylimidazole and 2-methylimidazole form compounds with metal ions such as copper(II), the distribution of electrons in the bond structure can change in different ways. Methyl groups can create steric hindrance in the imidazole ring, affecting the coordination geometry and stability of the compound. The difference between 1-methylimidazole and 2-methylimidazole arises from these steric effects appearing in different positions. The position (1 or 2) of the methyl group in the imidazole can change the coordination ability of the nitrogen atom. 1-methylimidazole generally shows stronger binding, while the binding ability of 2-methylimidazole may decrease due to steric hindrance. Methyl groups affect the stability of the compound by changing the steric and electronic properties of the ligand. More bulky and sterically hindered compounds may have lower stability. In the Cu-Co-1meim compound, 1-methylimidazole forms a strong bond and may increase the stability of the compound. However, in the Cu-Co-2meim compound, bonding may become more difficult due to steric hindrance, resulting in lower stability. Cyanide-bridged coordination polymers are being studied for innovative chemical designs because of their magnetic, optical, electrical, catalytic, and biological properties [13-17].

In the literature, the metal compounds utilizing the imidazole ligand and its derivatives have been studied [7, 18-28]. However, specific research on hexacyanometallate(III) compounds with imidazole and its derivatives is scarce [29, 30]. As a continuation of these studies, we present three new copper(II)/cobalt(III) cyanide compounds with im, 1-meim and 2-meim ligands [Cu$_3$(im)$_4$Co$_2$(CN)$_{12}$]·3H$_2$O (Cu-Co-im), [Cu$_3$(1-meim)$_4$Co$_2$(CN)$_{12}$]·6H$_2$O (Cu-Co-1meim) and [Cu$_3$(2-meim)$_4$Co$_2$(CN)$_{12}$]·6H$_2$O (Cu-Co-2meim). In addition, in previous studies, cyanide-bridged compounds with imidazole, 1-methylimidazole and 2-methylimidazole ligands were synthesized and their structural and spectroscopic analyses were performed. However, no study was found on how the changes in methyl groups affect the vibrational wavenumbers in spectroscopic studies. Therefore, the change in vibrational wavenumbers of methyl groups in imidazole derivatives during compound formation was investigated and compared with the compounds found in the literature.

2. EXPERIMENTAL

Copper(II) acetate monohydrate (Cu(CH$_3$COO)$_2$·H$_2$O, Acros, 98%), potassium hexacyanocobaltate(III) (K$_3$[Co(CN)$_6$], Acros, 95%), imidazole (C$_3$N$_2$H$_4$, Sigma Aldrich, 98%), 1-methylimidazole (C$_4$H$_6$N$_2$, Merck, 99%), 2-methylimidazole (C$_4$H$_6$N$_2$, Himedia, 97%), ammonia solution (NH$_4$OH, Merck, 25%) and ethanol (C$_2$H$_5$OH, Merck) were obtained from commercial suppliers and used directly without additional purification. Elemental analyses were conducted at the TÜBİTAK Ankara Test and Analysis Laboratory using a LECO CHNS-932 analyzer. The vibrational spectra of the compounds were obtained using a Perkin Elmer 100 FT-IR and Bruker Senterra Dispersive Raman spectrometer, respectively. PXRD was conducted using a PANalytical Empyrean instrument with Cu-Kα radiation.

The compounds were synthesized as follows;

Synthesis of K₃[Co(CN)₆]

Firstly, 2 mmol (4.80 g) of cobalt(II) chloride hexahydrate was dissolved in 50 ml of distilled water and stirred for 15 minutes. To the stirring solution, 4 mmol (3.00 g) of KCN dissolved in 20 ml of distilled water was added dropwise over 10 minutes. The reddish brown precipitate of cobalt(II) cyanide was filtered through filter paper and washed with 10 ml of cold water and then with acetone. Secondly, the resulting $Co(CN)_2$ was transferred to a 250 ml erlenmeyer flask and a solution of KCN dissolved in 25 ml of distilled water (6.00 g) was added to this solution. Finally, the obtaining dark red potassium hexacyanocobalate(II) {[$K_4Co(CN)_6$]} solution was heated to the boiling point and kept at the boiling point for 10 or 15 minutes. The solution acquired the yellow color of potassium hexacyanocobaltate(III) and was filtered while hot. After a few days at room temperature, yellow crystals of the salt {$K_3[Co(CN)_6]$} were formed.

Synthesis of the Cu-Co-L compounds

1 mmol $K_3[Co(CN)_6]$ (0.332 g) was dissolved in 10 mL of water and 10 mL of ammonia. Then, 1 mmol Cu(II) acetate monohydrate [$Cu(CH_3COO)_2·H_2O$ (0.199 g)] dissolved in 20 mL of water was added to the solution and this solution was stirred for 15 minutes. Finally, 4 mmol ligand [imidazole (0.272 g), 1-methylimidazole (0.328 g) or 2-methylimidazole (0.328 g)] dissolved in 5 mL ethanol and 5 mL water was added dropwise to the mixture and stirred at 50 °C for 4 hours. The solution was filtered and then allowed to stand at room temperature. The synthesis of compounds is illustrated by Figure 1. The compounds were then analyzed for carbon, hydrogen, and nitrogen, yielding the following results: Anal. calc. (%) for [$Cu_3(im)_4Co_2(CN)_{12}$]·3H₂O, $C_{24}H_{22}Co_2Cu_3N_{20}O_3$ (M_W = 947.07 g/mol): C, 30.44; H, 2.34; N, 29.58; found C, 30.65; H, 2.69; N, 29.66; for [$Cu_3(1-meim)_4Co_2(CN)_{12}$]·6H₂O, $C_{28}H_{36}Co_2Cu_3N_{20}O_6$ (M_W = 1057.22 g/mol): C, 31.81; H, 3.43; N, 26.50; found C, 31.50; H, 3.69; N, 26.66; for [$Cu_3(2-meim)_4Co_2(CN)_{12}$]·6H₂O, $C_{28}H_{36}Co_2Cu_3N_{20}O_6$ (M_W = 1057.22 g/mol): C, 31.81; H, 3.43; N, 26.50; found C, 31.10; H, 3.30; N, 26.42.
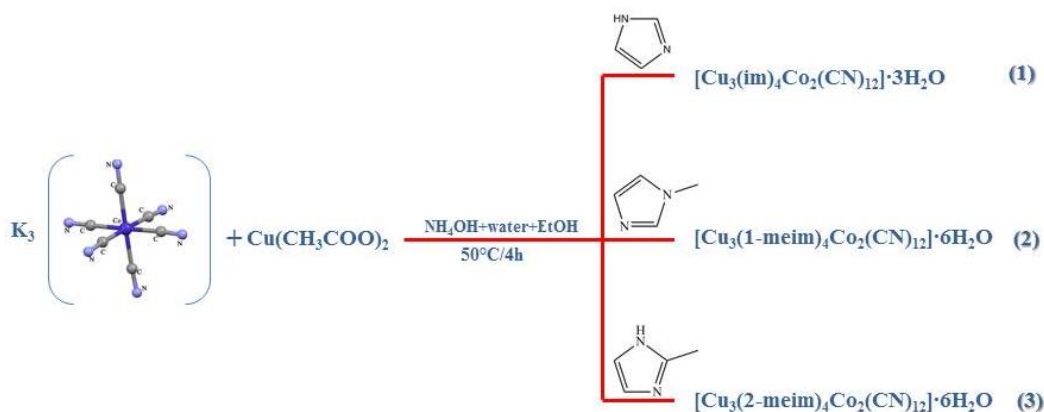
Figure 1. Synthesis scheme of the compounds

3. RESULTS AND DISCUSSION

3.1. Spectral (FT-IR and Raman) Analysis

The vibrational spectra of the compounds can be seen in Figures 2- 4 and are listed in Tables 1-3. As these figures demonstrate, the bands corresponding to the ligands in the vibrational spectra confirm the presence of ligands (im, 1-meim, and 2-meim) within the compounds. Vibrational wavenumbers and assignments for ligands are taken from studies in the literature and are given in Tables 1-3 [31-33]. The

proposed assignments for imidazole are derived from general literature data, and the corresponding values for coordinated ligands are consistent with data reported in the literature [24, 31]. The distinction between ligands is the presence of the CH$_3$ group in meim. Extra bands may appear due to the presence of the CH$_3$ group. In the vibration spectrum of Cu-Co-1meim and Cu-Co-2meim compounds, the absorption bands arising from ν and δ methyl vibrations contain more than the Cu-Co-im compound. In the FTIR and Raman spectra of the Cu-Co-1meim or Cu-Co-2meim compounds, it was observed that the stretching vibration wavenumbers of the methyl groups of the 1-methylimidazole or 2-methylimidazole ligands were shifted to lower or higher wavenumbers, respectively, compared to the methyl groups in the free ligand. These shifts were also observed in other cyanide-bridged compounds such as Cu-Pd-1meim or Cu-Pd-2meim [26, 34].

(a)

(b)
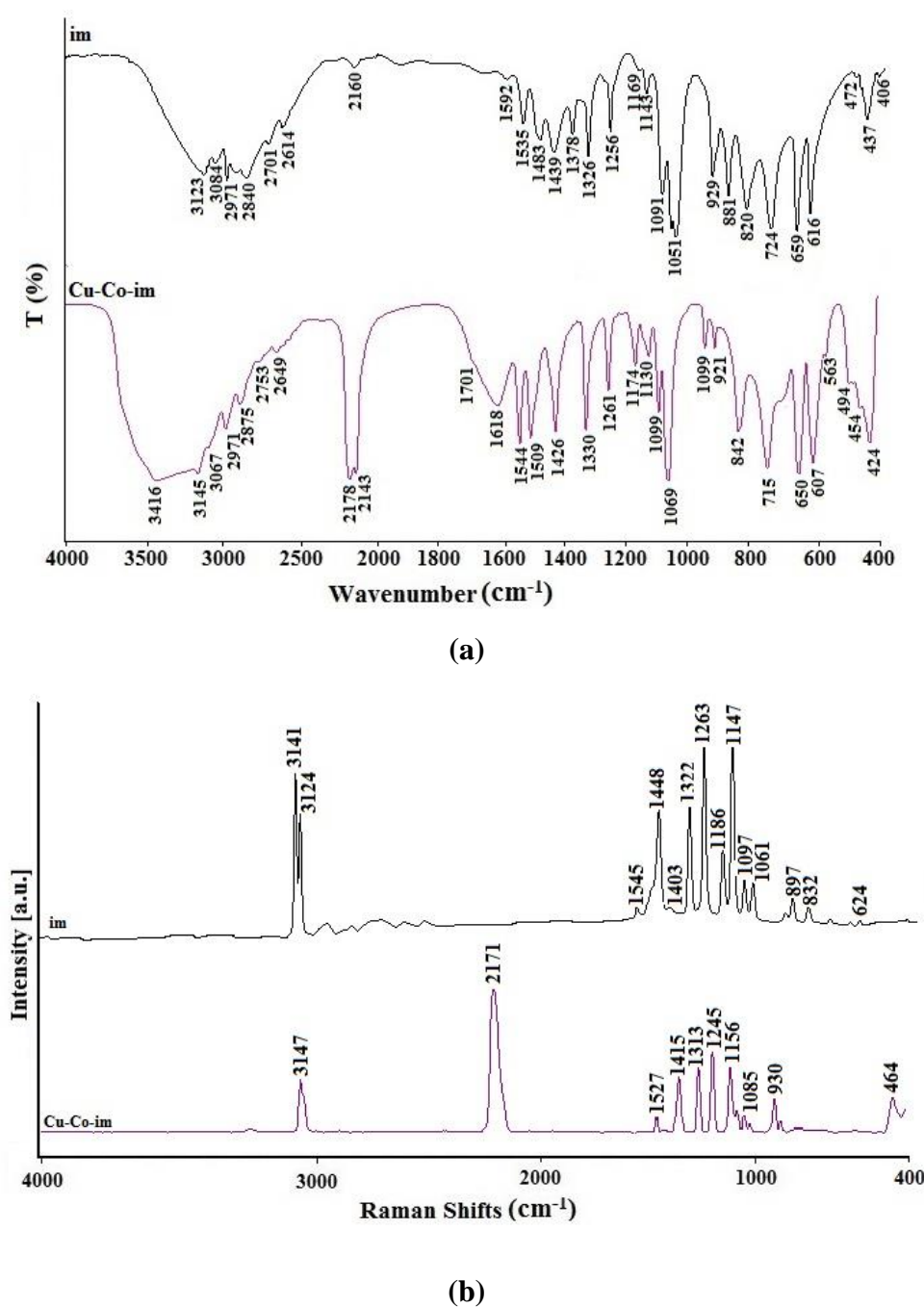
Figure 2. The FT-IR (a) and Raman (b) spectra of the Cu-Co-im compound
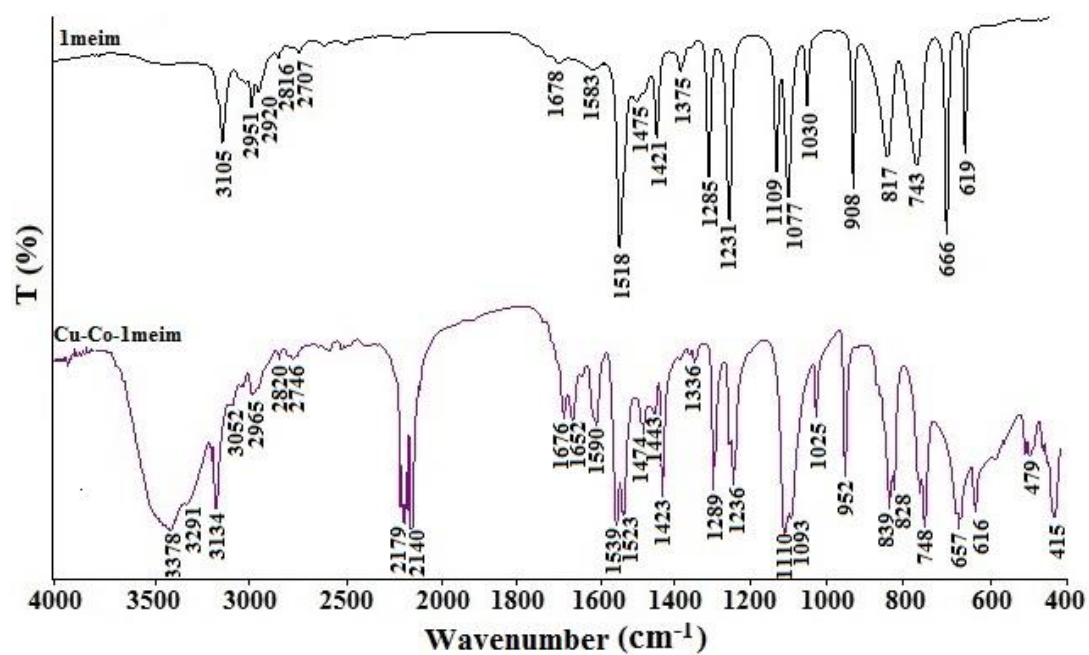
(a)
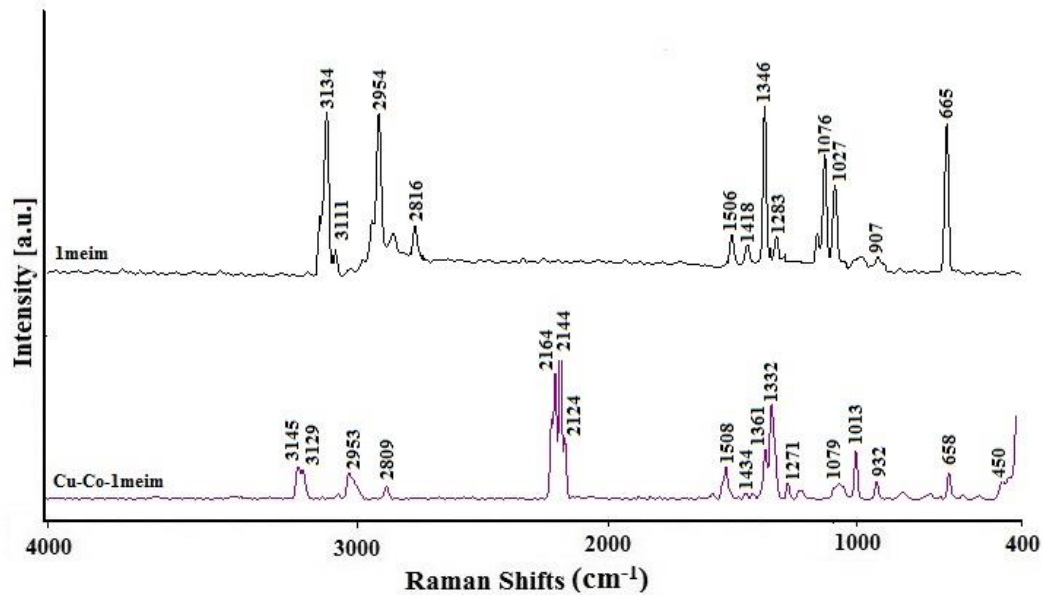
(b)

Figure 3. The FT-IR (a) and Raman (b) spectra of the Cu-Co-1meim compound
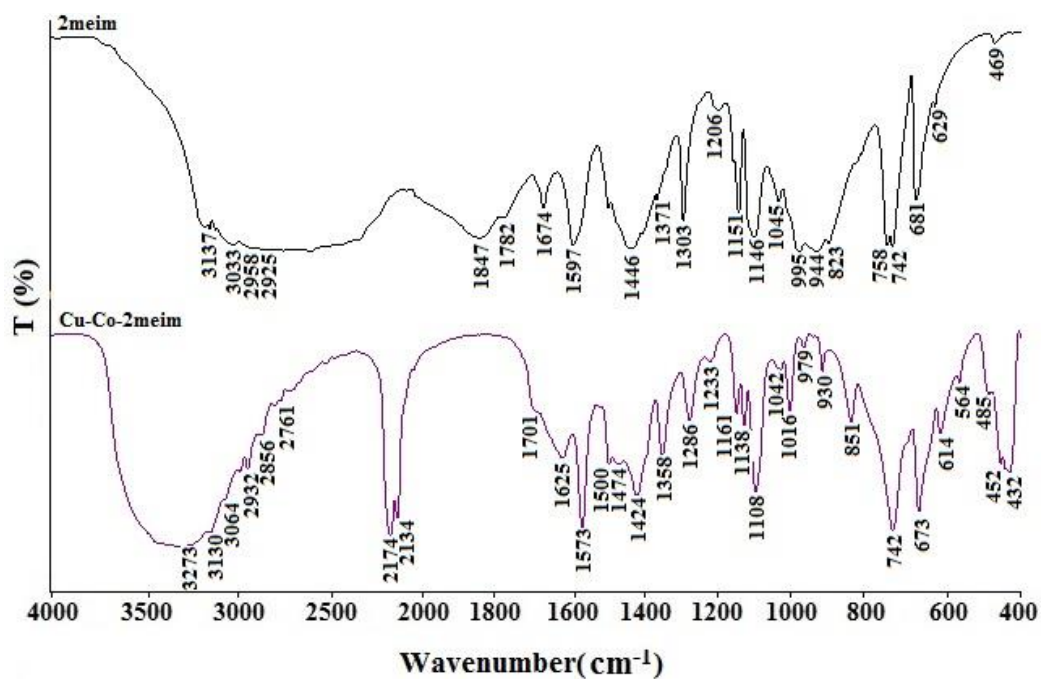
(a)
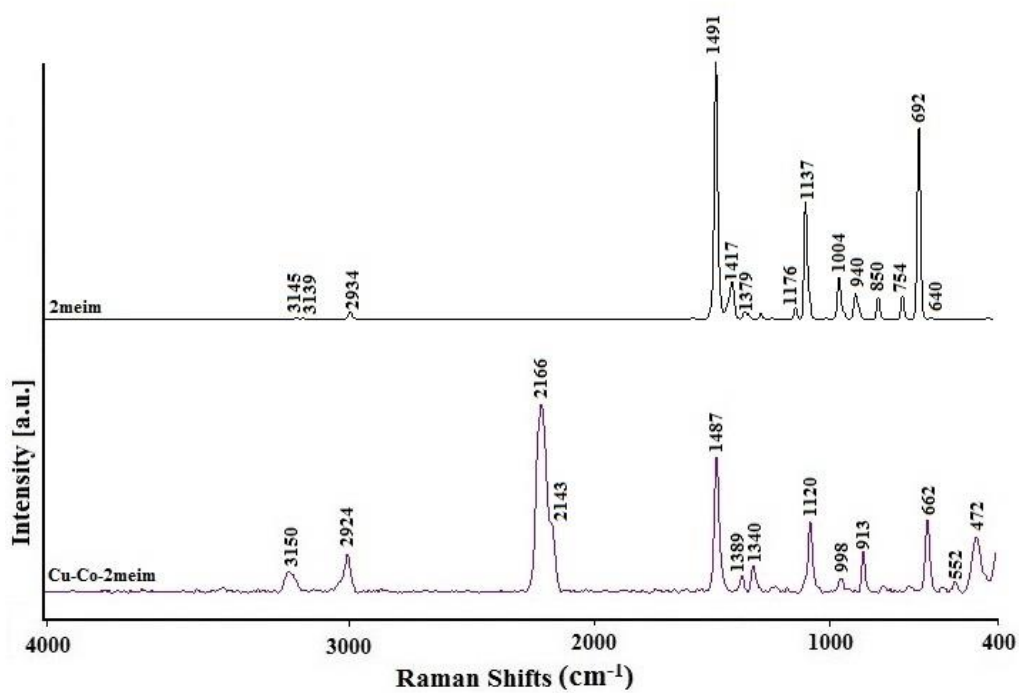
(b)

Figure 4. The FT-IR (a) and Raman (b) spectra of the Cu-Co-2meim compound
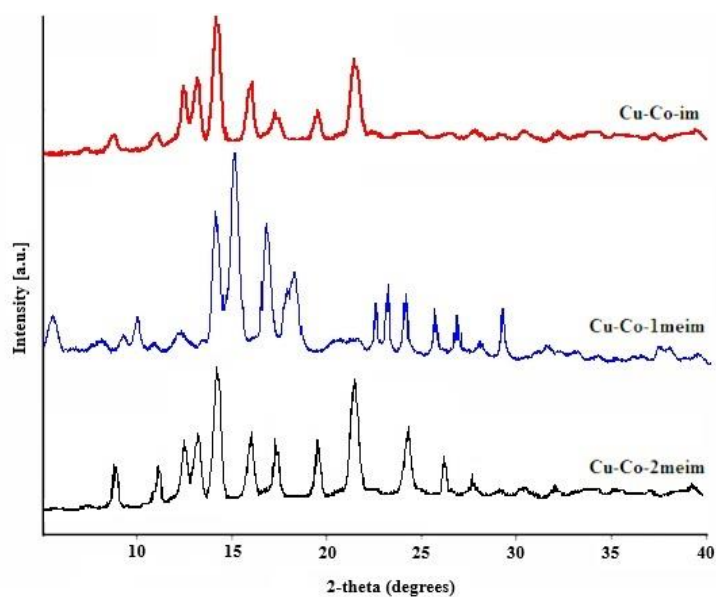
Figure 5. The powder XRD patterns of the compounds

Table 1. The FT-IR and Raman wavenumbers of the imidazole in the compound (cm^{-1})

Assignments [31]	im		Cu-Co-im	
	FT-IR	**Raman**	**FT-IR**	**Raman**
ν(NH)	3123 w	3141 m	3145 w	3147 w
ν(CH)	3048 w	3124 m	3067 sh	3070 vw
ν(CH)	2971 w	-	2971 w	-
ν(CH)	2919 w	-	2875 w	-
δ(NH)	1545 m	1545 w	1544 s	1527 w
δ(CH)	1483 m	-	1426 s	1482 vw
δ(NH)	1439 m	1403 vw	-	1415 m
δ(CH)	1326 m	1322 s	1330 s	1313 m
δ(CH)	1256 m	1263 m	1261 m	1245 m
ν(CN)	1143 m	1147 vs	1174 m	1156 m
ν(CN)	1091 s	1097 m	1099 m	1085 vw
ν(CN)	1051 vs	1061 m	1069 vs	1057 vw
δ_{ring}	929 m	924 vw	951 w	930 w
δ_{ring}	881 m	900 w	842 m	900 vw
γ(CH)	820 m	832 w	-	829 vw
γ(CH)	724 s	746 vw	715 s	738 vw
τ_{ring}	659 s	660 vw	650 vs	675 vw
τ_{ring}	616 s	624 vw	607 s	627 vw
γ(NH)	437 m	-	454 m	464 m

Assignments: ν, stretching; π, out of plane vibration; δ, in- plane vibration; s, strong; m, medium; w, weak; v, very, sh; shoulder.

Table 2. The FT-IR and Raman wavenumbers of the 1-methylimidazole in the compound (cm^{-1})

Assignments [32]	1-meim		Cu-Co-1meim	
	FT-IR	**Raman**	**FT-IR**	**Raman**
ν(CH)	3132 sh	3134 m	3165 w	3145 m
ν(CH)	3106 m	3111 m	3134 s	3129 m
ν(CH)	3025 w	-	3009 w	2994 w
ν(CH$_3$)	2987 w	-	2965 w	-
ν(CH$_3$)	2952 m	2954 m	2950 w	2953 m
ν(NH)	2765 w	-	2746 m	-
ν_{ring}, δ(CH$_3$)	1558 w	-	1590 m	1561 w
ν_{ring}, δ(CH$_3$)	1515 vs	-	1539 vs	-
ν_{ring}, δ(CH$_3$), ν(N-CH$_3$),	1506 w	1506 w	1523 vs	1508 m
δ(CH$_3$), ν_{ring}	1471 w	-	1474 m	1434 w
δ(CH$_3$), ν_{ring}	1420 s	1418 w	1423 s	1406 w
ν_{ring}, δ(CH$_3$)	1383 w	-	-	-
ν_{ring}, δ(CH$_3$)	1358 m	1346 vs	-	1361 m
ν_{ring}, δ(CH$_3$)	1330 w	-	1336 w	1332 s
δ(CH), ν_{ring}	1284 s	1283 w	1289 s	1271 w
ν_{ring}, δ(CH$_3$), ν(N-CH$_3$)	1229 vs	1230 w	1236 s	1226 w
ν(CN)	1107 s	-	1110 vs	1128 vw
ν(CN)	1076 vs	1076 m	1093 vs	1079 w
δ(CH$_3$), ν_{ring}	1028 s	1027 m	1025 m	1013 m
δ_{ring}, ν_{ring}	907 s	907 w	952 s	932 w
γ(CH)	815 s	817 vw	828 s	834 w
γ(CH)	737 s	740 vw	748 s	728 w
ν(N-CH$_3$),ν_{ring}	662 vs	665 m	657 s	658 m
δ_{ring}	615 s	616 w	616 m	601 w

Assignments: ν, stretching; π, out of plane vibration; δ, in- plane vibration; s, strong; m, medium; w, weak; v, very, sh; shoulder.

Table 3. The FT-IR and Raman wavenumbers of the 2-methylimidazole in the compound (cm^{-1})

Assignments [33]	2-meim		Cu-Co-2meim	
	FT-IR	**Raman**	**FT-IR**	**Raman**
ν(CH)	3137 m	3139 vw	3130 s	3137 m
ν(CH)	3110 m	-	-	-
ν(CH)	3033 m	-	3064 sh	3056 vw
ν(CH$_3$)	2958 s	-	2978 s	2989 vw
ν(CH$_3$)	2925 s	2934 w	2932 s	2925 m
ν(NH)	2765 w	-	2761 m	-
ν_{ring}	1597 s	-	1573 s	-
δ(CH$_3$)/ν_{ring}	1446 s	1491 vs	1424 s	1484 s
δ(CH$_3$)	1371 s	1379 w	1358 m	1384 m
ν_{ring}	1303 s	-	1286 m	1343 m
δ(NH)	1154 s	1176 w	1161 m	-
δ(CH)	1114 s	1137 s	1138 m	1122 m
ν(CN)	1091 s	-	1108 s	-
ν(CN)	1051 vs	-	-	-
δ(CH$_3$)	1046 w	-	1042 w	-
ν_{ring} or γ(CH)	995 vs	1004 m	979 w	997 w
γ(NH)	944 s	940 m	930 w	913 m
γ(CH)/δ_{ring}	823 sh	850 m	851 m	836 vw
δ(CH)	758 vs	754 m	742 vs	735 vw
ν(C=C)	681 vs	690 vs	673 vs	665 s
γ_{ring}	629 w	640 vw	-	-
τ_{ring}	616 s	-	614 m	608 w
γ(NH)	469 m	-	452 s	473 m

Assignments: ν, stretching; π, out of plane vibration; δ, in-plane vibration; s, strong; m, medium; w, weak; v, very, sh; shoulder.

From the Tables, it is observed that the vibrational modes of most of the ligands in the compounds have an overall increase in wavenumber compared to the free ligands. These shifts can be attributed to the coupling of Cu-N (im or meim) vibrations. Similar shifts have been noted in imidazole compounds coordinated with metals [24, 35, 36]. In particular, the distinct vibrations mainly related to ν(NH) (3123 cm^{-1} for im), ν(CH) (3048, 2971 and 2919 cm^{-1} for im, 3106 cm^{-1} for 1meim and 3137 cm^{-1} for 2meim), ν(CH$_3$) (2952 cm^{-1} for 1meim and 2958 and 2925 cm^{-1} for 2meim), ν_{ring} (1515 cm^{-1} for 1meim and 1597 cm^{-1} for 2meim), δ(NH) (1545 cm^{-1} for im), δ(CH$_3$) (1358 and 1107 cm^{-1} for 1meim and 1371 and 1046 cm^{-1} for 2meim), ν(CN) (1143, 1091 and 1051 cm^{-1} for im, 1107 and 1076 cm^{-1} for 1meim and 823 cm^{-1} for 2meim), δ_{ring} and ν_{ring} (929 and 881 cm^{-1} for im, 907 cm^{-1} for 1meim, and 1091 and 1051 cm^{-1} for 2meim), ν(C=C) (681 cm^{-1} for 2meim), τ_{ring} (659 and 616 cm^{-1} for im and 616 cm^{-1} for 2meim), and ν(N-CH$_3$) and ν_{ring} (662 cm^{-1} for 1meim) indicate the bonding of the ligand via its nitrogen atom, with significant delocalization of the negative charge across the nitrogen atoms in the ring. In the spectrum of the compounds, these distinct vibrations showed significant upward and downward shifts. These shifts indicate that the ligands coordinate with the copper ion via nitrogen. Similarly, in the cyanide-bridged compounds we previously made with imidazole and its derivatives, coordination to transition metals via the nitrogen in the imidazole ring was observed [23-26].

For these compounds, the ν(C≡N) vibrations contain the most pronounced absorption band. Therefore, the ν(C≡N) vibration peak reveals whether the structure has formed or not. In the FT-IR spectrum for K$_3$[Co(CN)$_6$], ν(C≡N) vibration bands are seen at 2118 cm^{-1} [37]. In the FT-IR spectrum of the K$_3$[Co(CN)$_6$] compound used, the ν(CN) vibration band was observed at 2126 cm^{-1}. The FT-IR spectrum of the compounds contains two distinct cyanide stretching vibrations at 2178 and 2143 cm^{-1} for Cu-Co-im, 2179 and 2140 cm^{-1} for Cu-Co-1meim, and 2174 and 2134 cm^{-1} for Cu-Co-2meim. In addition, one Raman fundamental is assigned to 2171 cm^{-1} for Cu-Co-im, two Raman fundamentals are 2164 and 2144 cm^{-1} for Cu-Co-1meim and 2166 and 2143 cm^{-1} for Cu-Co-2meim. Accordingly, cyanide groups are subject to cleavage in the compounds. In the spectrum of the compounds, the vibration band close to 2126 cm^{-1} indicates the free ν(CN) vibration band, while the higher ν(CN) vibration band indicates the bridge cyanide groups. Therefore, it shows that the cyanide groups are cleaved into two as free and bridge in the compounds. In cyanide-bridged compounds, the frequencies of the bridging cyanide are typically observed at a higher range. This phenomenon is attributed to kinematic coupling, which acts as a mechanical constraint on the bridging cyanide, limiting its movement due to its connection to a second metal center. Considering the shifts observed in the vibrational spectra of the compounds, it is concluded that the imidazole binds to the metal via the nitrogen in its ring, and the cyanides bind to the metals both freely and in a bridging manner.

3.2. Powder X-ray Diffraction (PXRD) Analyses

The PXRD patterns of im, 1-meim or 2-meim hexacyanocobaltate(III) copper(II) compounds are recorded and are given in Figure 5. The PXRD patterns show that the crystal structure is formed and that Cu-Co-im, Cu-Co-1meim, and Cu-Co-2meim structures are obtained in a very pure form. The maximum peaks corresponding to 2θ angles of 13.16°, 13.45°, 14,95°, 16.30°, and 21.56° for Cu-Co-im, 14.03°, 15.78°, 17.24°, and 18.04° for Cu-Co-1meim, and 13.23°, 14.18°, 16.20°, 17.53°, and 21.96° for Cu-Co-2meim indicate the crystal formation and purity. In addition, the element and spectroscopic analysis results prove the accuracy of these expected structures in PXRD patterns.

4. CONCLUSION

In this study, Cu(II) metal compounds containing hexacyanocobaltate(III) with the chemical formulas [Cu$_3$(L)$_4$Co$_2$(CN)$_{12}$]·nH$_2$O were obtained in powder form. Vibrational spectroscopy, powder-XRD and element analysis techniques were used to explain the structures of the compounds. Spectroscopic results showed that the im, 1meim, or 2meim ligands coordinate directly to copper(II) atoms and the cyanide

ligand to cobalt atoms. In addition, cyanide groups were observed to act both freely and as bridges. PXRD determined that the compounds were pure and crystalline. In addition, elemental, spectroscopic, and PXRD data support the similarity in the structural properties of the compounds.

ACKNOWLEDGEMENTS

CONFLICT OF INTEREST

The authors stated that there are no conflicts of interest regarding the publication of this article.

CRediT AUTHOR STATEMENT

Güneş Süheyla Kürkçüoğlu: Writing, Investigation, Supervision, Conceptualization, Original draft. **Dursun Karaağaç:** Investigation, Writing, Draw graph, Drawing a table. **Seray Kekeç:** Writing, Visualization, Draw graph, Drawing a table.

REFERENCES

[1] Gupta P, Gupta JK. Synthesis of bioactive imidazoles: a review. Int J Modern Chem 2015; 7: 60-80.

[2] Andrei GŞ, Andrei BF, Roxana PR. Imidazole derivatives and their antibacterial activity-a mini-review. Mini Rev Med Chem 2021; 21: 1380-1392.

[3] Yang H, Chen J-M, Sun J-J, Yang S-P, Yu J, Tan H, Li W. Syntheses, crystal structures and magnetic properties of three novel cobalt (II) complexes containing imidazole derivative groups. Dalton Trans 2009: 14: 2540-2551.

[4] Sundberg RJ, Martin RB. Interactions of histidine and other imidazole derivatives with transition metal ions in chemical and biological systems. Chem Rev 1974; 74: 471-517.

[5] Johnson CR, Shepherd RE, Marr B, O'Donnell S, Dressick W. Affinities of imidazolate and imidazole ligands for pentacyanoiron (III). J Am Chem Soc 1980; 102: 6227–6235.

[6] Fudulu A, Olar R, Maxim C, Scăeţeanu GV, Bleotu C, Matei L, Chifiriuc MC, Badea M. New cobalt (II) complexes with imidazole derivatives: antimicrobial efficiency against planktonic and adherent microbes and in vitro cytotoxicity features. Molecules 2020; 26: 55

[7] Abu-Dief AM, Abdel-Rahman LH, Abdelhamid AA, Marzouk AA, Shehata MR, Bakheet MA, Almaghrabi OA, Nafady A. Synthesis and characterization of new Cr(III), Fe(III) and Cu(II) complexes incorporating multi-substituted aryl imidazole ligand: Structural, DFT, DNA binding, and biological implications. Spectrochim Acta A Mol Biomol Spectrosc 2020; 228: 117700.

[8] Xie C, Wang W, Zou J-Z, Liu H-L, Shen X-P, Li B-L, Hu H-M, Xu Z. Template self-assembly of cyano-bridged supramolecular complexes {[Cu(en)$_2$][KM(CN)$_6$]}$_n$ (M = Cr(III), Fe(III), Co(III). J Coord Chem 2004; 57: 1519-1527.

[9]   Saha MK, Lloret F, Bernal I. Inter-string arrays of bimetallic assemblies with alternative $Cu^{2+}-Cl-Cu^{2+}$ and $Cu-NC-M$ ($M = Co^{3+}$, Fe^{+3}, Cr^{+3}) bridges: syntheses, crystal structure, and magnetic properties. Inorg Chem 2004; 43: 1969-1975.

[10]   Shiga T, Mishima A, Sugimoto K, Ōkawa H, Oshio H, Ohba M. One-Dimensional 3d–3d–4f trimetallic assemblies consisting of $Cu^{II}_2Ln^{III}$ trinuclear complexes and hexacyanometallate. Eur J Inorg Chem 2012; 2012: 2784-2791.

[11]   Billa E. Synthesis and characterization of mononuclear and dinuclear copper(II) complexes containing sterically hindered polyimidazole ligands: University of Louisville; 1997.

[12]   Machura B, Świtlicka A, Mroziński J, Kalińska B, Kruszynski R. Structural diversity and magnetic properties of thiocyanate copper (II) complexes. Polyhedron 2013; 52: 1276-1286.

[13]   Liu M, Hu J, Wang Y. Synthesis, crystal structure and MMCT of a heterobimetallic cyanide-bridged complex trans-$BrRu^{II}(dppe)_2(\mu\text{-}CN)(Fe^{III}Br_3)$. Polyhedron 2018; 149: 79-83.

[14]   Černák J, Orendáč M, Potočňák I, Chomič J, Orendáčová A, Skoršepa J, Feher A. Cyanocomplexes with one-dimensional structures: preparations, crystal structures and magnetic properties. Coord Chem Rev 2002; 224: 51-66.

[15]   Janiak C. Engineering coordination polymers towards applications. Dalton Trans 2003: 2781-2804.

[16]   Geiss A, Vahrenkamp H. $M(\mu\text{-}CN)Fe(\mu\text{-}CN)M'$ chains with phthalocyanine iron centers: preparation, structures, and isomerization. Inorg Chem 2000; 39: 4029-4036.

[17]   Matiková Maľarová M, Černák J, Matik M, Briančin J, Varret F. Thermal properties of four Co/Fe complexes based on amine-type and cyanido ligands. J Therm Anal Calorim 2019; 136: 703-715.

[18]   Xu H, Zhou B-Y, Yu K, Su Z-H, Zhou B-B, Su Z-M. Copper cyanide polymers with controllable dimensions modulated by rigid and flexible bis-(imidazole) ligands: synthesis, crystal structure and fluorescence properties. Crystengcomm 2019; 21: 1242-1249.

[19]   Ismael M, Abdou A, Abdel-Mawgoud AM. synthesis, characterization, modeling, and antimicrobial activity of Fe^{III}, Co^{II}, Ni^{II}, Cu^{II}, and Zn^{II} complexes based on trisubstituted imidazole ligand. Z Anorg Allg Chem 2018; 644: 1203-1214.

[20]   Huo J, Li H, Yu D, Arulsamy N. Three new metal complexes with imidazole-containing tripodal ligands as fluorophores for nitroaromatics-and ion-selective sensing. Inorg Chim Acta 2020; 502: 119310.

[21]   An B, Yin F, de Voogd NJ, Chen X, Cheng W, Lin W. Chagosendines A–C, New Metal Complexes of Imidazole Alkaloids from the Calcareous Sponge Leucetta chagosensis. Chemistry & Biodiversity 2018; 15: e1700481.

[22]   Kürkçüoğlu GS, Sayın E, Yavuz T, Şahin O. One-dimensional heteronuclear complexes with cyanide and 2-ethylimidazole ligands. Spectrosc Lett 2021; 54: 1-13.

[23] Karaağaç D, Kürkçüoğlu GS. Syntheses and characterizations of the cyanide-bridged heteronuclear polymeric complexes with 2-ethylimidazole. Bull Chem Soc Ethiop 2016; 30: 263-272.

[24] Kürkçüoğlu GS, Yeşilel OZ, Kavlak I, Kurtaran S, Büyükgüngör O. Synthesis, characterization and crystal structure of a novel three-dimensional supramolecular framework containing Ni⋯ π interaction heteronuclear complex: {[Cu(4(5)-Meim)$_4$][Ni(CN)$_4$]·H$_2$O}$_n$. J Inorg Organomet Polym Mater 2009; 19: 314-321.

[25] Kürkçüoğlu GS, Yeşilel OZ, Çaylı İ, Büyükgüngör O. One-and two-dimensional cadmium (II) tetracyanonickelate (II) coordination polymers with imidazole and 2-methylimidazole ligands. J Inorg Organomet Polym Mater 2011; 21: 306-315.

[26] Kürkçüoğlu GS, Gör K, Büyükgüngör O. New cyano bridged heteropolynuclear Cu(II) and Cd(II)-tetracyanopalladate (II) polymeric complexes with 2-methylimidazole ligand. Spectrochim Acta A Mol Biomol Spectrosc 2014; 124: 588-594.

[27] Kürkçüoğlu GS, Sayın E, Şahin O. Cyanide bridged hetero-metallic polymeric complexes: Syntheses, vibrational spectra, thermal analyses and crystal structures of complexes [M(1,2-dmi)$_2$Ni(μ-CN)$_4$]$_n$ (M = Zn(II) and Cd(II)). J Mol Struct 2015; 1101: 82-90.

[28] Mwanza T, Kürkçüoğlu GS, Ünver H, Şahin O, Yeşilel OZ. Synthesis, spectroscopic, structural characterizations, and catalytic properties of cyanide-bridged heteronuclear metal organic frameworks with imidazole. J Solid State Chem 2022; 314: 123344.

[29] Tchouka H. Magnetic and spectroscopic studies of iron and manganese complexes: from molecular materials to catalysis. Chemistry, University of groningen, The netherlands, 2011.

[30] Al Abbas A, Heinrich B, L'Her M, Couzigné E, Welter R, Douce L. Bolaamphiphilic liquid crystals based on bis-imidazolium cations. NJC 2017; 41: 2604-2613.

[31] Majoube M, Vergoten G. Assignment of normal modes for imidazole on the basis of 3-21G and 4-21G Ab Initio Force Fields. J Mol Struct 1992; 266: 345-352.

[32] Sheinker V, Movshovich DY, Osipov OA. Investigation and structure of properties of heterocyclic compounds and their complexes. IV. Calculation and interpretation of the vibrational spectra of N-methylimidazole. Zh Obshch Khim 1973; 43: 2725.

[33] Bellocq AM, Garrigoou-lagrange C. Vibration du méthyl-4(5) imidazole, du méthyl-4(5) imidazole (D)-1, du méthyl-4(5) imidazole (D$_2$)-2,5(4) et du méthyl-4(5) imidazole (D$_3$)-1,2,5(4). J Chim Phys 1969; 66: 1511-1521.

[34] Çaylı İ, Kürkçüoğlu GS, Yeşilel OZ, Şahin O, Büyükgüngör O. C− H⋯ Pd interactions and cyano-bridged heteronuclear polymeric complexes. Polyhedron 2012; 31: 386-394.

[35] Tufan Y, Karacan N, Davies JED. Vibrational spectroscopic investigations of M(imidazole)$_2$Ni(CN)$_4$·2C$_6$H$_{12}$ clathrates. Vib Spectros 2000; 23: 51-55.

[36] Tufan Y. An infrared spectroscopic study on the Hofmann T$_d$-Type clathrates: M(imidazole)$_2$M'(CN)$_4$·2C$_6$H$_6$. J Incl Phenom Macrocycl Chem 2004; 48: 131-134.

[37] Nakagawa I. Far infrared and Raman spectra of $K_3[Co(CN)_6]$ and $[Co(NH_3)_6][Co(CN)_6]$. BCSJ 1973; 46: 3690-3693.

RESEARCH ARTICLE

DETERMINATION OF THE PERFORMANCE OF THE ELECTROCOAGULATION PROCESS IN THE TREATMENT OF WASTEWATER FROM THE CERAMIC INDUSTRY

Esra FINDIK [1, *], Merve SÖZDER [2]

[1] Environmental Engineering, Faculty of Engineering, Eskisehir Technical University, Eskisehir, Turkey
ekacar@eskisehir.edu.tr - 🆔 _0000-0002-4867-9572_

[2] Eskisehir Technical University, Faculty of Engineering, Environmental Engineering, Eskisehir, Turkey
mrvsozder@gmail.com - 🆔 _0009-0006-4252-3573_

Abstract

The ceramic industry produces wastewater containing organic and inorganic pollutants. Traditional treatment methods are costly and complex. Electrocoagulation technology provides an effective treatment by precipitating pollutants through electrochemical reactions. In this thesis, wastewater samples taken from a ceramic factory in Kütahya were treated using the electrocoagulation method. The study considered current densities (1mA/cm², 2mA/cm², 4mA/cm², 10mA/cm²), electrode types (Iron, Aluminum, Iron-Aluminum), and different experiment durations (15 min, 30 min, 45 min, 60 min, 75 min), analyzing turbidity, suspended solids (SS), chemical oxygen demand (COD), and heavy metals. The results of measurements were compared with the Water Pollution Control Regulation (WPCR), showing that the treated wastewater met discharge criteria. When examining the effect of current density and electrode type on treatability, the best removal was found to be at 4 mA/cm² with an iron electrode. Parameters exceeding discharge limits in raw wastewater, such as suspended solids (SS), were reduced by 98.5% at 4 mA/cm² using the iron electrode. The Chemical Oxygen Demand (COD) was diminished by 85.7% at 4 mA/cm² with the iron electrode. For turbidity removal, a 99.94% success rate was achieved using the iron-aluminum electrode at 4 mA/cm². Heavy metal analyses for Zn, Pb, and Cd showed concentrations below WPCR discharge limits. However, in further processed wastewater, the best Pb removal was observed with the iron electrode at 4 mA/cm², and the best Cd removal was achieved with the aluminum electrode at 1 mA/cm². The data obtained were from laboratory-scale experiments, and it is recommended that the method be tested in pilot and full-scale systems. This will permit an evaluation of the efficacy and suitability of the method in actual, real-world contexts.

Abbreviations

WPCR: Water Pollution Control Regulation
SS: Suspended Solids
COD: Chemical Oxygen Demand
EC: Electrocoagulation

*Corresponding Author: ekacar@eskisehir.edu.tr

1. INTRODUCTION

The ceramic industry is a widely active sector in our country, and large amounts of wastewater are generated during ceramic production processes. The direct discharge of wastewater into the receiving environment without prior treatment can result in significant environmental issues. Therefore, the treatment of wastewater generated from production processes using appropriate methods is of significant economic and environmental importance [1].

Electrocoagulation (EC) is an advanced electrochemical treatment method that relies on the production of coagulant agents within the system through electrochemical reactions triggered by electric current passing through electrodes. These coagulants aid in the removal of contaminants by promoting their precipitation. The sludge resulting from the electrocoagulation process is easily settleable and dewaterable. The efficiency of the EC method has been proven, and it is relatively easy to implement. The numerous advantages of electrocoagulation, such as the minimal or negligible need for chemical additives, simple equipment requirements, reduced labor needs, applicability small areas, and lack of secondary pollution, distinguish this method from others. The aforementioned advantages have prompted a surge in research activity pertaining to electrocoagulation in recent years [2].

Within the scope of this study, the state of the ceramic industry in Turkey, its wastewater, production processes, the characteristics of post-process wastewater, environmental impacts, and regulatory requirements were examined. Additionally, experiments were conducted to improve the efficiency of removing discharge parameters from ceramic industry wastewater using the electrocoagulation method. In these experiments, the effects of three main parameters (current density, different experimental durations, and electrode type) on the treatment of ceramic industry wastewater by electrocoagulation were investigated [3].

In order to evaluate the effect of current density on treatment, the system was evaluated using iron, aluminum, and iron-aluminum electrodes at different current densities. The effect of electrode type on the treatment performance was examined using aluminum, iron, and iron-aluminum electrodes at different current densities.

In all the studies conducted, the parameters that must be adhered to in order to comply with discharge limits were measured in the influent waters. These values were then compared with the discharge standards in our country in order to evaluate the applicability of the method. Additionally, the electrical voltage and current intensities applied during the system operation were recorded, and comments were made on the treatability at different energy levels [4].

The electrocoagulation (EC) method has emerged as an effective and economical solution for the treatment of industrial wastewater. Özyonar et al. (2012) investigated the treatability of textile industry wastewater using the EC process and achieved removal efficiencies of up to 83% for total organic carbon (TOC), up to 73% for chemical oxygen demand (COD), up to 98% for color, and up to 99% for turbidity. These results demonstrate the high efficiency of the EC method in removing pollutants from textile wastewater [5].

Emir (2015) reported the removal of over 99% of suspended solids in wastewater from a ceramic factory, as well as high removal rates of heavy metals, including cadmium, zinc, and lead. The study identified iron electrodes and a current density of 1 mA/cm² as the most economical option, highlighting that the use of supporting electrolytes did not offer a cost-effective advantage [6].

In a study on the removal of methylene blue using sequential electrocoagulation and dried banana peel adsorption, it was observed that up to 99% of the colour was removed. The study utilised current densities ranging from 2.5 to 10 mA/cm², with the highest removal observed at 10 mA/cm².

Additionally, the effect of inlet concentration on removal efficiency was examined, and it was found that higher removal efficiency was achieved at lower concentrations. [7].

A study conducted by Camcıoğlu (2016), the effects of the EC method on paper industry wastewater were evaluated, showing a 9.96% increase in COD removal and a 37.49% reduction in energy consumption under controlled conditions [8].

Öztürk (2018) investigated the effects of different electrode types and geometries on the treatment of marble processing wastewater and found that Monopolar Al-Fe electrodes achieved the highest suspended solids removal, while Monopolar Al-Al electrodes provided the highest turbidity removal [9].

In anaother experimental study, the optimal working conditions for decolourisation of a synthetic dye solution with a concentration of 50 mg/L were identified. The experimental conditions, which were found to be optimal, included a current density ranging from 30 to 37.5 mA/cm^2, a conductivity value of 1 mS/cm, and a pH value of 7.5 at 25°C for both Al and Fe electrodes.In addition to these findings, a real textile wastewater sample was examined under conditions analogous to those of the synthetic dye solution, employing a batch EC reactor. The dye removal rate was found to be 80% with real wastewater, with an energy consumption of 9.16 kWh/m^3[10].

Kasaplar et al. (2019) achieved removal efficiencies of 50% COD and 46% suspended solids in the treatment of automotive industry wastewater using the EC method [11].

Öztürk (2019) examined the combination of EC and electrooxidation methods for the electrocatalytic degradation of phenol, achieving over 98% removal of phenol and conversion of by-products to carboxylic acids [12].

Salah et al (2022) investigate the removal of Disperse Blue 3 from aqueous solutions by electrocoagulation with Al and Fe electrodes. The effects of the operation parameters on the process are examined, including the electrocoagulation time, current density, initial pH, salt concentration, the distance between electrodes, and initial dye concentration. The results of the study demonstrated that the removal efficiency of Disperse Blue 3 increased from 22% to 90% when the electrocoagulation time was extended from 5 to 70 minutes, and from 67% to 96% when the electrocoagulation time was decreased from 5 to 60 minutes for Al and Fe, respectively [13].

Akkaya and Üçgül (2023) evaluated the effectiveness of the EC method in treating high dye concentration textile wastewater using solar energy and achieved 92% COD and 95% color removal with a 15-minute process at 1A current. These studies reveal that the EC method offers high efficiency and economic advantages for treating various industrial wastewaters, demonstrating significant potential for environmental sustainability [14].

2. MATERIALS AND METHODS

This study investigated the performance of the electrocoagulation method for the treatment of wastewater from the ceramic industry. The raw wastewater used in the study was obtained from a ceramic factory operating within the boundaries of Kütahya province. The characterization of the wastewater is detailed in Table 1.

Table 1: Initial Measured Values

Parameter	Value
SS	8941,5 mg/L
COD	140,20 mgO$_2$/L
Pb	0,0014 mg/L
Zn	0,1982 mg/L
Cd	-
Ph	8,53
Turbidity	15170 NTU

A Statron power supply, with an input voltage of 220 V, a voltage range of 0-300 V and an output current of 0-4 A, was utilised in the electrocoagulation configuration. Additionally, aluminum, iron, and iron-aluminum electrodes with dimensions of 3.8 x 5.8 cm were employed. The electrodes were connected using insulating serum caps, nuts, rubber seals, washers, and metal plates, and were arranged in a monopolar configuration to ensure that successive electrodes were charged with different loads. A burette stand was used to keep the electrode bundle at a fixed height, and a 600 mL beaker was chosen as the reactor. A magnetic stirrer were used to facilitate mixing within the system as illustrated in Figure 1.

Figure 1. Electrocoagulation Experimental Set-Up

Filter paper, filtration apparatus, and a precision balance were used for the analysis of suspended solids (SS). Samples were dried in an oven and then stored in a desiccator. pH measurements were performed using a Thermo Scientific pH meter, while Chemical Oxygen Demand (COD) analyses were conducted with a thermoreactor and glassware. Metal analyses were carried out using an Agilent 8800 ICP-MS device.

2.1 Determination of the Effect of Electrode Types on Purifiability

In this study on the treatment of ceramic industry wastewater using the electrocoagulation method, comprehensive experiments were conducted to determine the effects of different electrode types on

treatability. The experiments were carried out using various reaction times and current densities, and each combination was repeated with different electrode types. At the end of the experiments, parameters such as suspended solids (SS), turbidity, and chemical oxygen demand (COD) were measured, and treatment efficiencies were calculated. The resulting data were compared with the discharge criteria specified in the Water Pollution Control Regulation (WPCR), and the suitability of the wastewater for discharge into the receiving environment was assessed.

2.2. Determination of the Effect of Test Time on Treatability

The aim of this study is to determine the effect of electrocoagulation (EC) treatment time on treatability. Treatability is typically regarded as a parameter that reflects the effectiveness of chemical and physical processes and directly impacts process efficiency. The contribution of treatment time to this effect is of significant importance, especially regarding the optimization of treatment processes. The objective of this study was to investigate the impact of alternative treatment times using the EC treatment method, and the resulting turbidity, as well as suspended solids (SS), chemical oxygen demand (COD), and heavy metal analysis data at the conclusion of the treatment time, with a view to optimising these factors. The goal is to reveal the changes in treatability and the impact of time on these changes, thereby contributing to the development of more efficient and effective treatment strategies.

2.3. The Effect of Current Density on Purification Performance in the Electrocoagulation Process

In order to gain a detailed understanding of the impact of current density on the efficacy of the electrocoagulation process, different current densities were applied to wastewater from the ceramic industry. The experiments were conducted using iron, aluminum, and iron-aluminum plates with an active area of approximately 100 cm², and current densities of 1, 2, 4, and 10 mA/cm² were employed. This study was conducted to determine and optimize the effects of various current densities on electrocoagulation performance.

3. RESULTS

3.1. Studies on the Performance of Iron Electrodes in the Electrocoagulation Process

- Turbidity Removal Studies: Turbidity experiments were conducted over a duration of 75 minutes. Samples were taken from the wastewater under treatment every 15 minutes, centrifuged for 5 minutes at 5000 rpm, and the turbidity values were then measured and recorded using a turbid meter (Figure 2, Figure 3, Figure 4, and Figure 5). The turbidity removal efficiency of the experiments conducted at different currents using the Fe electrode was calculated to be in excess of 99%. When examining the effect of current density and electrode type on treatability, it was concluded that the best removal was achieved at 4 mA/cm² with the iron electrode. Following a period of analysis, it was determined that a duration of 15 minutes would be adequate for the purposes of this investigation. Salah A.et al found the Fe electrode was found to be more successful than the aluminum electrode[13].
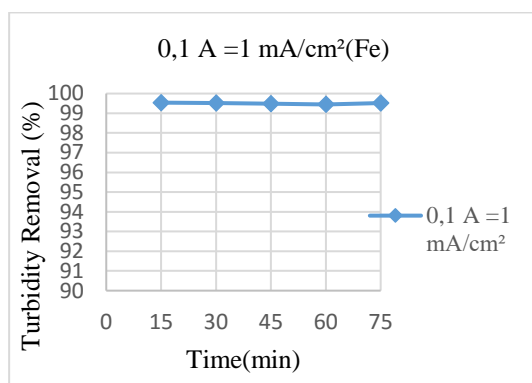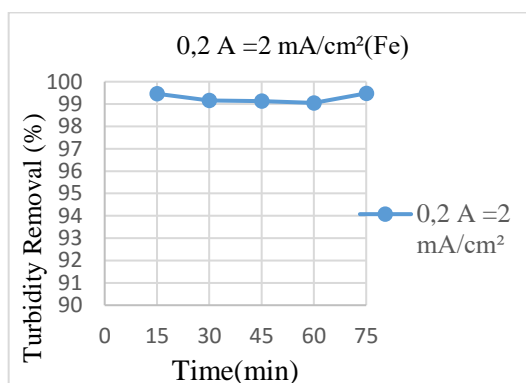
Figure 2. Turbidity values for 0,1A

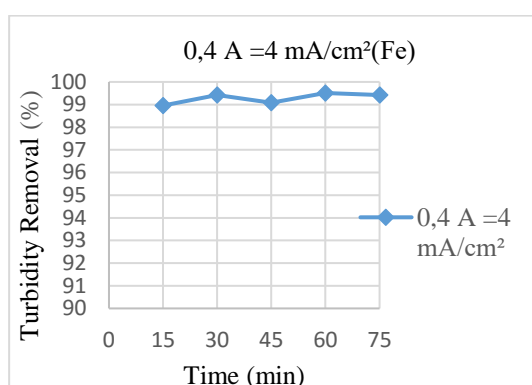**Figure 3.** Turbidity values for 0,2A
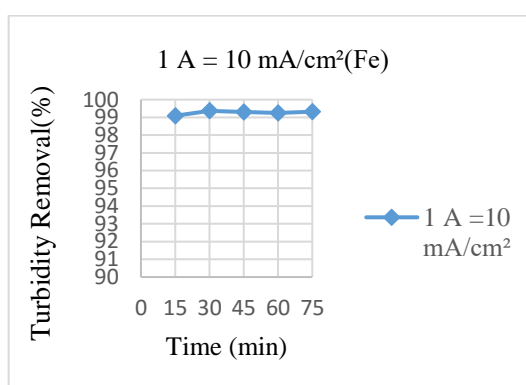

Figure 4. Turbidity values for 0,4A

Figure 5. Turbidity values for 1A

- Suspended Solids Removal Studies: The electrocoagulation process aimed at determining the performance of different electrode types in suspended solids removal was carried out over a duration of 75 minutes. The removal efficiencies achieved with the iron electrode at the end of 75 minutes are as follows (Figure 6). The optimal suspended solids removal was observed at a current of 4 mA/cm², and when the current density attained 10 mA/cm², the efficiency declined from 98.5% to 87%.

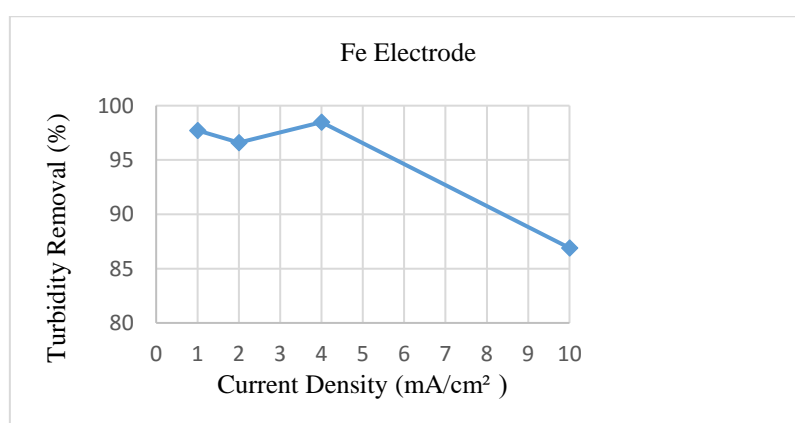**Figure 6.** The Relationship Between Current Density and Suspended Solids Removal Using Iron Electrodes

- Chemical Oxygen Demand (COD) Removal Studies: In the electrocoagulation process conducted with ceramic industry wastewater, samples taken at the 75th minute were acidified and analyzed for Chemical Oxygen Demand (COD). The removal efficiencies achieved with the iron electrode at the end

of 75 minutes are as follows (Figure 7). The optimal COD removal was achieved at a current of 4 mA/cm², with a 86% removal efficiency. When the current density was reduced to 0.1 mA/cm², the efficiency remained at 43%.

Figure 7. The Relationship Between Current Density and Chemical Oxygen Demand (COD) Removal Using Iron Electrodes

3.2. Studies on the Performance of Aluminum Electrodes in the Electrocoagulation Process

- Turbidity Removal Studies: Wastewater samples were processed at different current densities for 75 minutes, with samples taken every 15 minutes and centrifuged. Turbidity values measured with a turbid meter were recorded throughout the experimental period. The turbidity removal efficiency of the experiments conducted at different currents using the Aluminum electrode was calculated to be in excess of 99%. The graphs of turbidity removal efficiencies versus time for experiments conducted with aluminum electrodes at various current densities over 75 minutes are shown below (Figure 8, 9, 10 and 11).
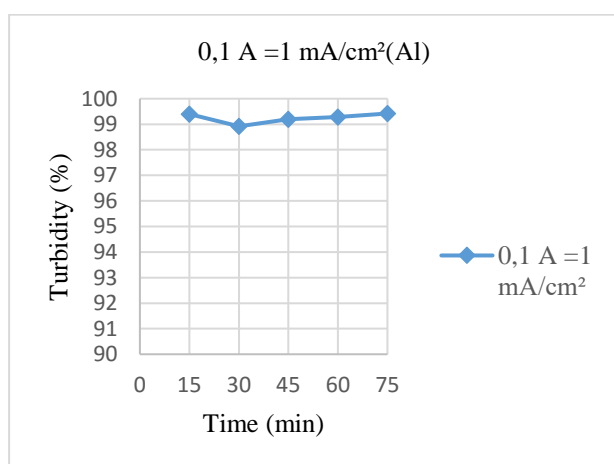
Figure 8. Turbidity values for 0,1A

Figure 9. Turbidity values for 0,2A

Figure 10. Turbidity values for 0,4A	**Figure 11.** Turbidity values for 1A

- Suspended Solids Removal Studies: The electrocoagulation process aimed at determining the performance of different electrode types in suspended solids removal was carried out over a duration of 75 minutes. The removal efficiencies achieved with the aluminum electrode at the end of 75 minutes are as follows (Figure 12). The optimal suspended solids removal was observed at a current of 1 mA/cm², and when the current density attained 0,2 mA/cm², the efficiency declined from 97.9% to 87,8%.

Figure 12. The Relationship Between Current Density and Suspended Solids Removal Using Aluminum Electrodes

-Chemical Oxygen Demand (COD) Removal Studies: In the electrocoagulation process conducted with ceramic industry wastewater, samples taken at the 75th minute were acidified and analyzed for Chemical Oxygen Demand (COD). The removal efficiencies achieved with the aluminum electrode at the end of 75 minutes are as follows (Figure 13). The optimal COD removal was achieved at a current of 0,4 mA/cm², with a 82,7% removal efficiency. When the current density was reduced to 0.1 mA/cm², the efficiency remained at 43%.
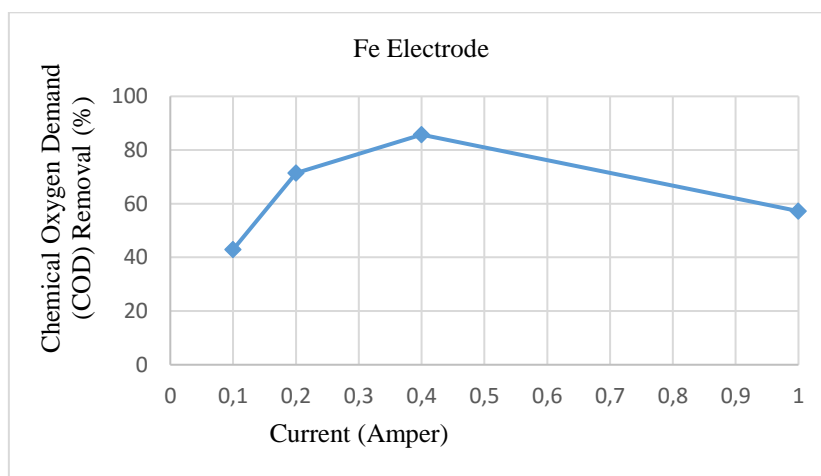
Figure 13. The Relationship Between Current Density and Chemical Oxygen Demand (COD) Removal Using Aluminum Electrodes

3.1.3. Studies on the Performance of Iron-Aluminum Electrodes in the Electrocoagulation Process

- Turbidity Removal Studies: Wastewater samples were processed at different current densities for 75 minutes, with samples taken every 15 minutes and centrifuged. Turbidity values measured with a turbid meter were recorded throughout the experimental period. The graphs of turbidity removal efficiencies versus time for experiments conducted with Iron-Aluminum electrodes at various current densities over 75 minutes are shown below (Figure 14,15,16 and 17). The turbidity removal efficiency of the experiments conducted at different currents using the Iron-Aluminum electrode was calculated to be in excess of 99,94%.
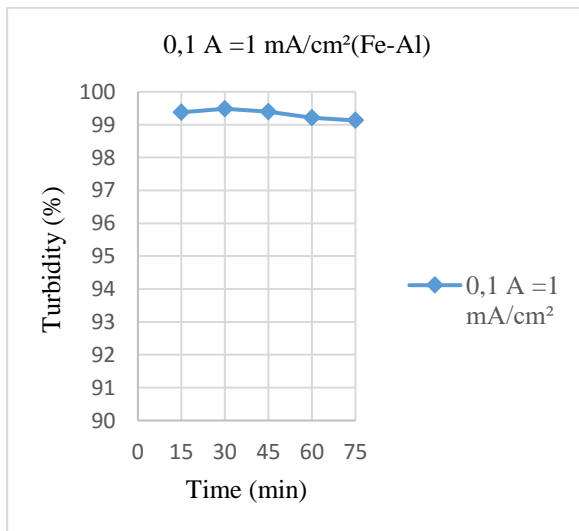
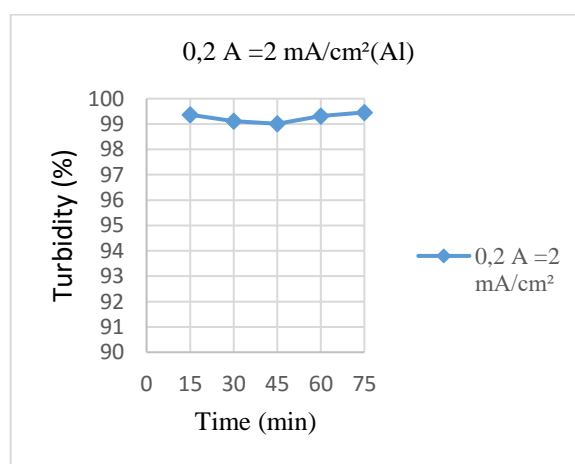**Figure 14.** Turbidity values for 0,1A
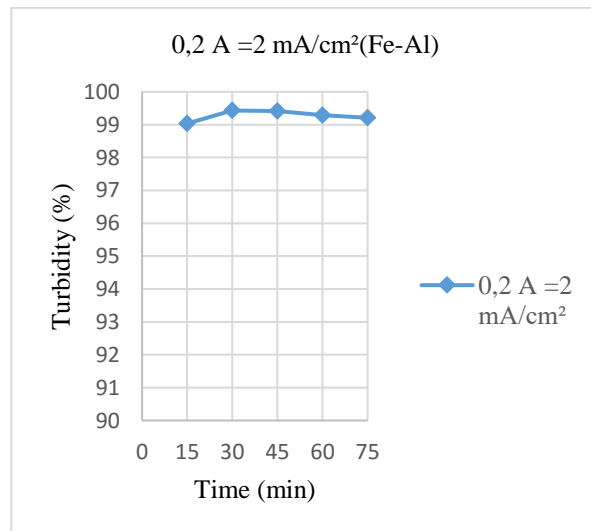
Figure 15. Turbidity values for 0,2A
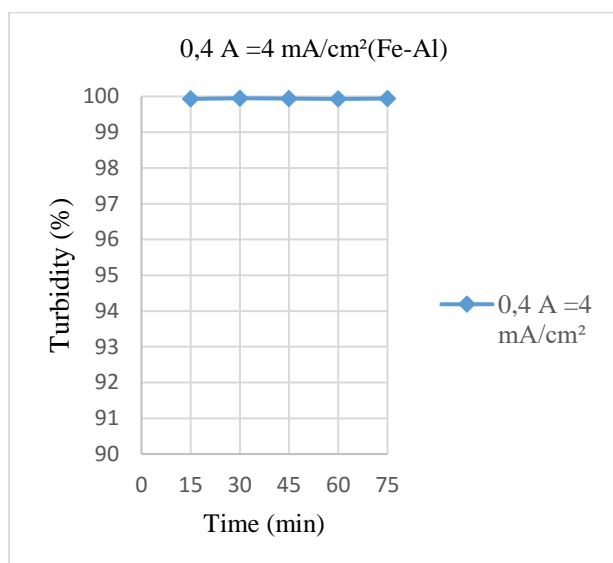
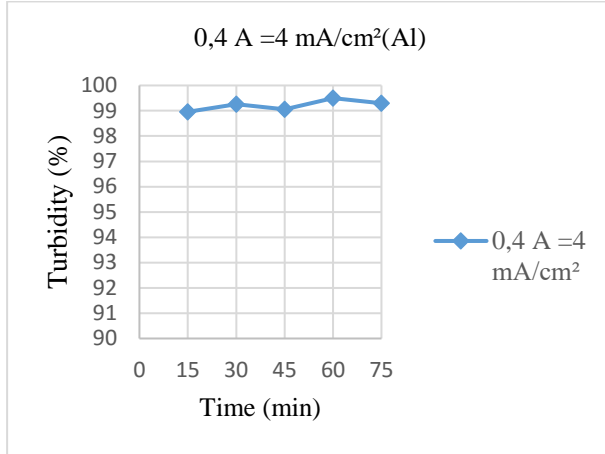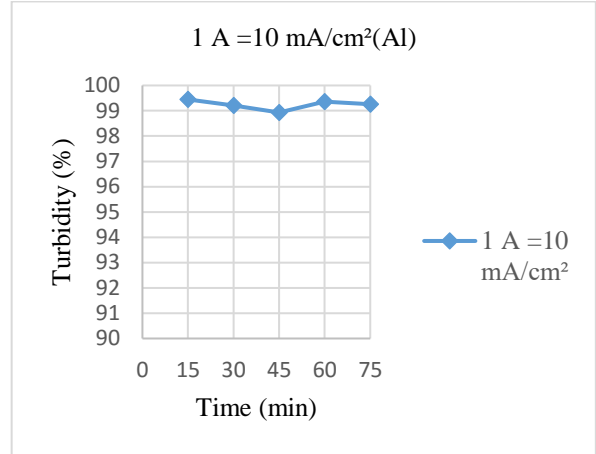**Figure 16.** Turbidity values for 0,4A   **Figure 17.** Turbidity values for 1A
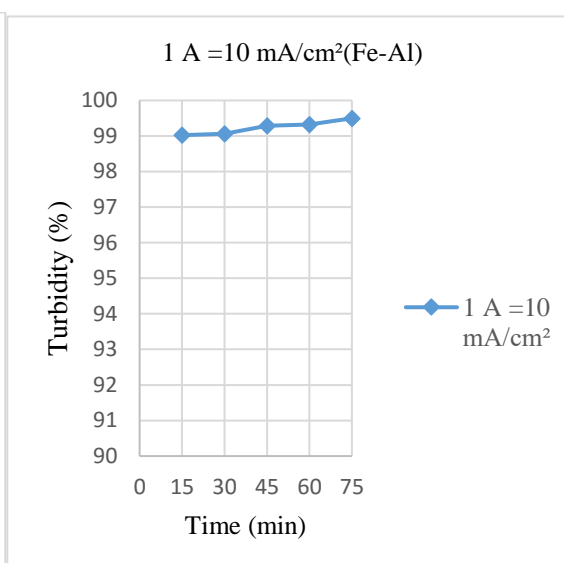
- Suspended Solids Removal Studies: The electrocoagulation process aimed at determining the performance of different electrode types in suspended solids removal was carried out over a duration of 75 minutes. The removal efficiencies achieved with the Iron-Aluminum electrode at the end of 75 minutes are as follows (Figure 18). The suspended solids removal efficiency of the experiments conducted at different currents using the Iron-Aluminum electrode was calculated to be in excess of 99%.
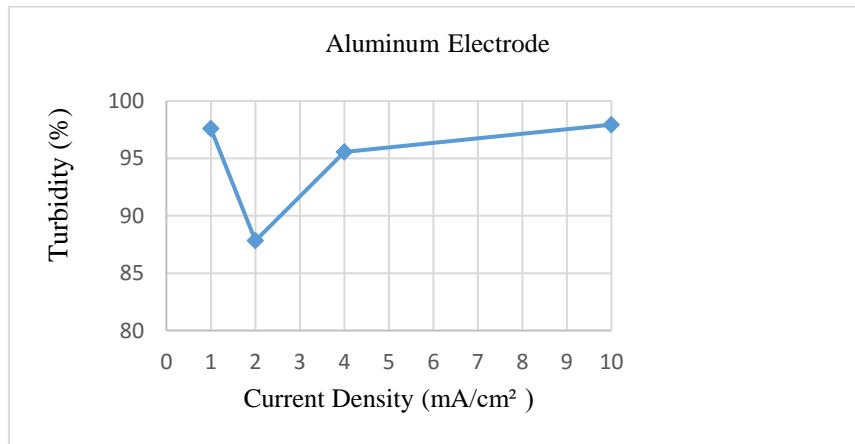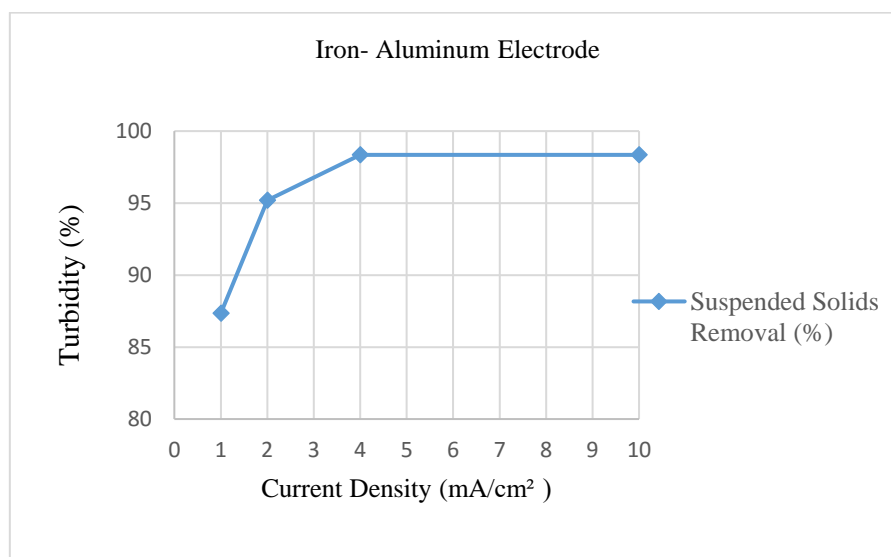

Figure 18. The Relationship Between Current Density and Suspended Solids Removal Using Iron-Aluminum Electrodes

- Chemical Oxygen Demand (COD) Removal Studies: In the electrocoagulation process conducted with ceramic industry wastewater, samples taken at the 75th minute were acidified and analyzed for Chemical Oxygen Demand (COD). The removal efficiencies achieved with the iron-aluminum electrode at the end of 75 minutes are as follows (Figure 19). The optimal COD removal was achieved at a current of 0,2-0,4 mA/cm², with a 85,7% removal efficiency.
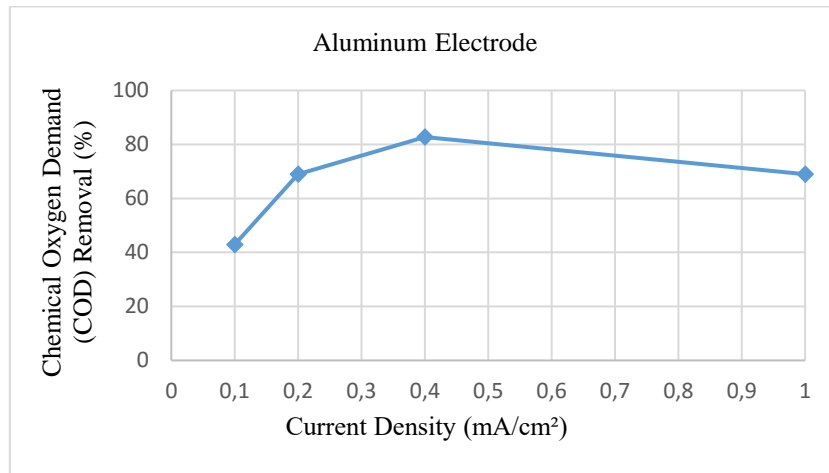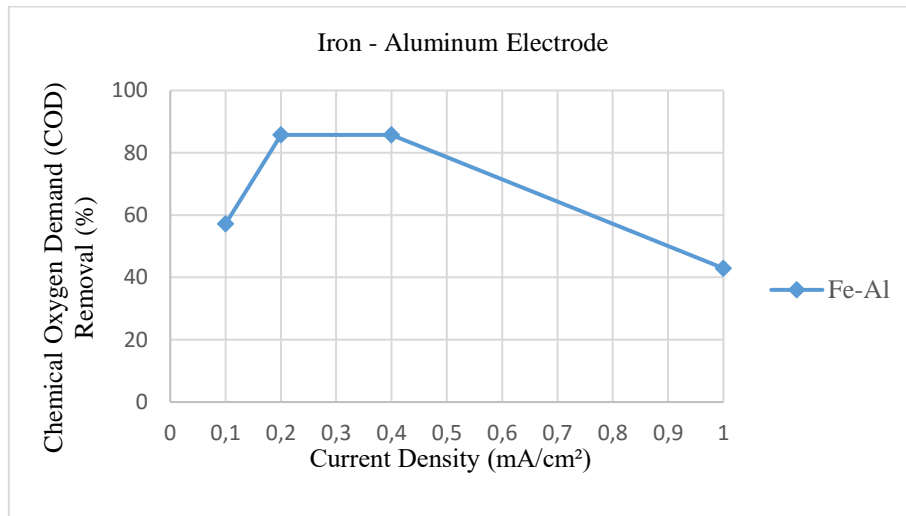
Figure 19. The Relationship Between Current Density and Chemical Oxygen Demand (COD) Removal Using Iron-Aluminum Electrodes

3.2. Effect of Electrode Type on Treatment Performance in the Electrocoagulation Process

- Turbidity Removal Studies: In the study, the effect of different electrode types on turbidity removal was investigated. The results of the experiments conducted with various electrodes are shown below (Figure 20).
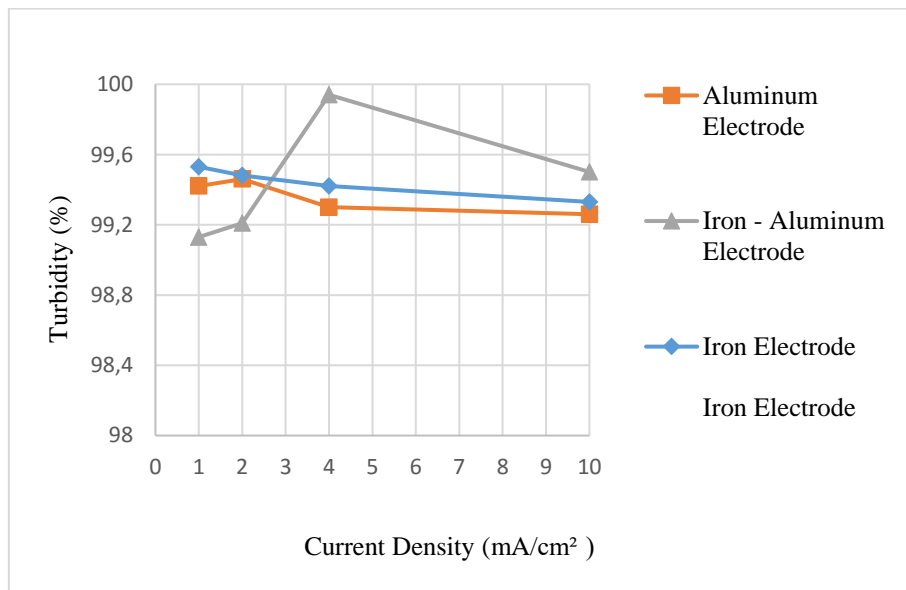
Figure 20. Relationship Between Turbidity Removal Performance and Electrode Types

- Suspended Solids Removal Studies: In the study, the effect of different electrode types on suspended solids removal was investigated. The experimental results are shown below (Figure 21).
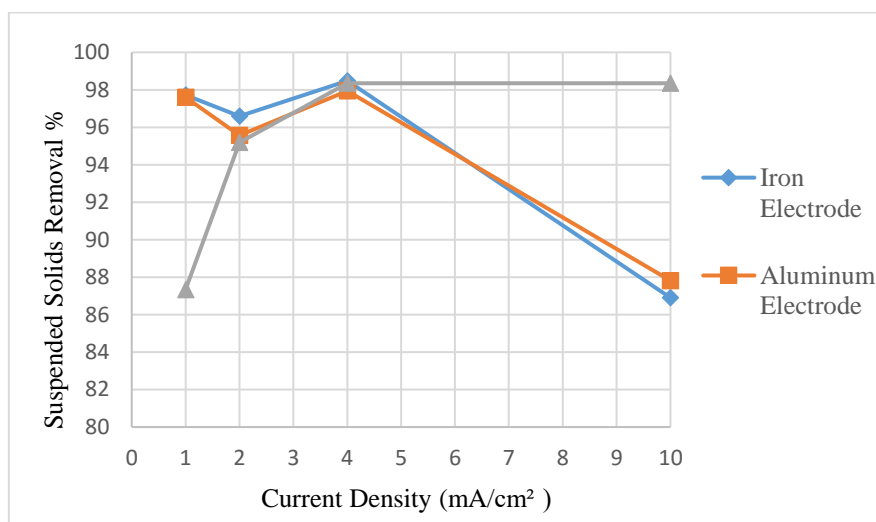
Figure 21. Relationship Between Suspended Solids Removal Performance and Electrode Types

- Chemical Oxygen Demand (COD) Removal Studies: According to the Water Pollution Control Regulation, the COD discharge limit for ceramic industry wastewater into receiving environments is 80 mg/L (Table 2). The COD concentration of the raw wastewater used in the experiments was determined to be 140.20 mg/L. In the study, wastewater samples were collected following a 75-minute treatment process at current densities of 1, 2, 4, and 10 mA/cm². The samples were acidified to below pH 2, allowed to settle, and then analyzed for COD using the supernatant. With the iron electrode, the electrocoagulation experiments resulted in a COD value reduced to 20 mg/L at a current density of 4 mA/cm², achieving a removal efficiency of 85.7%.

4. DISCUSSION AND CONCLUSION

In this study, the performance of the electrocoagulation method was evaluated using a wastewater sample from a ceramic factory in Kütahya Province. The study involved the use of different current densities (1 mA/cm², 2 mA/cm², 4 mA/cm², 10 mA/cm²), electrode types (Iron, Aluminum, Iron-Aluminum), and various treatment times (15 min, 30 min, 45 min, 60 min, 75 min) to analyze the turbidity, Suspended Solids (SS), Chemical Oxygen Demand (COD), and heavy metals in the ceramic industry wastewater. The effectiveness of the electrocoagulation method was assessed based on these parameters.

The experimental results indicate that the discharge standards set by the Water Pollution Control Regulation (WPCR) were met for all current densities. Due to the easily settleable nature of the ceramic industry wastewater, the highest turbidity removal efficiency was achieved within the early minutes of the experiment. The results of this study indicate that the optimal current density for the electrocoagulation process is 4 mA/cm².

In the pre-settled raw wastewater sample, the only parameter below the discharge limits was that of heavy metal levels. Heavy metal analyses were conducted after all electrocoagulation treatments. The electrocoagulation process achieved removal of Pb and Cd, further reducing these already below-limit heavy metals to even lower levels.

The characterisation results revealed that the concentration of suspended solids, a crucial parameter in the ceramic industry, exceeded the prescribed discharge limits. A removal efficiency of 98.5% was achieved using iron electrodes at a current density of 4 mA/cm².

Another parameter that exceed the receiving environment discharge standard in raw wastewater is COD. Experiments were conducted with iron, aluminum, and iron-aluminum electrodes at different current densities (1, 2, 4, 10 mA/cm²). Using iron electrodes, electrocoagulation experiments reduced COD to 20 mg/L at a current density of 4 mA/cm², achieving a removal efficiency of 85.7%.

The findings of the studies indicate that the electrocoagulation method could be an effective alternative to existing methods for treating ceramic industry wastewater.

The results of the experiments demonstrated that the standards set forth in the Water Pollution Control Regulation (WPCR) were met. When examining the effect of current density and electrode type on treatability, it was concluded that the best removal was achieved at 4 mA/cm² with the iron electrode. Parameters exceeding discharge limits in raw wastewater, such as Suspended Solids (SS), were removed by 98.5% at 4 mA/cm² current density in experiments using the iron electrode. Chemical Oxygen Demand (COD) was reduced by 85.7% at 4 mA/cm² current density in experiments using the iron electrode. In terms of turbidity removal 99.94% success rate was achieved using the iron-aluminum electrode at 4 mA/cm² current density.

ACKNOWLEDGEMENTS

CONFLICT OF INTEREST

The authors stated that there are no conflicts of interest regarding the publication of this article.

CRediT AUTHOR STATEMENT

Esra Fındık: Methodology, Formal analysis, Writing – Original Draft, Writing – Review & Editing. **Merve Sözder:** Resources, Writing – Original Draft, Formal analysis.

REFERENCES

[1]   Namal ÖÖ. Investigation of processes used in the treatment of textile industry wastewaters. Nevşehir J Sci Technol. 2017;6:388-396. doi:10.17100/nevbiltek.322169

[2]   Houssini NS, Essadki A, Elqars E. Removal of reactive blue and disperse red dyes from synthetic textile effluent by electrocoagulation process using Al-Al and Fe-Fe electrodes: Parametric optimization by response surface methodology. Desalination Water Treat. 2021;223:363-379. doi:10.5004/dwt.2021.27111

[3]   Sümer G. Production technology in the ceramic industry. J Min Sci Mining J. 1976;59(1):37-43. doi:10.30797/madencilik.705498

[4]   Akarsu C, Taner F, Ayol A. Treatment of leachate using the electrooxidation process. In: ISEM2014, Adıyaman; 2014.

[5]   Özyonar F, Karagözoğlu B. Treatment of textile wastewater by electrocoagulation process. Erciyes Univ J Inst Sci Technol. 2012;28(1):29-37.

[6] Emir G. Treatment of ceramic industry wastewater by electrocoagulation method. Master's thesis, Anadolu University, Turkey; 2015.

[7] Carvalho HP, Huang J, Zhao M, et al. Improvement of methylene blue removal by electrocoagulation/banana peel adsorption coupling in a batch system. Alexandria Eng J. 2015;54(3):777-786.

[8] Camcıoğlu Ş. Treatment of paper industry wastewater by electrochemical method. Doctoral dissertation, Ankara University, Turkey; 2016.

[9] Öztürk D. Treatment of marble industry wastewater by electrocoagulation method. Master's thesis, Anadolu University, Turkey; 2018.

[10] Özden M, Tekbaş M, Çalışkan Y, Bektas N. Decolourisation of disperse brown dye solution by electrocoagulation process with Al and Fe electrodes. Gazi Univ J Sci. 2019;32(1):104-114.

[11] Kasaplar M. Application of electrocoagulation process in the treatment of automotive industry wastewater. Master's thesis, Bursa Uludağ University, Turkey; 2019.

[12] Öztürk H. Removal of phenol by electrooxidation−electrocoagulation hybrid process: Reaction kinetics and determination of metabolites. Master's thesis, Kocaeli University, Institute of Science; 2019.

[13] Salah A, Bensmaili A. Decolourization of disperse blue 3 dye by electrocoagulation process using Al and Fe electrodes – Application of the artificial neural network model. Iran J Chem Chem Eng. 2022;41(4):1-11.

[14] Kurtoglu Akkaya G, Üçgül İ. Treatment of textile wastewater by electrocoagulation using direct solar energy. Black Sea J Sci. 2023;13(2):504-516. doi:10.31466/kfbd.1227078

RESEARCH ARTICLE

THE QUANTUM MECHANICAL INVESTIGATION OF THE INTERACTIONS BETWEEN H_2SO_4 AND HNO_3 MOLECULES AND WATER CLUSTERS

Fatime Mine BALCI [1], *

Süleyman Demirel Univeersity, Department of Chemistry, Faculty of Engineering and Natural Sciences, Isparta, Turkey
minebalci@sdu.edu.tr - 🆔 *0000-0002-4053-8521*

Abstract

Nitric acid and sulfuric acid can form various hydrogen bonds with each other, creating stable species with water molecules. Additionally, these acid molecules are also significant from an atmospheric perspective and play an important role in atmospheric chemistry. This theoretical study focuses on the analysis of intermolecular interactions in structures obtained by scanning the potential energy surface of clusters formed by nitric acid and sulfuric acid with two and three water molecules. In the structures obtained with three water molecules, the ionic forms of these acid molecules were observed. The most stable structures energetically are those where nitric acid acts as a proton donor to sulfuric acid. The results of all the structures obtained were analyzed structurally, energetically, and spectroscopically.

1. INTRODUCTION

Sulfuric acid, nitric acid, and water are substances abundantly found in nature and play an active role in many heterogeneous reactions, particularly those occurring in the atmosphere. Most of these reactions are associated with phenomena that affect human life, such as acid rain and the depletion of the ozone layer in the stratosphere. Specifically, it is known that many heterogeneous reactions responsible for the depletion of the ozone layer occur in Polar Stratospheric Clouds (PSC) located in the upper layers of the stratosphere [1-5]. It has been suggested that the majority of these clouds consist of supercooled ternary solutions (STS) formed by H_2SO_4, HNO_3, and H_2O molecules, with a smaller portion composed of nitric acid trihydrates (NAT) and ice particles. Furthermore, sulfuric acid is considered an important compound involved in the early stages of cloud formation in the atmosphere [6] and central to new particle formation at atmospheric concentrations [7], with interactions with water, ammonia, and other species being considered as the initiation of this formation [8-10]. It is known that H_2SO_4/H_2O binary aerosols play a role in the formation of $H_2SO_4/HNO_3/H_2O$ (STS) particles, which constitute a large portion of PSCs. Numerous experimental studies on $H_2SO_4/HNO_3/H_2O$ (STS) particles exist in the literature [3,11-13], but their composition and formation mechanisms are still not fully understood [5].

With the discovery of polar stratospheric clouds, interest has increased in molecules important for the atmosphere, particularly strong acid molecules (such as HNO_3, H_2SO_4, and HCl). There are numerous experimental and theoretical studies in the literature on nitric acid and its hydrates [14-19]. Additionally,

---

most of the heterogeneous reactions leading to the depletion of the ozone layer are catalyzed on ice surfaces. Ice surfaces contain active sites for the interactions of strong adsorbates, which are the cause of many chemical phenomena. The ability of strong acid molecules to form strong hydrogen bonds enhances the importance of intermolecular interactions in studies focused on these molecules. Specifically, the solvation and ionization of strong acid adsorbates on ice surfaces or within water molecules are among the topics actively researched in the scientific community [20-23]. Moreover, understanding how the interactions of multiple strong acids (H_2SO_4 and HNO_3) change on ice surfaces or water molecules is considered an important area of study. However, before analyzing large (bulk) systems, it is always advantageous to study smaller clusters. Therefore, this study provides a detailed analysis of the interactions of H_2SO_4 and HNO_3 molecules on clusters containing multiple water molecules.

There are studies in the literature on the binary systems of HNO_3/H_2O, H_2SO_4/H_2O, and H_2SO_4/HNO_3. Particularly, many studies have been conducted on the complexes formed by HNO_3 and H_2SO_4 molecules with water, which are important in atmospheric chemistry. These studies have been performed using experimental and quantum mechanical methods [17, 24-30]. It has been found that the stable $HNO_3 \cdots H_2O$ dimer has a cyclic structure, and the strong hydrogen bond is proposed to form between the acidic hydrogen of nitric acid and the oxygen of water. The interaction energy for this dimer structure has been calculated to be approximately between -7 and -10 kcal/mol in studies performed at different levels and with different basis sets [30].

Unlike HNO_3, H_2SO_4 has two protons. Potential energy surface scans for the H_2SO_4 monomer structure have shown that the trans conformation of sulfuric acid is more energetically stable than the cis conformation [31]. The interactions between sulfuric acid and water molecules have also been examined. In the sulfuric acid monohydrate structure, the strong hydrogen bond forms between the oxygen of water and the hydrogen of sulfuric acid. The structure in which the trans conformation of H_2SO_4 interacts with water has been found to be the most stable structure in the literature [32-38]. There are two studies on the $H_2SO_4 \cdots HNO_3$ dimer [38, 39]. In the most stable structure, both nitric acid and sulfuric acid act as proton donors to each other.

There are few studies in the literature regarding the interactions of H_2SO_4 and HNO_3 with water molecules. Theoretical studies have examined $H_2SO_4/HNO_3/H_2O$ ternary clusters and explored the stability of these complex structures formed through hydrogen bonds [40-42]. However, there is no existing study on the interactions of H_2SO_4 and HNO_3 with clusters containing multiple water molecules. Therefore, this study analyzes the intermolecular interactions of H_2SO_4 and HNO_3 molecules on clusters containing two and three water molecules.

2. MATERIALS AND METHODS

In this study, the Gaussian 09 software package was used for electronic calculations [43]. The selection of the structural parameters for the H_2SO_4, HNO_3, and H_2O monomer molecules was made by comparing them with available experimental gas-phase values in the literature. Since ab initio calculations are entirely based on static computations, the results obtained are considered as gas-phase values. The Density Functional Theory (DFT) method was employed in the calculations, with the M062X functional, which is known for its reliable description of non-covalent interactions. Additionally, the aug-cc-pvdz basis set, which provides good results for hydrogen-bonded systems, was used [44].

Table 1 presents the calculated bond lengths and bond angles for the H_2SO_4, HNO_3, and H_2O monomer molecules, along with their corresponding experimental values.

Table 1. Structural parameters H_2SO_4, HNO_3, and H_2O molecules. Bond lengths (r) are given in Å, and bond angles (a) are given in degrees.

Structural parameters	M062X/aug-cc-pvdz	Experimental *
H_2SO_4 (trans)		
r(O-H)	0.97	0.97
r(HO-S)	1.62	1.57
r(S-O)	1.45	1.42
a(H-O-S)	107.6	108.5
a(OH-S-O)	108.3	108.6
a(O-S-O)	124.8	123.3
a(OH-S-OH)	101.5	101.3
HNO_3		
r(O-H)	0.97	0.96
r(N-O)	1.37	1.41
r(N-O4)	1.20	1.21
r(N-O5)	1.19	1.20
H_2O		
r(O-H)	0.96	0.96
a(H-O-H)	105	105

* **references [31, 45-46].**

In this study, the potential energy surfaces of $H_2SO_4 \cdots HNO_3 \cdots (H_2O)_n$ (n=2,3) clusters were investigated using the ABCluster code [47,48]. The ABCluster global search method was applied in conjunction with the Gaussian 09 program. Fifty structural optimizations were performed at the B3LYP/6-31++g(d) level. At this stage, several minimum energy points were obtained, and among these, distinct and energetically more stable structures were selected. The chosen structures were further optimized at the M062X/aug-cc-pvdz level, and frequency calculations were performed to determine whether they represented true minima on the potential energy surface. The "tight convergence" criterion was employed in the optimization steps. As a result of the calculations, the binding energies and zero-point energies (ZPE) of these clusters were determined based on their configurations. The binding energies of the clusters were calculated by subtracting the energies of the monomers from the energy of the complex.

2.1. Description of Clusters

The systems studied are named as NSnW-m, where N, S, and W represent nitric acid (HNO_3), sulfuric acid (H_2SO_4), and water (H_2O) molecules, respectively. The n indicates the number of water molecules in the cluster, and m is an index representing the different structures of a specific NSnW cluster based on their energy ranking. For example; NS2W-4 refers to the fourth structure of the system containing one nitric acid molecule, one sulfuric acid molecule, and two water molecules ($H_2SO_4 \cdots HNO_3 \cdots H_2O)_2$) in order of energy stability.

3. RESULTS AND DISCUSSION

3.1. Results for NS2W Clusters

As a result of the potential energy surface scan, 22 minimum structures were identified for the NS2W clusters, as shown in Figure 1. The binding energies of these structures, calculated at the M062X/aug-cc-pvdz level and binding energies with zero-point energy correction (ΔZPEC) are listed in Table 2. The binding energies of the 22 structures range from -34.63 kcal/mol to -20.15 kcal/mol.

None of the structures exhibit ionic forms of nitric acid or sulfuric acid. The NS2W-1 structure was found to be the most energetically stable. In this configuration, nitric acid acts as a proton donor to sulfuric acid, while sulfuric acid serves as a proton donor to the water molecule. Water molecules

interact with each other as well as with the other acid molecules. Each molecule functions both as a proton donor and a proton acceptor.

In the NS2W-2 structure, a similar molecular interaction was observed, but the orientation of hydrogen atoms not involved in bond formation was different. The energy difference between this structure and NS2W-1 is only 0.05 kcal/mol. The structural difference between these two configurations arises from the water molecule containing the O5 atom in the NS2W-2 structure. While this water molecule accepts a proton, it simultaneously acts as a proton donor both to another water molecule and to one of the oxygen atoms of nitric acid. In the N2W-1 structure, both water molecules accept and donate a proton. This situation makes the structure more stable due to the cooperative effect in hydrogen-bonded systems. A similar situation has been observed in other studies in the literature [30,40]. In the structures NS2W-5, NS2W-8, NS2W-9, NS2W-10, NS2W-15, NS2W-16, and NS2W-17, where nitric acid acts as a proton donor to sulfuric acid, a similar effect was not observed, resulting in these structures being obtained as energetically less stable. For instance, in NS2W-8, water molecules do not interact with each other.

Apart from NS2W-22, where nitric acid does not act as a proton donor to the water molecule, all other structures show that nitric acid donates a proton to the water molecule. NS2W-22 is the least stable structure with a binding energy of -20.15 kcal/mol, as the hydrogen atoms of nitric acid do not interact with other molecules. In the NS2W-3 and NS2W-4 structures, each molecule forms a cyclic structure by both donating and accepting a proton, with binding energies calculated as -33.93 kcal/mol and -33.81 kcal/mol, respectively. In these two minimum structures, water molecules do not interact with each other.

Structures where sulfuric acid acts as a proton donor to nitric acid, such as NS2W-10, NS2W-11, NS2W-12, NS2W-13, NS2W-14, and NS2W-20, are found to be less stable. Except for NS2W-10, in these structures, nitric acid donates a proton to the water molecule. In NS2W-10, sulfuric acid acts as a proton acceptor from nitric acid, making this structure less stable compared to NS2W-1 or NS2W-2, as nitric acid does not interact with water molecules in this case.

The results of the NS2W structures can be compared with those of the $H_2SO_4 \cdots HNO_3 \cdots H_2O$ clusters found in the literature [40]. It has been observed that the most energetically stable structures obtained in this study are similar to the results reported for ternary systems. The cyclic structure, where sulfuric acid acts as a proton donor to water and nitric acid acts as a proton donor to sulfuric acid, has been identified as the most energetically stable configuration for ternary systems. At the same time, structures in which nitric acid does not engage in any interaction were found to be energetically less stable. Unlike ternary systems, in this study, due to the larger number of water molecules, nitric acid and sulfuric acid do not interact with each other in structures like NS2W-3 and NS2W-4. However, since both acid molecules act as proton donors to water molecules and form a cyclic arrangement, these structures are energetically stable. There is an energy difference of approximately 0.07 to 0.08 kcal/mol between the NS2W-1 structure and the NS2W-3 and NS2W-4 structures, respectively.
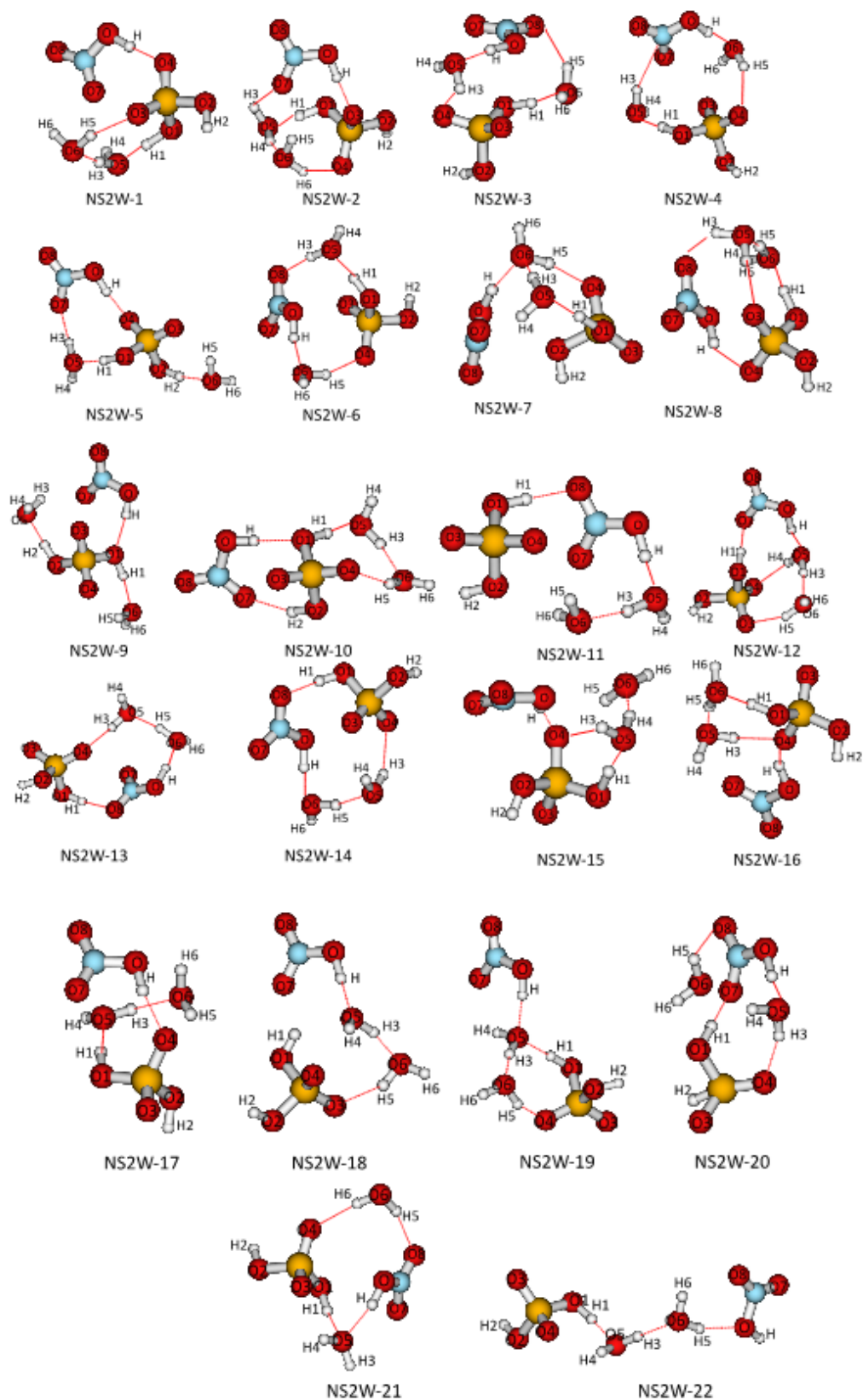
Figure 1. Optimized NS2W Clusters at the M062X/aug-cc-pvdz level.

Table 2. Binding energies ($E_{binding}$) of NS2W clusters calculated at the M062X/aug-cc-pvdz level and ΔZPEC corrected binding energies ($E_{binding+\Delta ZPEC}$). Values are given in kcal/mol.

NS2W clusters	$E_{binding}$	$E_{binding+\Delta ZPEC}$
NS2S-1	-40.22	-34.63
NS2S-2	-39.58	-34.58
NS2S-3	-39.14	-33.93
NS2S-4	-39.06	-33.81
NS2S-5	-38.99	-33.76
NS2S-6	-38.79	-33.76
NS2S-7	-38.78	-33.14
NS2S-8	-37.81	-32.88
NS2S-9	-38.07	-32.53
NS2S-10	-37.36	-32.11
NS2S-11	-37.28	-31.88
NS2S-12	-36.85	-31.78
NS2S-13	-36.80	-31.59
NS2S-14	-36.36	-31.34
NS2S-15	-35.55	-30.56
NS2S-16	-35.46	-30.19
NS2S-17	-35.35	-30.18
NS2S-18	-35.28	-29.65
NS2S-19	-35.00	-29.05
NS2S-20	-33.68	-28.64
NS2S-21	-25.51	-20.38
NS2S-22	-25.28	-20.15

When examining the structural parameters of the NS2W clusters, it is observed that hydrogen bonds play a crucial role in the stability of the structures. Important structural parameters for the NS2W clusters are detailed in Supplementary Materials, and a summary is given in Figure 2.

In the NS2W-1 structure, the strongest hydrogen bond is between sulfuric acid and water, with a bond length of 1.33 Å. This $H_2SO_4\cdots H_2O$ interaction is the strongest interaction observed among all structures. Literature also indicates that the $H_2SO_4\cdots H_2O$ dimer interaction is stronger than the $HNO_3\cdots H_2O$ interaction [40]. In the NS2W-1 structure, nitric acid acts as a proton donor to sulfuric acid, with a hydrogen bond length of 1.62 Å.

In structures such as NS2W-2, NS2W-5, NS2W-9, NS2W-10, NS2W-13, NS2W-14, NS2W-15, NS2W-16, and NS2W-17, nitric acid acts as a proton donor to one of the oxygen atoms of sulfuric acid. However, the strength of these bonds is weaker compared to the NS2W-1 structure. The literature also notes that dimer structures of $H_2SO_4\cdots HNO_3$, where both acids act as proton donors to each other, are observed to be the most stable [38,39].

In the NS2W-1 structure, the hydrogen bond between water molecules is calculated to be 1.65 Å. Within this structure, one of the water molecules acts as a proton donor to nitric acid, with this weak hydrogen bond (H4···O7) having a length of 2.41 Å.

Similarly, in NS2W-3 and NS2W-4 structures, both nitric acid and sulfuric acid donate protons to water molecules and also receive protons from them. The hydrogen bonds formed between acid molecules and water molecules are stronger, as detailed in Supplementary Materials (e.g., H···O5, H1···O6, H···O6, and H1···O5 bonds), compared to those formed between water molecules and acid molecules, which are weaker. For example, in the NS2W-3 structure, the hydrogen bond length between H3 and O3 is 2.27 Å, while in the NS2W-4 structure, the distance between H5 and O4 is 1.89 Å.

The O-H bond lengths of acid molecules have varied from their monomer values. As shown in Table 1, the O-H bond lengths for monomeric HNO_3 and H_2SO_4 are provided. In the NS2W clusters, the O-H bond length of nitric acid ranges from 0.97 Å to 1.05 Å. It has been observed that the O-H bond length is longer in structures where nitric acid donates protons to water or sulfuric acid. Specifically, in cyclic structures where each molecule donates and receives a proton (e.g., NS2W-3, NS2W-4, NS2W-13 as shown in Figure 1), the O-H bond length is notably elongated.

In the NS2W-22 structure, since the O-H bond does not participate in any interactions, the O-H bond length remains the same as in monomeric HNO_3 (0.97 Å). A similar situation is observed for the O-H bonds in sulfuric acid. The O-H bond lengths involved in interactions with values ranging from 0.99 Å to 1.10 Å. The greatest elongation is observed in the NS2W-1 (O1-H1) and NS2W-2 (O1-H1) structures, where the non-interacting O-H bond length remains the same as the monomeric value (e.g., O2-H2 bond in NS2W-1).

For water molecules, the O-H bond lengths involved in interactions range from 0.97 Å to 0.99 Å. Non-interacting O-H bonds in water molecules have a length of 0.96 Å.
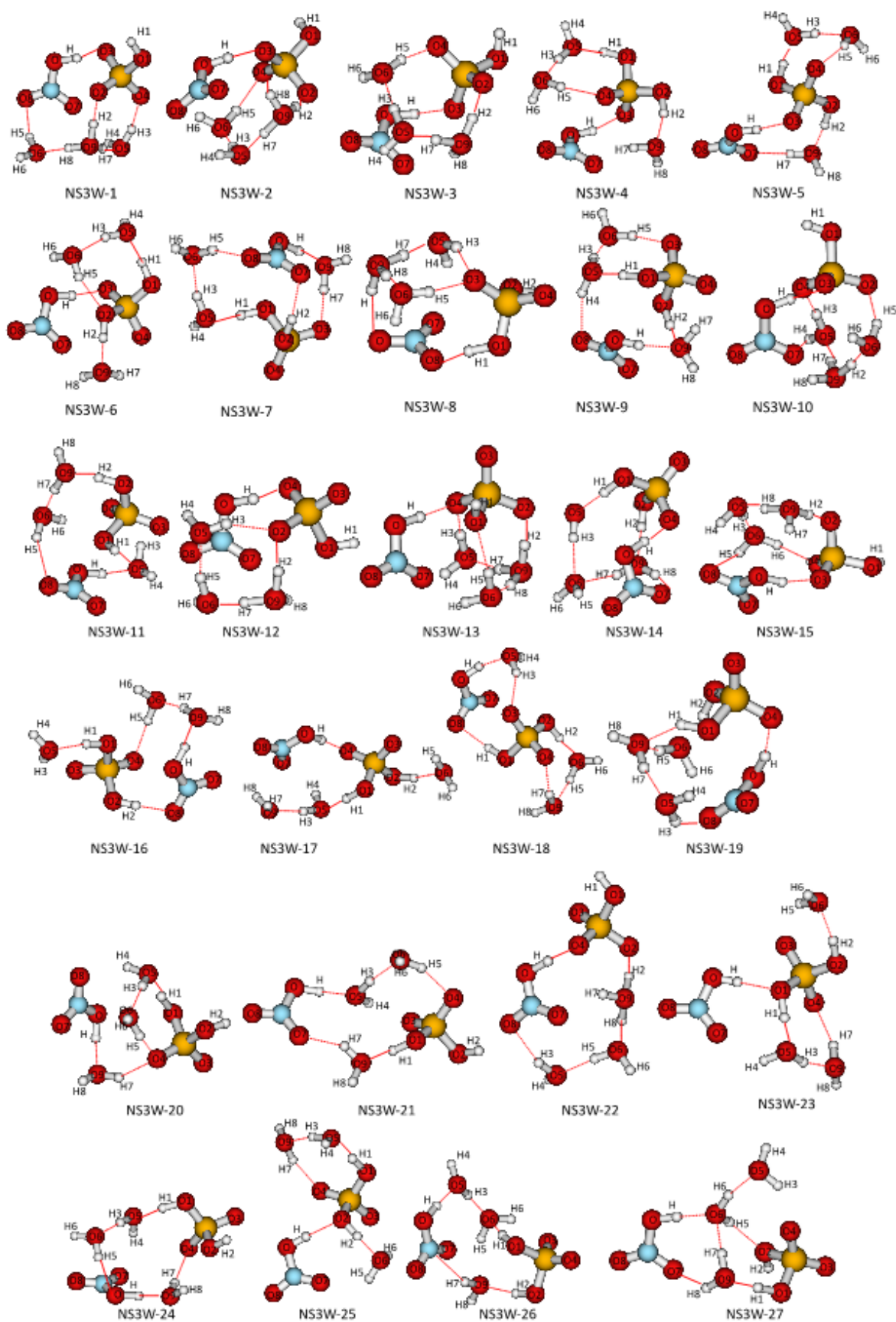
3.2. Results for NS3W Clusters

In the potential energy surface scan for the NS3W clusters, 38 minimum structures were identified, as shown in Figure 2. The binding energies calculated at the M062X/aug-cc-pvdz level and binding energies with zero-point energy correction (ΔZPEC) for these structures are presented in Table 3.

Unlike the NS2W clusters, among the 38 NS3W clusters obtained after optimization, 10 structures feature either sulfuric acid or nitric acid in an ionic state. The binding energies for these structures range from -48.14 kcal/mol to -36.14 kcal/mol. The most stable structure, according to the energy ranking, is NS3W-1, which resembles the arrangement of molecules in NS2W-1. In this structure, nitric acid acts as a proton donor to sulfuric acid, sulfuric acid donates protons to water, and the water molecules act as proton donors both to each other and to the acid molecules. The binding energy is calculated to be -48.14 kcal/mol, and sulfuric acid is found to be ionic in this minimum structure.

Sulfuric acid is also observed to be ionic in NS3W-2, NS3W-3, NS3W-10, NS3W-12, NS3W-13, NS3W-15, and NS3W-22 structures. In general, sulfuric acid in these structures is observed to be three-coordinated. The binding energies for these structures are -46.29 kcal/mol, -46.13 kcal/mol, -43.98 kcal/mol, -43.27 kcal/mol, -43.26 kcal/mol, -42.90 kcal/mol, and -41.11 kcal/mol, respectively.

Nitric acid is found to be ionic only in NS3W-8 and NS3W-32, where it is observed to be three-coordinated. The literature contains various studies on the ionization of acid molecules [17, 29, 49-51]. For instance, it has been noted that at least four water molecules are needed for the ionization of HCl [49]. Additionally, the interaction of nitric acid with HCl in water clusters has been studied, and structures where nitric acid is three-coordinated were also found to be ionic [52]. For ionization to occur, the water molecule accepting the proton must also be three-coordinated. For example, in the NS3W-4 structure, even though sulfuric acid is three-coordinated, one of the hydrogen atoms of the water molecule that donates a proton is free (H4 atom).

Among the NS3W clusters, the top three energy-stable structures are in an ionic state (NS3W-1, NS3W-2, NS3W-3). The subsequent NS3W-4 structure does not feature ionic acid molecules and has a binding energy of -45.37 kcal/mol. In this structure, nitric acid acts as a proton donor to sulfuric acid, and sulfuric acid acts as a proton donor to a water molecule, resulting in a cyclic structure. This arrangement is identical to both the most energetically stable NS2W-1 structure and the most stable configuration found for ternary systems [40].

NS3W-1 NS3W-2 NS3W-3 NS3W-4 NS3W-5

NS3W-6 NS3W-7 NS3W-8 NS3W-9 NS3W-10

NS3W-11 NS3W-12 NS3W-13 NS3W-14 NS3W-15

NS3W-16 NS3W-17 NS3W-18 NS3W-19

NS3W-20 NS3W-21 NS3W-22 NS3W-23

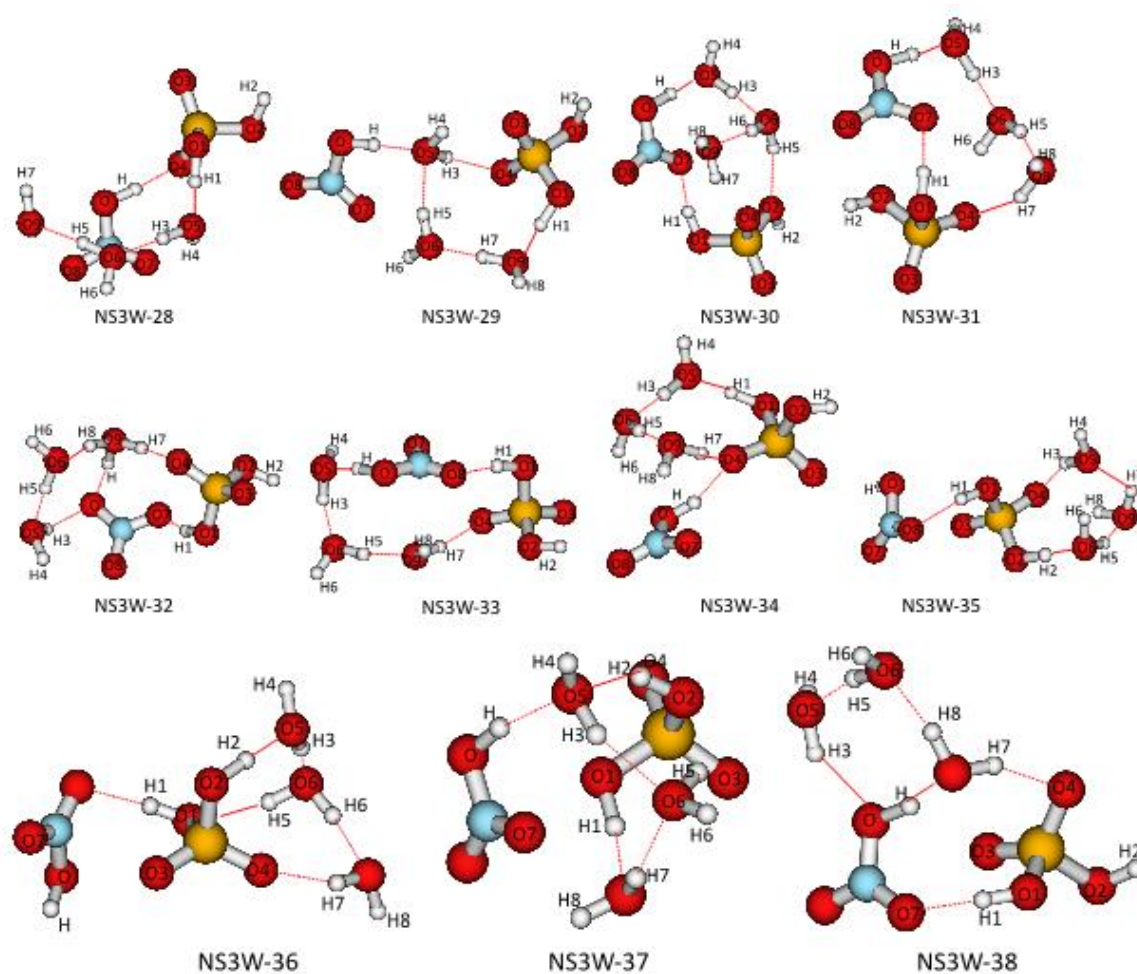NS3W-24 NS3W-25 NS3W-26 NS3W-27

Figure 2. Optimized NS3W Clusters at the M062X/aug-cc-pvdz level.

Table 3. Binding energies ($E_{binding}$) of NS3W clusters calculated at the M062X/aug-cc-pvdz level and ΔZPEC corrected binding energies ($E_{binding+\Delta ZPEC}$). Values are given in kcal/mol.

NS3W Clusters	$E_{binding}$	$E_{binding+\Delta ZPEC}$
NS3S-1	-55.50	-48.14
NS3S-2	-53.23	-46.29
NS3S-3	-53.16	-46.13
NS3S-4	-53.03	-45.37
NS3S-5	-52.58	-45.28
NS3S-6	-53.40	-46.11
NS3S-7	-52.01	-44.16
NS3S-8	-51.58	-44.29
NS3S-9	-51.49	-43.88
NS3S-10	-51.42	-43.98
NS3S-11	-51.16	-43.27
NS3S-12	-51.09	-44.19
NS3S-13	-50.98	-43.26
NS3S-14	-50.89	-43.30
NS3S-15	-50.76	-42.90
NS3S-16	-50.68	-42.74
NS3S-17	-50.51	-42.99
NS3S-18	-50.31	-42.97
NS3S-19	-50.09	-43.12
NS3S-20	-50.03	-42.65
NS3S-21	-49.37	-42.05
NS3S-22	-48.79	-41.11
NS3S-23	-48.75	-41.39
NS3S-24	-48.72	-41.42
NS3S-25	-48.67	-41.92
NS3S-26	-48.66	-40.30
NS3S-27	-48.64	-41.51
NS3S-28	-48.35	-41.09
NS3S-29	-48.15	-40.57
NS3S-30	-47.79	-40.33
NS3S-31	-46.93	-39.34
NS3S-32	-46.79	-39.55
NS3S-33	-46.71	-39.57
NS3S-34	-46.39	-39.43
NS3S-35	-45.45	-37.72
NS3S-36	-44.62	-36.21
NS3S-37	-44.09	-36.33
NS3S-38	-43.23	-36.14

In the NS3W clusters, key structural parameters are provided in Supplementary Materials. The most stable structure, NS3W-1, features nitric acid donating a proton to sulfuric acid. This structure resembles the most stable NS2W-1 structure, but sulfuric acid is in an ionic state here. The strongest hydrogen bond in NS3W-1 is between nitric acid and sulfuric acid, with an O3···H bond length of 1.42 Å. Each hydrogen atom of the H_3O^+ ion interacts with oxygen atoms from two water molecules and one oxygen atom from sulfuric acid. The hydrogen bonds made by the H_3O^+ ion are calculated as follows: O2···H2: 1.50 Å, O6···H8: 1.58 Å, O5···H7: 1.48 Å. Water molecules in this structure also donate protons to the acid molecules, but these interactions are weaker compared to the other hydrogen bonds, with bond lengths of: O4···H3: 1.78 Å, O8···H5: 1.89 Å.

In addition to NS3W-1, sulfuric acid is also found in an ionic state in NS3W-2, NS3W-3, NS3W-10, NS3W-12, NS3W-13, NS3W-15, and NS3W-22. In these structures, the three-coordination state of the H_3O^+ ion is less stable. For instance, in NS3W-2, the hydrogen bonds involving the H_3O^+ ion with the molecules are: O2···H2: 1.46 Å, O5···H7: 1.37 Å, O7···H8: 2.08 Å. The O7···H8 interaction is

notably weaker. Similar observations are made in other structures where sulfuric acid is ionic. In NS3W-8 and NS3W-32, nitric acid is ionic. In NS3W-8, the hydrogen bonds between the H_3O^+ ion and water molecules are: O6···H8: 1.47 Å, O5···H7: 1.43 Å. The interaction with the nitrate ion (O···H hydrogen bond) is 1.84 Å. The strongest hydrogen bond is observed as O8···H1 at 1.34 Å. In NS3W-32, the hydrogen bonds made by the H_3O^+ ion are: O6···H8: 1.43 Å, O···H: 1.56 Å, O4···H7: 1.65 Å. In this structure, the nitrate ion is three-coordinated, but unlike NS3W-8, one of the oxygen atoms of the nitrate ion (O atom) is two-coordinated. In NS3W-8, all the oxygen atoms of the nitrate ion are single-coordinated.

In NS3W structures where the acid molecules are molecularly obtained, nitric acid either donates a proton to sulfuric acid or to water. In the more stable structures, nitric acid donates a proton to sulfuric acid such as in NS3W-4 and NS3W-5. However, only in NS3W-35 and NS3W-36, the hydrogen of nitric acid does not participate in any interactions. Generally, the hydrogen atom of nitric acid interacts with one of the non-proton-containing oxygen atoms of sulfuric acid. Only in NS3W-23 and NS3W-25 does the hydrogen atom of nitric acid donate a proton to one of the proton-containing oxygen atoms of sulfuric acid, which is weaker compared to interactions where nitric acid donates a proton to non-proton-containing oxygen atoms of sulfuric acid. For NS3W-23, the O1···H bond is 1.75 Å, and for NS3W-25, the O2···H bond is 1.78 Å.

In the NS3W clusters, the O-H bond lengths of nitric acid involved in interactions range from 0.98 Å to 1.09 Å. The maximum extension is observed in NS3W-31, a structure where each molecule forms a chain-like configuration by donating and accepting a proton, similar to the structure described for NS2W-13. As the number of water molecules increases, a further extension of the O-H bond lengths is observed.

A similar trend is noted for the O-H bonds of sulfuric acid and water molecules, where the bond lengths also increase with more water molecules in the system.

3.3. Vibrational Frequencies

Harmonic frequency analyses for the NS2W and NS3W clusters were performed at the M062X/aug-cc-pvdz level. Figure 3 shows the IR spectra of five structures with different configurations selected from these clusters (NS2W-1, NS2W-3, NS3W-9, NS3W-1, and NS3W-8); the IR spectra of all other structures are presented in Supplementary Materials. In the NS2W-1 structure, nitric acid acts as a proton donor to sulfuric acid, while in the NS2W-3 and NS3W-9 structures, nitric acid is the proton donor to water. In the NS3W-1 structure, sulfuric acid is in an ionic form, whereas in the NS3W-8 structure, nitric acid is in an ionic form.
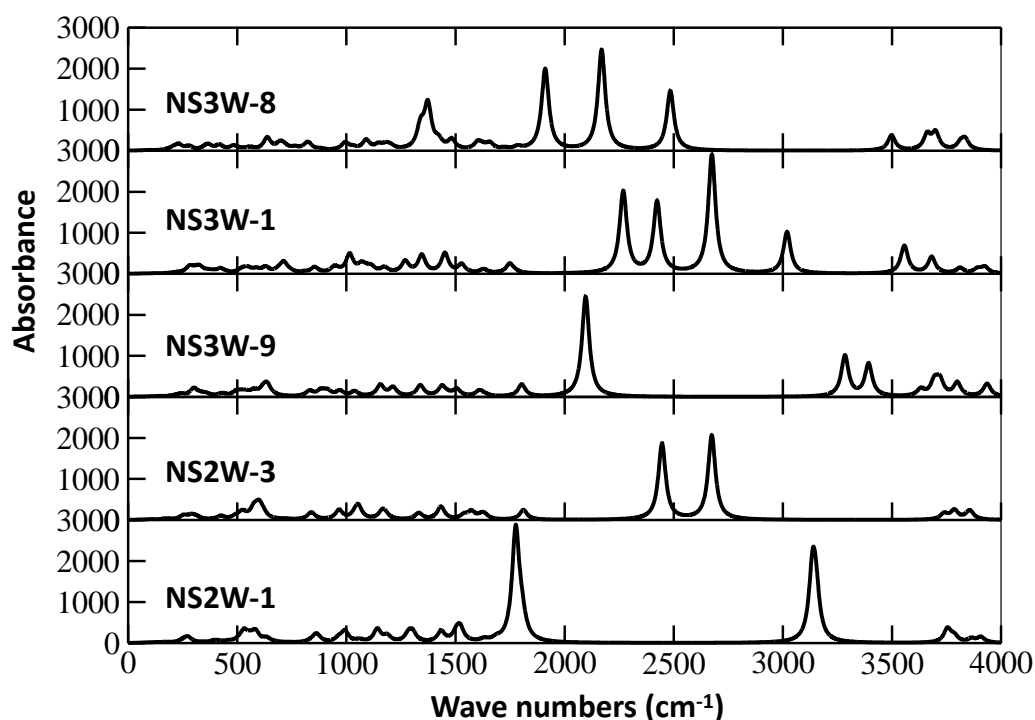
Figure 3. IR spectra of NS2W-1, NS2W-3, NS3W-9, NS3W-1 and NS3W-8.

Looking at the spectra of NS2W-1 and NS2W-3 structures, the vibration frequencies of the O-H bond in HNO_3 peak at 3136 cm^{-1} and 2674 cm^{-1}, respectively. For the monomer HNO_3, the O-H bond vibration frequency is calculated to be 3769 cm^{-1} at the M062X/aug-cc-pvdz level. In this case, the O-H bond is more stretched when HNO_3 acts as a proton donor to water. A similar situation has also been observed in ternary systems [40]. In the NS3W-9 structure, although HNO_3 is also a proton donor to water, the O-H bond peaks at 3284 cm^{-1} in the spectrum. This structure causes less stretching of the O-H bond compared to others due to the involvement of both protons of sulfuric acid in the interaction. In the NS3W-1 structure, sulfuric acid is in an ionic state, and the O-H bond of HNO_3 shows the largest stretching in this structure, peaking at 2268 cm^{-1} in the IR spectrum.

Looking at the O-H bonds of sulfuric acid; in the NS2W-1 and NS2W-3 structures, the interacting O-H bonds peak at 1775 cm^{-1} and 2446 cm^{-1}, respectively. The vibration frequencies of the O-H bonds for the monomer H_2SO_4 are calculated to be 3783 cm^{-1} and 3788 cm^{-1}. Accordingly, the largest shift in the spectrum is observed in the NS2W-1 structure. In this structure, sulfuric acid acts as a proton acceptor from nitric acid and also shows three-coordinations of sulfuric acid.

In the NS3W-9 structure, both O-H bonds of sulfuric acid are involved in interactions. The interacting O-H bonds peak at 2096 cm^{-1} (O1-H1) and 3632 cm^{-1} (O2-H2). In the NS3W-1 structure, sulfuric acid donates one proton to water to form an H_3O^+ ion, while the other O-H bond does not participate in any interaction. The vibration frequency of this O-H bond is 3812 cm^{-1}. In the NS3W-8 structure, the O-H bond of sulfuric acid interacting with the nitrate ion peaks at 1911 cm^{-1}, while the free O-H bond peaks at 3814 cm^{-1}. In both NS3W-1 and NS3W-8 structures, the peaks associated with the H_3O^+ ion appear in the spectrum approximately between 2100 cm^{-1} and 2600 cm^{-1}.

When examining the O-H bonds of water molecules, it has been observed that the interacting O-H bonds show larger shifts in the spectrum compared to their monomer values (3867 cm^{-1} and 3976 cm^{-1}). Additionally, it has been noted that the interaction of O-H bonds with acids or water alters the stretching of these bonds. When water molecules interact with each other, their O-H bonds peak in the region of 3000 cm^{-1} to 3400 cm^{-1}, whereas they peak between 3600 cm^{-1} and 3750 cm^{-1} when they act as proton donors to acid molecules. Peaks of free O-H bonds not involved in any interactions are found between 3850 cm^{-1} and 3950 cm^{-1}.

4. CONCLUSION

Nitric acid and sulfuric acid can form stable species with water molecules by creating various hydrogen bonds. These acid molecules are significant from an atmospheric perspective and play an important role in atmospheric chemistry. In this theoretical study, interactions in clusters of these acids with two and three water molecules were analyzed at the M062X/aug-cc-pvdz level. The potential energy surfaces for $HNO_3 \cdots H_2SO_4 \cdots (H_2O)_2$ and $HNO_3 \cdots H_2SO_4 \cdots (H_2O)_3$ clusters were initially scanned using the ABCluster program. On the potential energy surface, 22 minimum energy points were obtained for $HNO_3 \cdots H_2SO_4 \cdots (H_2O)_2$ clusters and 38 minimum energy points for $HNO_3 \cdots H_2SO_4 \cdots (H_2O)_3$ clusters. In the NS2W clusters, neither sulfuric acid nor nitric acid was ionized. By adding one more water molecule to the system, ionic forms of sulfuric acid or nitric acid were obtained in the NS3W clusters. Literature studies exist on the number of water molecules required for acid molecules to ionize [49-51]. For example, it has been noted that ionization of HCl requires at least four water molecules. There are also studies examining HNO_3 with HCl in water clusters [52]. When HNO_3 replaces one water molecule, it was observed that HCl ionizes with three water molecules. The same study reported that HNO_3 ionizes in clusters containing four water molecules and HCl. In this study, sulfuric acid or nitric acid did not ionize in the NS2W clusters, where H_2SO_4 was examined with two water molecules and nitric acid. By adding a water molecule to the system, both ionic forms of nitric acid and sulfuric acid were obtained. The literature mentions only one study where sulfuric acid's ionic form is stable in a structure containing five water molecules with HNO_3 and H_2SO_4 [42]. However, no studies have been conducted on clusters with fewer water molecules.

When examining the binding energies of the clusters, it was found that both NS2W and NS3W clusters exhibit the most stable structures, with nitric acid acting as a proton donor to sulfuric acid. This result is consistent with previous studies on $HNO_3 \cdots H_2SO_4 \cdots H_2O$ ternary clusters [40]. Generally, hydrogen bonds are found to enhance the stability of the clusters, and cyclic structures in which each molecule in the cluster donates and accepts a proton are more energetically stable. Structural and spectroscopic analyses have shown that the strength of hydrogen bonds varies according to the proton donation and acceptance states of the molecules within the cluster. For example, in the NS2W-1 structure, sulfuric acid interacts with three oxygen atoms, forming a three-coordinated structure. In this structure, the hydrogen bond between sulfuric acid and water has a length of 1.33 Å, and the O-H bond of sulfuric acid peaks at 1775 cm^{-1}. In the NS2W-3 structure, sulfuric acid is two-coordinated and does not interact with nitric acid. The hydrogen bond between sulfuric acid and the water molecule is 1.47 Å, and the O-H bond peaks at 2446 cm^{-1}. Therefore, in the NS2W-1 structure, where a strong hydrogen bond is formed, the O-H bond is more stretched. In another structure, NS3W-9, both protons of sulfuric acid participate in hydrogen bonding. The hydrogen bond distances for O5$\cdots$H1 and O9$\cdots$H2 are 1.39 Å and 2.04 Å, respectively, and their vibration frequencies are observed to be 2096 cm^{-1} (O1-H1) and 3632 cm^{-1} (O2-H2), respectively. A similar situation is also true for nitric acid. The stretching of the O-H bond changes depending on the strength of the hydrogen bond it forms. Another significant point of the study is that the hydrogen bonds between water molecules themselves are observed to be stronger than in cases where they act as proton donors to acid molecules.

ACKNOWLEDGEMENTS

CONFLICT OF INTEREST

The author stated that there are no conflicts of interest regarding the publication of this article.

CRediT AUTHOR STATEMENT

Fatime Mine Balcı: Conceptualization, Formal analysis, Investigation, Writing – Original Draft, Writing – Review & Editing, Methodology.

REFERENCES

[1]   Solomon S, Garcia RR, Rowland FS, Wuebbles DJ. On the depletion of Antartic ozone. Nature 1986; 321:755–758.

[2]   Solomon S. Stratospheric ozone depletion: a review of concepts and history. Rev Geophys 1999; 37 (3): 275–316.

[3]   Molina MJ, Zhang R, Wooldridge PJ, McMahon JR, Kim JE, Chang HY, Beyer KD. Physical chemistry of the $H_2SO_4/HNO_3/H_2O$ system: implications for polar stratospheric clouds. Science 1993; 261:1418-1423.

[4]   Wegner T, Kinnison DE, Garcia RR, Solomon S. Simulation of polar stratospheric clouds in the specified dynamics version of the whole atmosphere community climate model. J Geophys Res 2013; 118 (10):4991–5002.

[5]   Lowe D, MacKenzie AR. Polar stratospheric cloud microphysics and chemistry. JASTP 2008; 70 (1):13–40.

[6]   Finlayson-Pitts BJ., Pitts J.r JN. Chemistry of the Upper and Lower Atmosphere. 2000 Academic Press: New York.

[7]   Sipila M, Berndt T, Petaja T, Brus D, Vanhanen J, Stratmann F, Patokoski J, Mauldin RL, Hyvarinen AP, Lihavainen H, Kulmala M. The role of sulfuric acid in atmospheric nucleation. Science 2010; 327:1243−1246.

[8]   Yu F, Turco RP. Ultrafine aerosol formation via ion-mediated nucleation. Geophys Res Lett 2000; 27 (6):883−886.

[9]   Korhonen P, Kulmala M, Laaksonen A, Viisanen Y, McGraw R, Seinfeld JJ. Ternary nucleation of H_2SO_4, NH_3 and H_2O in the atmosphere. J Geophys Res 1999; 104: 26349−26353.

[10]   Zhang R, Suh I, Zhao J, Zhang D, Fortner EC, Tie X, Molina LT. Atmospheric new particle formation enhanced by organic acids. Science 2004; 304:1487−1490.

[11] Zhang R, Wooldridge PJ, Molina MJ. Vapor pressure measurements for the $H_2SO_4/HNO_3/H_2O$ and $H_2SO_4/HCl/H_2O$ systems: incorporation of stratospheric acids into background sulfate aerosols. J Phys Chem A 1993; 97:8541–8548.

[12] Tabazadeh A, Turco RP, Drdla K, Jacobson MZ. A study of type I polar stratospheric cloud formation. Geophys Res Lett 1994; 21 (15):1619–1622.

[13] Hanson DR. Reaction of $ClONO_2$ with H_2O and HCl in sulfuric acid and $HNO_3/H_2SO_4/H_2O$ mixtures. J Phys Chem A 1998; 102:4794–4807.

[14] Ritzhaupt G, Devlin JP. Infrared spectra of nitric and hydrochloric acid hydrate thin films. J Phys Chem 1991; 95:90.

[15] Tolbert MA, Middlebrook AM. Fourier transform infrared studies of model polar stratospheric cloud surfaces: Growth and evaporation of ice and nitric acid/ice. J Geophys Res 1990; 95:22423.

[16] Barton N, Rowland B, Devlin JP. Infrared spectra of large acid hydrate clusters: Formation conditions of submicron particles of $HNO_3.2H_2O$ and $HNO_3.3H_2O$. J Phys Chem 1993; 97:5848.

[17] Escribano R, Couceiro M, Gomez PC, Carrasco E, Moreno MA, Herrero VJ. The nitric acid hydrates: ab initio molecular study, and RAIR Spectra of the Solids. J Phys Chem A 2003; 107 (5):651-661.

[18] Fernandez-Torre D, Escribano R, Archer T, Pruneda JM, Artacho E. First-principles infrared spectrum of nitric acid and nitric acid monohydrtae crystals. J Phys Chem A 2004; 108: 10535.

[19] Leopold KR. Hydrated Acid Clusters. Annu Rev Phys Chem 2011; 62:327-349.

[20] Devlin JP, Uras N, Sadlej J, Buch V. Discrete stages in the solvation and ionization of hydrogen chlorie adsorbed on ice particles. Nature 2002; 417 (6886):269-271.

[21] Buch V, Sadlej J, Aytemiz-Uras N, Devlin JP. Solvation and ionization of stages of HCl on ice nanocrystals. J Phys Chem A 2002; 106 (41):9374-9389.

[22] Ortiz-Repiso M, Escribano R, Gomez PC. Structure and spectra of $HOCl(H_2O)_n$ clusters, n = 1−4: a theoretical calculation. J Phys Chem A 2000; 104 (3):600-609.

[23] Riikonen S, Parkkinen P, Halonen L, Gerber RB. Ionization of Nitric Acid on Crystalline Ice: The Role of Defects and Collective Proton Movement. J Phys Chem Lett 2013; 4: 1850-1855.

[24] Dimitrova Y. Structure, stability and vibrational spectrum of the hydrogen-bonded complex between HNO_3 and H_2O ab initio and DFT studies. Spectrochim Acta A Mol Biomol Spectrosc 2004; 60 (1):1-8.

[25] Tao F-M, Higgins K, Klemperer W, Nelson DD. Structure, binding energy, and equilibrium constant of the nitric acid-Water complex. Geophys Res Lett 1996; 23(14):1797-1800.

[26] Scott JB, Wright J. Computational investigation of the solvation of nitric acid: formation of the NO_3^- and H_3O^+ ion pair. J Phys Chem A 2004; 108(47):10578-10585.

[27] Canagaratna M, Phillips JA, Ott ME, Leopold KR. The nitric acid−water complex: Microwave Spectrum, Structure, and Tunneling. J Phys Chem A 1998; 102(9):1489-1497.

[28] Staikova S, Donaldson DJ. Ab initio investigation of water complexes of some atmospherically important acids: HONO, HNO_3 and HO_2NO_2. Phys Chem Chem Phys 2011; 3(11):1999-2006.

[29] McCurdy PR, Hess WP, Xantheas SS. Nitric acid-water complexes: Theoretical calculations and comparison to experiment. J Phys Chem A 2002; 106(33):7628-7635.

[30] Balcı FM, Uras-Aytemiz N. Interaction in the ternary complexes of $HNO_3 \cdots HCl \cdots H_2O$: a theoretical study on energetics, structure, and spectroscopy. J Phys Chem A 2011; 115(23):5943-5954.

[31] Kuczkowski RL, Suenram RD, Lovas FJ. Microwave spectrum, structure, and dipole moment of sulfuric acid. JACS 1981; 103:2561-2566.

[32] Re S, Osamura Y, Morokuma K. Coexistence of Neutral and Ion-Pair Clusters of Hydrated Sulfuric Acid $H_2SO_4(H_2O)_n$ (n =1-5)-A Molecular Orbital Study. J Phys Chem A 1999; 103:3535-3547.

[33] Partanen L, Hanninen V, Halonen L. Ab Initio Structural and Vibrational Investigation of Sulfuric Acid Monohydrate. J Phys Chem A 2012; 116:2867−2879.

[34] Miller Y, Chaban GM., Gerber RB. Ab Initio Vibrational Calculations for H_2SO_4 and $H_2SO_4.H_2O$: Spectroscopy and the Nature of the Anharmonic Couplings. J Phys Chem A 2005; 109:6565-6574.

[35] Kurten T, Sundberg MR, Vehkamaki H, Noppel M, Blomqvist J, Kulmala M. Ab Initio and Density Functional Theory Reinvestigation of Gas-Phase Sulfuric Acid Monohydrate and Ammonium Hydrogen Sulfate. J Phys Chem A 2006; 110:7178-7188.

[36] Bandy AR, Ianni JC. Study of the Hydrates of H_2SO_4 Using Density Functional Theory. J Phys Chem A 1998; 102:6533-6539.

[37] Al Natsheh A, Nadykto AB, Mikkelsen KV, Yu F, Ruuskanen J. Sulfuric Acid and Sulfuric Acid Hydrates in the Gas Phase: A DFT Investigation. J Phys Chem A 2004; 108: 8914-8929.

[38] Balcı FM. Theoretical investigation of hydrogen bonding in the $H_2SO_4 \cdots HNO_3$ system. Comput Theor Chem 2017; 1117:41-46.

[39] Beichert P, Schrems O. Complexes of Sulfuric Acid with Hydrogen Chloride, Water, Nitric Acid, Chlorine Nitrate and Hydrogen Peroxide: An ab Initio Investigation. J Phys Chem A 1998; 102:10540-10544.

[40] Balcı FM, Uras-Aytemiz N. A detailed hydrogen bonding analysis on the compositions of $H_2SO_4/HNO_3/H_2O$ ternary systems: A computational study. J Mol Graph Model 2018; 80:272-281.

[41] Verdes M, Paniagua M. Quantum chemical study of atmospheric aggregates: $HCl.HNO_3.H_2SO_4$. J Mol Model 2014; 20:2232.

[42] Verdes M, Paniagua M. Facet shapes and thermo-stabilities of $H_2SO_4 \bullet HNO_3$ hydrates involved in polar stratospheric clouds. J Mol Model 2015; 21:238.

[43] Frisch MJ, Trucks GW, Schlegel HB. et al., Gaussian 09, Revision E.01, Gaussian, Inc., Wallingford CT, 2016.

[44] Xantheas SS, Dunning TH. Ab initio studies of cyclic water clusters $(H_2O)_n$, n=1–6. I. Optimal structures and vibrational spectra. J Chem Phys 1993; 99:8774.

[45] Cox A, Riveros J. Microwave Spectrum and Structure of Nitric Acid. J Chem Phys 1965; 42:3106-3112.

[46] Benedict WS, Gailar N, Plyler EK. Rotation-Vibration Spectra of Deuterated Water Vapor. J Chem Phys 1956; 24:1139-1165.

[47] Zhang J, Dolg M. ABCluster: the artificial bee colony algorithm for cluster global optimization. Phys Chem Chem Phys 2015; 17:24173–24181.

[48] Zhang J, Dolg M. Global optimization of clusters of rigid molecules using the artificial bee colony algorithm. Phys Chem Chem Phys 2016; 18:3003–3010.

[49] Milet A, Struniewicz C, Moszynski R. Theoretical study of the protolytic dissociation of HCl in water clusters. J Chem Phys 2011; 115:349-356.

[50] Re S, Osamura Y, Suzuki Y, Schaefer III HF. Structures and stability of hydrated clusters of hydrogen chloride, $HCl(H_2O)_n$, n= 1–5. J Chem Phys 1998; 109:973-977.

[51] Buch V, Milet A, Vacha R, Jungwirth P, Devlin JP, Water surface is acidic. Proc Natl Acad Sci U.S.A 2007; 104:7342-7.

[52] Balcı FM, Uras-Aytemiz N, Gomez PC, Escribano R. Proton transfer and autoionization in $HNO_3HCl(H_2O)_n$ particles. Phys Chem Chem Phys 2011; 13:18145-18153.

RESEARCH ARTICLE

INVESTIGATION OF X-RAY SOURCES IN NGC 7552: IDENTIFICATION OF A NEW ULX CANDIDATE

Sinan ALLAK [1, *], Aysun AKYUZ [1, 2]

[1] Space Science and Solar Energy Research and Application Center (UZAYMER), University of Çukurova, 01330, Adana, Turkey
0417allaksinan@gmail.com- *0000-0001-7093-1079*

[2] Department of Physics, University of Çukurova, 01330, Adana, Türkiye
aakyuz@cu.edu.tr- *0000-0001-9533-9805*

Abstract

This study investigates the X-ray and optical properties of 29 X-ray sources within the NGC 7552 galaxy, using *Chandra*, Swift X-Ray Telescope (*Swift-XRT*) data, and *Hubble Space Telescope* (*HST*). A significant finding was the identification of a new ultraluminous X-ray source (ULX-3) with an X-ray luminosity, $L_X \approx 10^{39}\ erg\ s^{-1}$ making it the third ULX identified in this galaxy. The spectral analysis of ULX-3 suggests it could be a stellar-mass black hole with an estimated mass of around 8 solar masses ($M_\odot$). Nearly half of the observed X-ray binaries (XRBs) were classified as transient or variable. Variability studies revealed that ULX-1 exhibited significant long-term variability in *Chandra* data, while ULX-2 remained stable in both *Chandra* and *Swift-XRT* observations. ULX-3 showed no significant variability in *Chandra* data, indicating steady emissions during the observation period. The analysis of the X-ray energy spectra for ULX-1, ULX-2, and ULX-3 showed that power-law models best described their spectra. These findings suggest that the ULXs have a hard spectral structure, commonly linked to X-ray emissions from compact objects such as black holes or neutron stars. Optical counterparts were also identified for several XRBs, including ULX-1, ULX-2, and ULX-3, most of which exhibit faint optical magnitudes (m_V >22 mag) characteristic of ULX systems.

1. INTRODUCTION

X-ray binaries (XRBs) are systems where two stars orbit a common center of mass, consisting of a compact object and a companion star (donor). This compact object can be a neutron star (NS), a black hole (BH), or a white dwarf (WD). XRBs can generally be classified into two different types based on the mass of the donor star: (1) High-mass X-ray binaries (HMXBs, $\geq 10\ M_\odot$) and (2) Low-mass X-ray binaries (LMXBs, ($\leq 1\ M_\odot$). HMXBs typically involve an O or B-type star whose optical/UV brightness is comparable to or greater than that of the X-ray source. The X-ray emission in these systems results from wind accretion, where mass is transferred from the early-type, mass-losing star to the compact star. Additionally, although rare, mass transfer can also occur through Roche lobe overflow in these systems [1]. Furthermore, HMXBs containing an NS may include a Be star (Be/X-ray binary) and a supergiant (SG/X-ray binary). In LMXBs, mass transfer occurs via Roche lobe overflow. Low-mass donor stars can include white dwarfs, late-type main-sequence stars, and F-G-

type subgiants. LMXBs are relatively faint in the optical wavelengths. The emission in the optical region in LMXBs is primarily driven by the radiation from an accretion disk around the compact star. The contribution of the donor star to the emission is generally negligible. In XRBs with an NS, X-ray pulsations can be observed. The NS's strong magnetic field channels the transferred mass to its magnetic poles, creating a bright X-ray hotspot when the mass strikes the hard surface. If the NS's rotational and magnetic axes are not aligned, the emission will be visible once per rotation, resulting in X-ray pulsations. These systems are known as X-ray pulsars. XRBs typically exhibit X-ray luminosities ranging from about $10^{37}-10^{39}$ erg/s, depending on the type of system and the characteristics of the compact object. Moreover, some XRBs exhibit much higher luminosities, ranging from $10^{39} - 10^{41}$ erg/s. These are known as ultraluminous X-ray sources (ULXs).

ULXs are point-like sources located outside the nuclei of their host galaxies, exhibiting X-ray luminosities exceeding 10^{39} erg s^{-1} [2]. ULXs were first discovered in the 1980s by the Einstein Observatory. They began to be better understood with the construction of X-ray observatories with relatively better spectral characteristics, such as *ROSAT*. Recently, next-generation X-ray observatories like *Chandra* and *XMM-Newton* have provided even more information about the spectral and temporal characteristics, and especially the nature, of these sources. Initially, ULXs were thought to be intermediate-mass black holes (IMBHs) with masses in the range of 10^2 - $10^4 M_\odot$, assuming their emission and accretion rates were isotropic and limited by Eddington luminosity [3]. Subsequent studies suggested that the primary source of luminosity might be an accretion disk surrounding a compact object in binary systems, potentially exceeding the Eddington limit for X-ray emission [4, 5]. Although there is not yet an identified ULX in our galaxy, Swift J0243.6+6124, which is well-studied and whose compact object has been identified as a neutron star (NS), is a strong candidate for a Galactic ULX.

Theoretical models and population synthesis studies have proposed that the majority of ULXs might contain highly magnetized NSs [6]. They proposed that pulsating ULXs are not strongly beamed, and thus their observed luminosities should be close to their actual luminosities. King et al ([1]) attributed the low number of discovered pulsars ULXs to the fact that magnetic neutron stars emit observable signals only for a short part of their lifetimes. They suggest that a much larger fraction of ULXs, beyond the number of currently discovered pulsar ULXs, may have NS as their compact objects. This interpretation has been reinforced by the discovery of NSs in these systems since 2014 [7], indicating that the ULX population predominantly consists of compact objects accreting at super-Eddington rates [7-12]. Many ULXs can exhibit steady luminosity for several years or even decades. However, some may show significant flux variations on short timescales. Some can completely fade away on the order of days or months and then re-emit at ULX levels [13]. Such sources are called transient ULXs. In some cases, notable flux variability in ULXs can be attributed to the accretion process being halted at the magnetospheric radius of the NS, a phenomenon referred to as the propeller effect [13,14]. Another scenario proposed to explain the variability that these sources may be observed during outbursts of LMXBs [15].

Using ground-based observations and the *Hubble Space Telescope (HST)* along with high-resolution *Chandra* observations, the optical counterparts of ULXs can be determined [13,16]. The emission from the optical counterparts of ULXs may originate from the donor star, the outer part of the accretion disk, or both [17,18]. Photometric and spectroscopic observations allow for detailed characterization of the donor's spectral type, age, metallicity, mass, and the physical conditions of the local environment [19, 20]. ULXs typically have faint optical counterparts (>22 magnitudes). The absolute magnitudes of the identified optical counterparts have been calculated to range between -4 < M_V < -9 [21].

The number of identified ULXs continues to grow with new, more sensitive multiwavelength observations. As the ULX population expands, so does the potential to uncover the physical properties

and emission mechanisms of these sources. Our study aims to explore the X-ray population in NGC 7552, with a particular focus on investigating the X-ray and optical properties of ULXs using additional datasets. The enhanced understanding of these features may provide deeper insights into the nature of ULXs, contributing to the broader knowledge of their formation, evolution, and interaction with their host galaxies. NGC 7552 is a starburst ringed, face-on barred spiral galaxy with an inclination of 28 degrees [22]. Throughout this study, the distance to the galaxy NGC 7552, which is morphologically classified as SBbc(s), is assumed to be 19.5 Mpc [23]. Classified mostly as a LINER galaxy [24] this galaxy has not shown significant activity in either X-ray or near-infrared (NIR) band observations of its core [23]. ULX-1 in this galaxy was identified using *ROSAT* observations [25]. Later, using *Chandra* images from 2007, [26] identified ULX-1 and ULX-2 sources, highlighting the bright X-rays. The main objective of this study is to reveal the spectral and temporal properties of the bright X-ray sources within the D_{25} area of the NGC 7552 galaxy using *Chandra* and *Swift-XRT* observations. Additionally, determining their optical counterparts using *HST* archival data and reporting photometric results is another primary goal of this study. For this galaxy, unlike previous studies, more *Chandra* and *Swift-XRT* X-ray observations were used, and for the first time in this study, the properties of the X-ray sources were examined using optical wavelengths.

This paper is organized into three main sections. Section 2 details the reduction and analysis of X-ray and optical data obtained from *Chandra*, *Swift-XRT*, and the *HST*. Section 3 presents the spectral and temporal analysis of 29 X-ray sources in the NGC 7552 galaxy, including a focus on ULX-1, ULX-2, and the newly identified ULX-3, along with their optical counterparts. Finally, Section 4 summarizes the findings, highlighting the new insights gained into the nature and evolution of ULXs.

2. MATERIALS AND METHODS

NGC 7552 has been observed multiple times over 17 years by the *XMM-Newton, Chandra,* and *Swift-XRT X-ray* observatories. As shown in Figure 1, XMM-Newton observations were excluded due to their insufficient spatial resolution, making it difficult to resolve most sources. Moreover, these observations are affected by high background noise and frequent flaring events. Using *Chandra* observations, 29 X-ray sources have been identified within the D_{25} area. Additionally, different regions of the galaxy have been observed with high-resolution *HST* optical detectors. The *HST, Chandra*, and *Swift-XRT* observations used in this study are listed in Table 1. The data reduction and analysis of these observations are detailed in the following sections.

Table 1. X-ray and optical observations of NGC 7552

Instrument	ObsID	Date	Exp. time	
Swift-XRT	46279002	2012-11-07	1.8	
Swift-XRT	46279003	2012-11-08	4.8	
Swift-XRT	46279004	2012-11-10	1.2	
Swift-XRT	46279005	2012-11-11	0.9	
Swift-XRT	46279006	2012-11-16	0.7	
Swift-XRT	46279007	2012-11-18	0.4	
Swift-XRT	46279008	2012-11-20	1.5	
Swift-XRT	46279009	2013-01-07	0.8	
Swift-XRT	10041001	2017-04-04	1.2	
Swift-XRT	10041002	2017-04-08	1.9	
Swift-XRT	10041003	2017-04-12	0.8	
Swift-XRT	10041004	2017-04-16	1.5	
Swift-XRT	10041005	2017-04-20	0.7	
Swift-XRT	10041006	2017-04-21	1.1	
Swift-XRT	10041007	2017-04-23	1.8	
Swift-XRT	10041008	2017-04-29	1.6	
Swift-XRT	10041009	2017-05-06	1.4	
Swift-XRT	10041010	2017-05-10	0.5	
Swift-XRT	3104723001	2018-06-06	0.4	
Swift-XRT	3104723004	2018-07-18	1.6	
Swift-XRT	88883001	2018-07-18	2.2	
Chandra/ACIS-S	7848	2007-03-31	5.0	
Chandra/ACIS-S	20268	2018-08-20	12.0	
Chandra/ACIS-S	20267	2018-08-21	57.0	
Chandra/ACIS-S	21675	2018-08-24	65.0	
Chandra/ACIS-S	21676	2018-08-24	66.0	
				Filter
HST/WFPC2	ubah3301m	2009-05-05	60.5	F439W
HST/WFPC2	ubah330bm	2009-05-05	65.6	F555W
HST/WFPC2	ubah330cm	2009-05-05	65.6	F814W
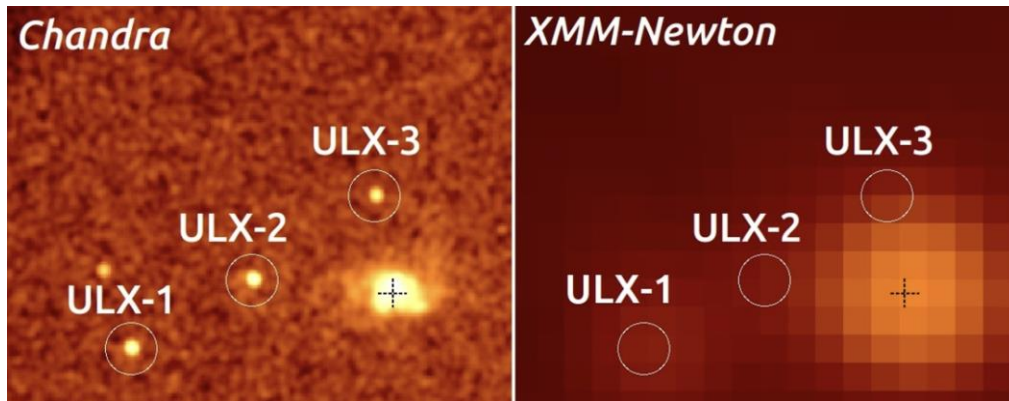
Figure 1. A detailed view of the ULX positions on *Chandra* (left) and *XMM-Newton* (right) images.

2.1. X-ray Data Reduction and Analysis

Chandra ACIS-S observations were analyzed using the *Chandra Interactive Analysis of Observations (CIAO)* v4.14 software and calibration files *CALDB* v4.9.6. The observation files were prepared for analysis using the *CIAO chandra_repro* packages. Using *Chandra* data, 29 X-ray sources were identified within the D_{25} area. The right panel of Figure 2 shows these sources on the X-ray RGB (Red: Green: Blue) image. The sources were numbered in ascending order of *Chandra* cumulative counts. Spectral, temporal, and statistical (photon count rate) analyses were performed by selecting both the source and background regions using circles with a radius of 5 arcseconds (")
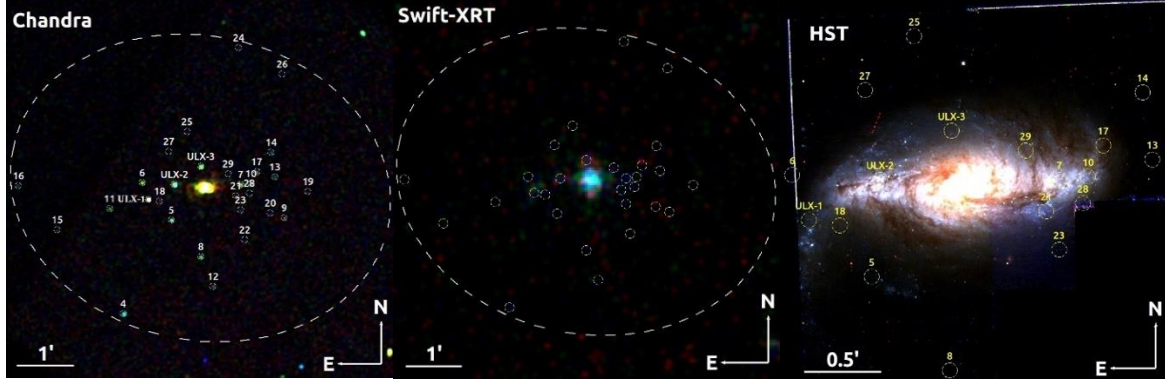

Figure 2. Three-color (RGB, R: red; G: green; B: blue) images of the NGC 7552 galaxy from *Chandra* (Observation ID 21676) (left), *Swift-XRT* (a combination of 2012 observations) (center), and HST (right). The *Chandra* and *Swift-XRT* RGB images were created using energy bands of 0.3-1 keV, 1-2 keV, and 2-8 keV, respectively, while the HST RGB image was composed using the F814W, F555W, and F435W filters. The large dashed ellipse represents the D_{25} region, and the smaller dashed hollow circles indicate the positions of the X-ray sources.

Source spectra and light curves were obtained using the specextract and dmextract packages, respectively. Additionally, spectra from 2018 *Chandra* data with closely spaced observation dates were combined using the combine_spectra package. This process enabled the analysis of the spectral and temporal properties of faint sources with low photon counts.

Spectral analyses were performed using the XSPEC v12.8.2 software. Based on the total source counts, the source energy spectra were grouped with a minimum of 10 counts per energy bin. Count rates and spectra for all detectors were obtained in the 0.3-10 keV energy range. Fundamental models for XRBs, such as the power-law and diskbb models, were applied to the source spectra. Additionally, combined models like the power-law+diskbb model were also applied. An absorption column component (TBABS) was included in these models.

Photon count rates for *Swift-XRT* in PC (Photon Counting) mode were obtained using the automated procedures specified on the website [27]. Due to the typically short exposure time of *Swift-XRT* observations, the data are statistically insufficient for model application. Therefore, *Swift-XRT* observations were used only for temporal analyses in this study.

The short-term and long-term characteristics of X-ray sources provide significant insights into their nature. Some sources can exhibit flux variations of more than 50 times over the long term [13]. These variations can provide crucial insights into the types of compact objects they contain. For instance, the high flux variations observed in pulsar ULXs typically display a bi-modal distribution. This is often an indication of a mechanism known as the propeller effect [28, 29]. This effect occurs directly when the compact objects are NSs. Additionally; short-term variations are examined for pulsar-like signals or quasi-periodic oscillations (QPO). These analyses can also indicate of whether the compact object is a

neutron star or a black hole. In this study, short-term and long-term flux variations were examined to investigate such characteristics of X-ray sources.

For short-term analyses, light curves were produced using *Chandra* datasets cleaned from the background in the 0.3-10 keV energy range. For long-term light curves, count rates ($count\ s^{-1}$) from *Chandra* and *Swift-XRT* observations in the 0.3-10 keV energy range were used. Long-term variations were calculated using the 2007 and combined 2018 *Chandra* observations. The variability of the sources was calculated using *Chandra* data, owing to its superior pixel resolution. Based on these two datasets, X-ray sources were classified as variable if the variation factor (V_f), defined as the ratio of the highest flux to the lowest flux, was ≥3. Table 2 shows the X-ray sources identified within the D_{25} region of the NGC 7552, along with their coordinates in degrees and their variation factors. Moreover, long-term variations of sources, including ULXs, were examined using *Swift-XRT* observations. However, light curves for all sources were not generated, as not all sources were resolved by the *Swift-XRT* detector and/or due to their transient nature. High-quality observations with strong data statistics are particularly needed to investigate pulsar-like strong signals.

Table 2. The X-ray sources located within the D_{25} region of the NGC 7552 are described by their coordinates, fluxes (F_X), and variability factors (V_f).

Source No.	RA	Decl.	F_X	V_f
	(°)	(°)	$(10^{-14} erg\ cm^{-2} s^{-1})$	(T=Transit)
ULX-1	349.0674	-42.5884	6.2 ± 0.1	4.1
ULX-2	349.0569	-42.5840	10.2±0.1	1.2
ULX-3	349.0463	-42.5787	2.22±0.01	1.8
X4	349.0774	-42.6222	1.42±0.4	1.2
X5	349.0581	-42.5945	0.91±0.3	1.3
X6	349.0699	-42.5835	0.71±0.3	1.7
X7	349.0304	-42.5840	0.68±0.2	T
X8	349.0464	-42.6054	0.62±0.2	1.1
X9	349.0129	-42.5940	0.48±0.2	T
X10	349.0262	-42.5837	0.46±0.2	1.4
X11	349.0830	-42.5912	0.41±0.1	1.6
X12	349.0415	-42.6142	0.37±0.1	T
X13	349.0167	-42.5818	0.34±0.2	T
X14	349.0181	-42.5745	0.34±0.1	1.7
X15	349.1040	-42.5974	0.32±0.1	2.5
X16	349.1196	-42.5844	0.31±0.1	2.8
X17	349.0239	-42.5803	0.28±0.1	1.2
X18	349.0628	-42.5890	0.22±0.1	T
X19	349.0033	-42.5861	0.18±0.1	2.5
X20	349.0184	-42.5925	0.17±0.01	1.6
X21	349.0323	-42.5874	0.15±0.01	1.5
X22	349.0288	-42.6004	0.15±0.01	3.4
X23	349.0304	-42.5916	0.15±0.01	2.3
X24	349.0312	-42.5435	0.13±0.01	T
X25	349.0518	-42.5684	0.13±0.01	T
X26	349.0137	-42.5514	0.11±0.01	T
X27	349.0591	-42.5743	0.10±0.01	1.2
X28	349.0269	-42.5866	0.07±0.01	4.7
X29	349.0354	-42.5809	0.07±0.01	1.1

However, to examine short-term count rates, background-subtracted Chandra light curves were produced in the 0.3-10 keV energy range with time intervals of 3.14 seconds. No sources showing significant short-term variations were found. To gain further insights into the nature of all these sources, new observations with high data statistics are required.

2.2. Optical Data Reduction and Analysis

NGC 7552 was observed by *HST* in 2009 using *WFPC2/WFC* (*The Wide Field and Planetary Camera 2/ The Wide Field Camera*). In this study, the F439W, F555W, and F814W filters were utilized. The details of the observations are provided in Table 1. High-resolution *Chandra* and *HST* images are frequently used to identify the optical counterparts of XRBs. However, none of the X-ray sources in the NGC 7552 galaxy matched any sources identified in the *HST* optical images. Therefore, relative astrometry was indirectly performed between *Chandra* and *HST* using the *GAIA R2* optical catalog. Two reference sources were identified between *Chandra* and *GAIA*. Using these reference sources, errors for right ascension (*R.A*) and declination (*Decl.*) were determined between the two images. These errors are defined based on the standard deviation calculation using the offsets between the reference sources. Subsequently, 10 reference sources were selected between *GAIA* and *HST*, and errors were calculated for R.A and Decl., respectively.

Astrometric calculations were performed following the method from our previous studies [30]. As a result, the optical coordinates and errors of the X-ray sources were calculated. *Chandra* (5932) and *HST WFPC2/WFC* (F555W) images were used for astrometric corrections. Sources were identified using the *wavedetect* and *IRAF/daofind* packages. All identified reference sources are shown in Figure 3. The root mean square of the total errors between *Chandra* and *GAIA* and between *GAIA* and *HST* provides an astrometric error radius of 0.34" with 90% confidence. Within the astrometric error radius, only the sources X8, X16, X17, ULX-1, ULX-2, and ULX-3 were found to have optical counterparts.
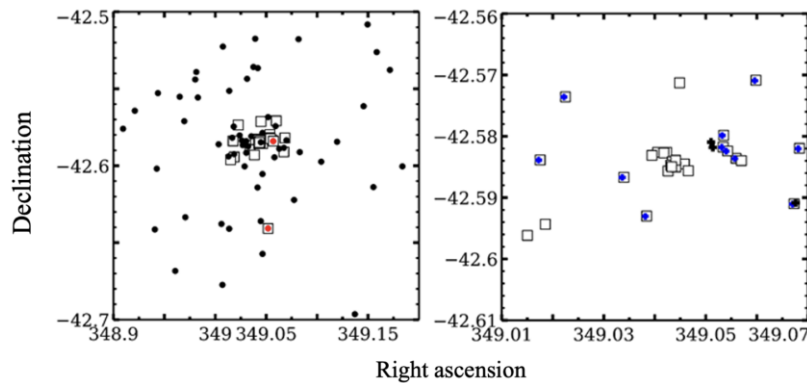
Figure 3. Left panel: The coordinates of *Chandra* and *GAIA* sources are represented by filled circles and hollow squares, respectively. The references between Chandra and *GAIA* are shown as red filled circles. Right panel: The coordinates of *GAIA* and *HST* sources are represented by hollow squares and dark crosses, respectively. The reference sources between these two images are represented by blue crosses.

The photometric analyses of these optical counterparts were performed using the *APPHOT* package in the *IRAF* software. Circles with radii of 3 and 12 pixels were selected for the source and background, respectively. Aperture correction was also carried out for each filter using 25 isolated and bright sources with radii ranging from 3 pixels to 24 pixels. Accordingly, the aperture corrections for the F439W (B), F555W (V), and F814W (I) filters were calculated as -0.32, -0.28, and -0.24 magnitudes, respectively. The resulting magnitudes were then corrected for extinction (A_V) using a value of $A_V = 0.04$ magnitudes from the study by [31]

Color-magnitude diagrams (CMDs) of *F439W-F555W* versus *F555W* and *F555W-F814W* versus F814W were generated to estimate the ages and masses of the optical counterparts [36]. *PARSEC* isochrones were employed in the CMDs. The metallicity and distance modulus of NGC 7552 were set to solar metallicity (Z = 0.02) and 31.45 magnitudes, respectively, for CMD construction. The *PARSEC* isochrones were corrected with an extinction value of $A_V = 0.04$. In generating the CMDs, it was assumed that the optical emission originated entirely from the donor star.

3. RESULTS AND DISCUSSION

3.1. X-ray

The X-ray and optical properties of the X-ray sources within the NGC 7552 galaxy have been investigated using *Chandra, Swift-XRT,* and *HST* data spanning over 17 years. Using *Chandra* data, 29 X-ray sources were identified within the D_{25}. These sources do not correspond to any cataloged AGN, background galaxy, or foreground star. All sources, including the previously identified ULX-1 and ULX-2, were analyzed using *Chandra* and *Swift-XRT* archival data sets. The previously identified ULX-1 and ULX-2 in the NGC 7552 galaxy were examined using combined *Chandra* spectra from the studies of [25, 26] which utilized *ROSAT* and 2007 *Chandra* data. The luminosity values for these sources are nearly identical to those calculated in this study. Although study [26] used a distance of 21.6 Mpc for the NGC 7552 galaxy, compared to 19.5 Mpc here, the results remain consistent. This similarity can be attributed to the combination of 2018 *Chandra* spectra, which improved the data statistics with a total observation time of 200 ks. The *power-law* model parameters and luminosity values that best represent the spectra of these two sources are shown in Table 3. Throughout this study, models with a reduced chi-square (*χ2*) value of 0.75-1.50 were considered the best fits. The photon indices (*Γ*) of ULX-1 and ULX-2, 1.8 and 2.4 respectively, are consistent with a hard state characterized by non-thermal emission [32-35].

One of the most significant outcomes of this study is the identification of a third ULX candidate in the NGC 7552 galaxy. In previous studies [26], the luminosity values of source X17 (hereafter referred to as ULX-3) were calculated to be below the ULX level of luminosity. Using the combined 2018 *Chandra* spectrum and the best-fitting *power-law* model, its luminosity in the 0.3-10 keV range has been calculated to be $L_X = 1.1 \times 10^{39}$ erg s^{-1}. This value classifies this source a ULX candidate. The *power-law* model parameter that best represents its energy spectrum was calculated as Γ=1.9 (see Table 3). Assuming accretion at Eddington luminosities, the compact object's mass was found to be ~ $8M_\odot$, indicating a stellar-mass black hole. Figure 4 shows the energy spectra of ULX-1, 2, and 3 fitted with the *power-law* model.

Table 3. *Power-law* model parameters that best represent the energy spectra of the ULX candidates.

Source	N_H	Np	Γ	F_X	L_X	*χ2/dof*
	10^{22}	10^{-5}		10^{-14}	10^{39}	
ULX-3	4.5 ± 0.4	3.8 ± 1.6	1.9 ± 0.5	2.2 ± 0.1	1.1 ± 0.1	28.2/30
ULX-2	0.2 ± 0.0	1.6 ± 0.4	1.8 ± 0.2	10.2 ± 0.1	4.6 ± 0.1	62.2/85
ULX-1	0.1 ± 0.0	1.3 ± 0.2	2.4 ± 0.3	6.4 ± 0.1	2.9 ± 0.2	64.6/64

Note. N_H: Intrinsic X-ray absorption value in units of $10^{22} cm^{-2}$. N_P: Normalization parameter of power-law model in units of 110^{-5}. Γ is the photon index from the power-law model. F_X is unabsorbed fluxes in units of $10^{-13} erg\ cm^{-2} s^{-1}$. L_X is unabsorbed luminosities in units of $10^{39} erg\ s^{-1}$ 1 in the 0.3–10 keV energy range. χ2/dof is the reduced. All errors are at the 90% confidence level.
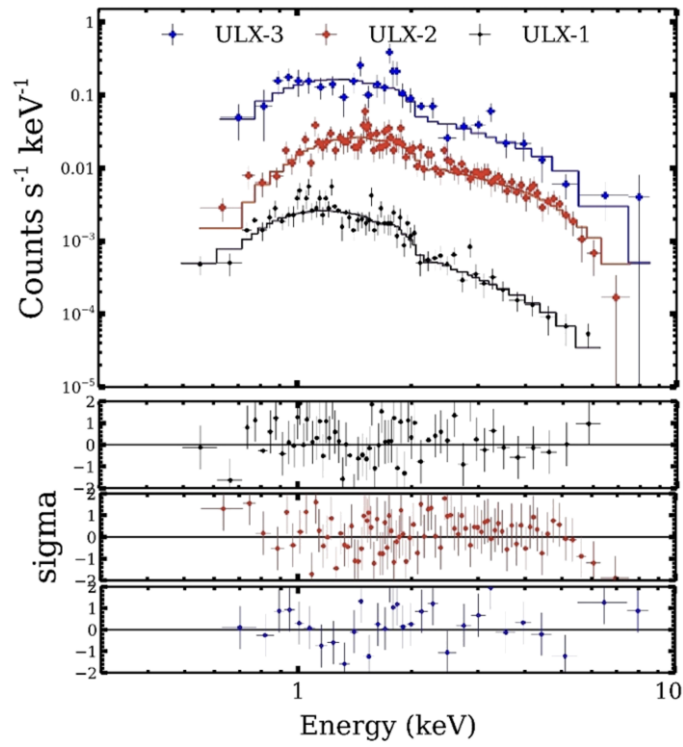
Figure 4. Energy spectra of three ULX candidates located in the NGC 7552 galaxy: ULX-3 (dark blue crosses), ULX-2 (dark red crosses), and ULX-1 (black crosses). The residuals from the fitting process are displayed in the bottom panels (data-model)/error.

Variability factors (V_f) were calculated using 2007 and combined 2018 *Chandra* data. Sources were defined as a variable when the variability factor $V_f \geq 3$ and sources detected in one observation but not in another were defined as transient (see Table 2). Accordingly, sources X16, X22, X28 and ULX-1 were considered variable. Additionally, X7, X9, X12, X13, X18, X24, X25, and X26 sources which were not detected in the 2007 *Chandra* data but were detected in the 2018 images, were defined as transient sources. Two of the three ULXs, ULX-2, and ULX-3, do not show any variability in long-term *Chandra* data. The long-term variability of the variable and transient sources, including the ULX candidates, was also investigated using *Swift-XRT* observations.

None of the transient sources were detected in any of the *Swift-XRT* observations. This could be due to the observations not having sufficiently long exposure times to detect these faint sources, or because their transient nature means they may have prevented them from emitting during these periods. Light curves created based on the count rate for sources ULX-1, ULX-2, ULX-3, X4, and X28 using *Swift-XRT* observations are shown in Figure 5. ULX-1 and ULX-2 did not show strong variability ($V_f \leq 3$) in the *Swift-XRT* observations. In contrast, ULX-3 which did not show significant variability in *Chandra* observations exhibited variability ($V_f \sim 6$) in *Swift-XRT* observations. X24 maintained its variable nature, while no significant changes were observed for X28 in these observations. Variable sources can remain constant during some periods.
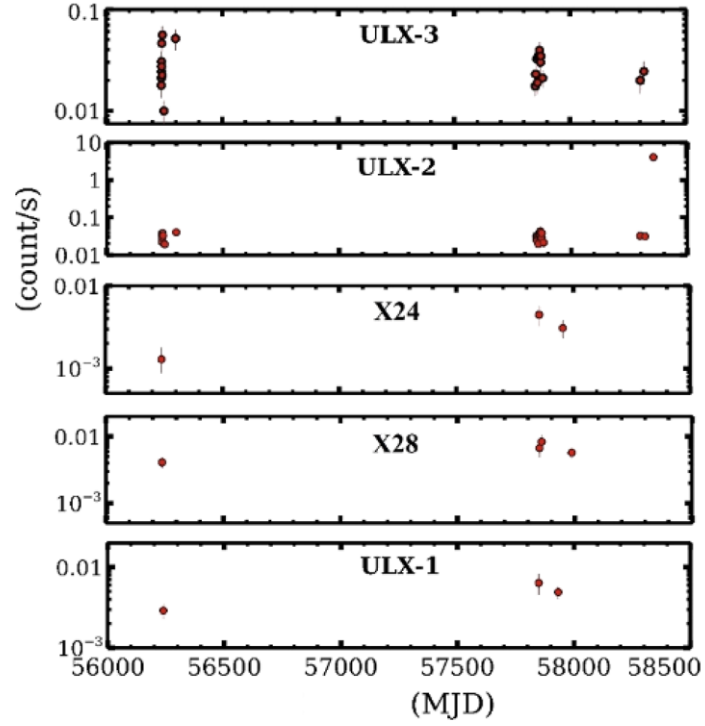
Figure 5. Long-term X-ray light curves of variable sources and those classified as ULX candidates were obtained using *Swift-XRT* observations.

3.2. Optical

Based on advanced astrometry from *Chandra*, *GAIA*, and *HST* observations, potential optical counterparts for the X-ray sources were identified. By examining the optical images listed in Table 1, optical counterparts for ULX-1, ULX-2, ULX-3, X5, X8, X13, X14, X21, and X29 were identified within an astrometric error radius of 0.34" with 90% confidence level. No optical counterparts were found within the astrometric error radius for the remaining sources. Figure 6 shows the position of the optical counterpart of ULX-3 on the *HST* image. Table 4 provides the coordinates and Vega magnitudes in three filters for the sources with identified optical counterparts.

Figure 6. The optical counterpart of ULX-3 is shown on the *HST* F439W image. The solid white circle represents the astrometric error region with a radius of 0.34".

Table 4. The counterparts and their Vega magnitudes in three filters.
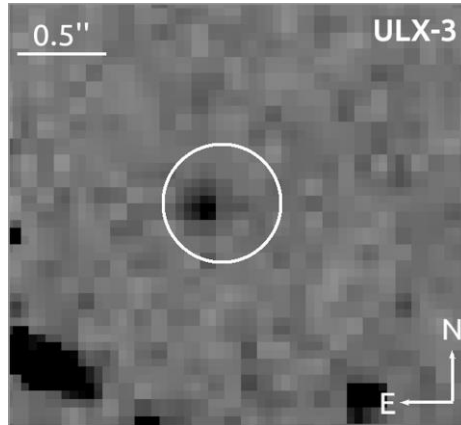
Filter/source	F439W	F555W	F814W
ULX-1	22.6 ± 0.4	22.20 ± 0.2	21.9 ± 0.3
ULX-2	19.8 ± 0.2	19.6 ± 0.2	19.4 ± 0.2
ULX-3	22.3 ± 0.3	…	21.5 ± 0.4
X5	…	…	24.8 ± 0.6
X8	23.4 ± 0.4	…	23.3 ± 0.5
X13	25.1 ± 0.7	24.2 ± 0.4	21.9 ± 0.2
X14	25.3 ± 0.6	23.5 ± 0.5	24.2 ± 0.5
X21	22.9 ± 0.7	22.8 ± 0.4	22.8 ± 0.7
X29	…	…	22.5 ± 0.5

All sources with identified optical counterparts must have sufficiently distinct and bright donor stars, as they were detected in at least one *HST* filter. For NGC 7552, at a distance of 19.5 Mpc, the lower detection limit for donor stars of XRBs in *HST* observations is likely greater than 8 $M_{\odot}$, which is the lowest mass calculated for the optical sources. This suggests that the sources can be classified as HMXBs. The lack of optical counterparts for the other sources is likely due to their faintness and small donor mass, suggesting they could be LMXBs [37]. On the other hand, analyses of James Webb Space Telescope observations have provided clues indicating that the donor stars of ULXs without identified optical counterparts may be embedded in dense, hot gas and dust [38-40]. Consecutive optical observations in different filters will provide critical insights into the optical emission mechanisms through analyses of optical temporal variability and spectral energy distributions. These observations will help determine whether the optical emission originates from the accretion disk, the donor star, or both.

The apparent magnitudes in the V-band (F555W) indicate that most ULX optical counterparts are faint, similar to other ULX counterparts [16-18]. The CMDs showing the ages and masses of the optical counterparts of ULXs, X14, and X21 are presented in Figure 7. These diagrams shows that the probable masses of the optical counterparts range from 8 to 30 $M_{\odot}$, with ages between 4 and 20 Myr.
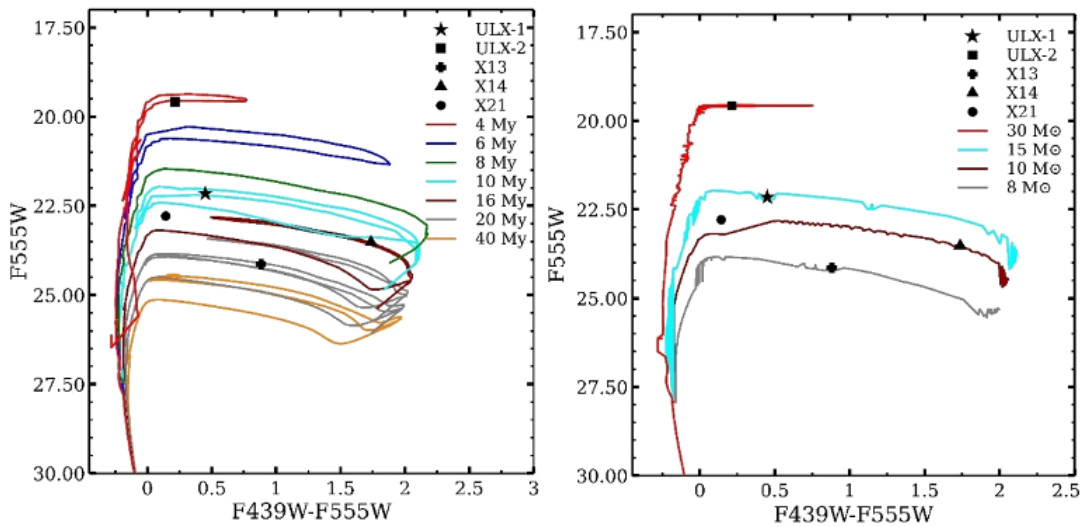

Figure 7. Color-magnitude diagrams (CMDs) of the identified optical counterparts of ULXs and XRBs. PARSEC isochrones of different ages (left panel) and masses (right panel) are overplotted. Isochrones have been corrected with an A_V=0.04 value.

4. CONCLUSION

Previous X-ray studies of the galaxy NGC 7552 have identified numerous bright X-ray sources, including ULX-1 and ULX-2 [26]. However, detailed analyses of other faint sources have not been conducted. In contrast, this study provides a thorough spectral and temporal analysis of 29 X-ray sources within the D25 field of the galaxy, utilizing a broader range of archival data. Our main findings are summarized as follows:

I. This study has provided a detailed analysis of the X-ray and optical properties of 29 XRBs within the NGC 7552 galaxy, leading to the discovery of a new ultraluminous X-ray source (ULX-3). This identification contributes to the growing understanding of X-ray sources within this galaxy.

II. Analysis of the energy spectrum suggests that ULX-3 is likely a stellar-mass black hole with an estimated mass of around 8 $M_\odot$. This supports the hypothesis that ULX-3 is a compact stellar-mass object exhibiting high-energy X-ray emissions.

III. ULX-1 exhibited significant long-term variability in *Chandra* data, indicating dynamic changes in its flux over time. In contrast, ULX-2 showed no significant variability in either *Chandra* or *Swift-XRT* observations, maintaining a stable luminosity throughout. Similarly, ULX-3 did not exhibit variability in *Chandra* data but displayed significant variability in *Swift-XRT* observations, suggesting that its variability may manifest over shorter timescales.

IV. Nearly 50% of the identified X-ray sources are either transient or variable. This finding suggests that the population of XRBs or ULXs appears to grow as galaxies are re-observed and re-examined.

V. Optical counterparts were identified for ULX-1, ULX-2, and ULX-3. These counterparts are consistent with the faint optical characteristics commonly associated with ULX systems. Therefore, high-quality, long-term, and simultaneous multiwavelength observations will be crucial for better understanding the emission mechanisms, particularly in determining whether the emission primarily originates from the donor star or other components such as the accretion disk. Such observations will also help refine the variability characteristics and physical properties of these ULXs, leading to a more comprehensive understanding of their nature.

ACKNOWLEDGEMENTS

CONFLICT OF INTEREST

The author(s) stated that there are no conflicts of interest regarding the publication of this article.

CRediT AUTHOR STATEMENT

Sinan Allak: Formal analysis, Writing – original draft, Visualization. **Aysun Akyuz**: Supervision, Project administration, Conceptualization.

REFERENCES

[1]   Lewin WHG, van Paradijs J, van den Heuvel EPJ. X-ray Binaries. Cambridge University Press 1997: 674.

[2] King A, Lasota, J.-P, and Middleton M, Ultraluminous X-ray sources. New Astronomy Reviewsvol. 2023; 96: 101672.

[3] Colbert EJM, Mushotzky RF. The nature of accreting black holes in nearby galaxy nuclei The Astrophysical Journal, 1999; 519: 89.

[4] Begelman MC. Super-Eddington Fluxes from Thin Accretion Disks? The Astrophysical Journal 2002; 568(2): L97–L100.

[5] Walton DJ. A Potential Cyclotron Resonant Scattering Feature in the Ultraluminous X-Ray Source Pulsar NGC 300 ULX1 Seen by NuSTAR and XMM-Newton. The Astrophysical Journal 2018; 857(1): L3.

[6] Mushtukov AA, Suleimanov VF, Tsygankov SS, Poutanen J. On the maximum accretion luminosity of magnetized neutron stars: connecting X-ray pulsars and ultraluminous X-ray sources. MNRAS 2015; 454(3): 2539–2548.

[7] Bachetti M. An ultraluminous X-ray source powered by an accreting neutron star. Nature, 2014; 514(521): 202–204.

[8] Fürst F. Discovery of Coherent Pulsations from the Ultraluminous X-Ray Source NGC 7793 P13. The Astrophysical Journal 2016; 831(2): L14.

[9] Israel GL. An accreting pulsar with extreme properties drives an ultraluminous x-ray source in NGC 5907. Science 2017; 355(6327): 817–819.

[10] Carpano S, Haberl F, Maitra C, Vasilopoulos G. Discovery of pulsations from NGC 300 ULX1 and its fast period evolution. MNRAS 2018; 476(1): L45–L49.

[11] Sathyaprakash R. The discovery of weak coherent pulsations in the ultraluminous X-ray source NGC 1313 X-2. MNRAS 2019; 488(1): L35–L40.

[12] Rodríguez Castillo GA. Discovery of a 2.8 s Pulsar in a 2 Day Orbit High-mass X-Ray Binary Powering the Ultraluminous X-Ray Source ULX-7 in M51. The Astrophysical Journal 2020; 895(1): 60.

[13] Allak S. The transient ultraluminous X-ray source, ULX-4, in M51. MNRAS 2022; 510(3): 4355–4369.

[14] Erkut MH, Ekşi KY, Alpar MA. Ultra-luminous X-Ray Sources as Super-critical Propellers. The Astrophysical Journal 2019; 873(2): 105.

[15] Earnshaw HP, Roberts TP, Sathyaprakash R. Searching for propeller-phase ULXs in the XMM-Newton Serendipitous Source Catalogue. MNRAS 2018; 476(3): 4272–4277.

[16] Allak S. Detection of 125.5-day optical periodic modulation of the neutron star M51 ULX-8. MNRAS 2022; 517(3): 3495–3504.

[17] Tao L, Feng H, Grisé F, Kaaret P. Compact Optical Counterparts of Ultraluminous X-Ray Sources. The Astrophysical Journal 2011; 737(2): 81.

[18] Gladstone JC. Optical Counterparts of the Nearest Ultraluminous X-Ray Sources. The Astrophysical Journal Supplement Series 2013; 206(2): 14.

[19] Kaaret P, Ward MJ, Zezas A. High-resolution imaging of the HeII λ4686 emission line nebula associated with the ultraluminous X-ray source in Holmberg II. MNRAS 2004; 351(3): L83–L88.

[20] Grisé F, Kaaret P, Corbel S, Feng H, Cseh D, Tao L. Optical Emission of the Ultraluminous X-Ray Source NGC 5408 X-1: Donor Star or Irradiated Accretion Disk? The Astrophysical Journal 2012; 745(2): 123.

[21] Vinokurov A, Fabrika S, Atapin K. Optical Counterparts of Ultraluminous X-Ray Sources NGC 4559 X-10 and NGC 4395 ULX-1. The Astrophysical Journal 2018; 854 (2): 176.

[22] Schinnerer E. The Circumnuclear Starburst in NGC 7552: First Results from Near-Infrared Spectral Synthesis. The Astrophysical Journal 1997; 488 (1): 174–194.

[23] Tully RB, Fisher JR. Book-Review - Nearby Galaxies Atlaz. Science 1988; 239: 926.

[24] Durret F, Bergeron J. Long slit spectroscopy of emission line galaxies. I. The sample. Astronomy and Astrophysics Supplement Series 1988; 5: 273–297.

[25] Liu JF, Bregman JN. Ultraluminous X-Ray Sources in Nearby Galaxies from ROSAT High Resolution Imager Observations I. Data Analysis. The Astrophysical Journal Supplement Series 2005; 157(1): 59–125.

[26] Luangtip W. A deficit of ultraluminous X-ray sources in luminous infrared galaxies. MNRAS 2015; 446(1): 470–492.

[27] Evans PA. Methods and results of an automatic analysis of a complete sample of Swift-XRT observations of GRBs. MNRAS 2009; 397(3): 1177–1201.

[28] Tsygankov SS, Mushtukov AA, Suleimanov VF and Poutanen J. Propeller effect in action in the ultraluminous accreting magnetar M82 X-2. MNRAS 2016; 457(1): 1101–1106.

[29] Song X. The hunt for pulsating ultraluminous X-ray sources. MNRAS 2020; 491(1): 1260–1277.

[30] Allak S. Detection of 125.5-day optical periodic modulation of the neutron star M51 ULX-8. MNRAS 2022; 517(3): 3495–3504.

[31] Schlafly EF and Finkbeiner DP. Measuring Reddening with Sloan Digital Sky Survey Stellar Spectra and Recalibrating SFD. The Astrophysical Journal 2011; 737(2): 103

[32] Remillard RA and McClintock JE. X-Ray Properties of Black-Hole Binaries. Annual Review of Astronomy and Astrophysics 2006; 44(1): 49–92.

[33] Feng H, Kaaret P. Spectral States and Evolution of Ultraluminous X-Ray Sources. The Astrophysical Journal 2009; 696(2): 1712–1726.

[34] Jin J, Feng H, Kaaret P. Transition to the Disk Dominant State of a New Ultraluminous X-ray Source in M82. The Astrophysical Journal 2010; 716(1): 181–186.

[35] Koliopanos F, Vasilopoulos G, Buchner J, Maitra C, Haberl F. Investigating ULX accretion flows and cyclotron resonance in NGC 300 ULX1. Astronomy and Astrophysics 2019; 621.

[36] Bressan A. PARSEC: stellar tracks and isochrones with the PAdova and TRieste Stellar Evolution Code. MNRAS 2012; 427(1): 127–145.

[37] Hunt Q. Calibrating X-Ray Binary Luminosity Functions via Optical Reconnaissance. I. The Case of M83. The Astrophysical Journal 2021; 912(1): 31.

[38] Allak S. Comprehensive X-ray and multiwavelength study of ULXs in NGC 1566. MNRAS 2024; 527(3): 556–7567.

[39] Allak S. The first glimpse of ULXs through the near-infrared images captured by the JWST. MNRAS 2024; 527(2): 2599–2611.

[40] Allak S. New transient ULX candidate in NGC 4254: evidence of circumbinary disc? MNRAS 2023; 526(4): 5765–5776.

COMPARATIVE PERFORMANCE STUDY OF A MODIFIED GASOLINE ENGINE WITH THROTTLE-VALVE-DRIVEN MECHANICAL HYDROGEN INJECTOR

Ahmet GÖRGÜLÜ [1], *

[1] Eti Gida Sanayi ve Ticaret A.Ş., Eti Plaza, Hoşnudiye Mah. K.Mahmut Pehlivan Cad. No:11, 26110, Tepebaşı, Eskişehir, Turkey
agorgulu1375@gmail.com 0000-0002-7549-1524

Abstract

In this study, a single-cylinder, air-cooled, 4-stroke, spark-ignited internal combustion engine was modified to operate with both gasoline and gas-phase hydrogen. The engine cylinder cover was redesigned, and an enhanced mechanical hydrogen injector was attached to it. Measurement devices capable of capturing all critical test parameters for comparison purposes were integrated into the test engine. Additionally, all necessary safety equipment was adapted to ensure the safe delivery of hydrogen to the engine. The engine was initially tested with gasoline, and values for engine torque, brake power, specific fuel consumption, TE, and VE were recorded at air throttle openings of 20º to 90º in 10º increments and speeds ranging from 1000 to 3900 rpm. The same parameters were then measured using gas-phase hydrogen. In the experiments conducted with gasoline, optimal performance was achieved at air throttle openings of 60º to 90º and engine speeds of 2350 to 3400 rpm. In the experiments using hydrogen, the most favorable values were observed between 1300 and 1775 rpm at a 30º air throttle opening. When comparing the performance of gasoline and hydrogen in the same engine, results indicated that using gaseous hydrogen led to a 79.54% reduction in engine power and a 73.44% decrease in engine torque. This reduction is considered typical, given that the lower calorific value of hydrogen in the gas phase, at the same pressure and temperature (1 bar, 20 ºC), is approximately 0.010 MJ/l, compared to around 34 MJ/l for gasoline. During testing, issues such as knocking, pre-ignition, and backfire typically associated with intake manifold injection did not occur. No prior studies have employed a direct hydrogen injection method into the combustion chamber with a mechanically activated Hydrogen Injector driven by the intake valve.

1. INTRODUCTION

Hydrogen-fueled engines are attractive due to their lower exhaust emissions compared to fossil-fuel internal combustion engines. Hydrogen offers advantages in Spark Ignition (SI) engines because of its low ignition temperature, wide flammability range in fuel/air mixtures, and high combustion speed. It is considered a clean fuel, producing no Carbon Dioxide (CO_2), Unburned Hydrocarbons (UHC), and generating lower Nitrogen oxide (NO_x) emissions. However, pre-mixing hydrogen with intake air before feeding it into the combustion chamber can cause backfiring and knocking [1]. Engine output power is limited by the low calorific value per unit volume of gaseous hydrogen, especially at low pressures [2]. Additionally, as hydrogen does not naturally exist as a molecular element, its production is costly, requiring extraction from various sources through different methods [3]. The total carbon emissions from hydrogen production also make Life Cycle Analysis (LCA) critically important depending on production methods [4]. Hydrogen production from renewable energy sources is significant in terms of emissions reduction [5],[6],[7]. One major obstacle to widespread hydrogen use as a fuel is its high

production cost, which can range from 1.4 to 8.4 USD/kg when including carbon capture processes [8]. Another significant challenge in replacing fossil-fueled vehicles with hydrogen-fueled vehicles lies in hydrogen storage systems, which require high safety standards, substantial energy for storage, and lightweight yet high-capacity tanks. Current technologies allow for only about 19.4% of a storage tank's weight to be hydrogen [9]. Fossil-fueled Internal Combustion Engines (ICE) produce Carbon Monoxide (CO), NO_x, UHC, Particulate Matter (PM), and Greenhouse Gases (GHG) as combustion products [10]. Compared to gasoline engines, Hydrogen-fueled Internal Combustion Engines (H_2ICE) operate more efficiently with lean mixtures due to hydrogen's high energy content. Hydrogen also has a higher flame speed, lower ignition energy (0.02 MJ), and a higher ignition temperature than other fuels [11]. Due to its high diffusivity, low ignition energy, and high flame speed relative to gasoline and methane, hydrogen is well-suited for SI engines [12]. Hydrogen use in SI engines can take several forms: injection into the intake manifold, cold hydrogen injection directly into the combustion chamber, or use in combination with gasoline and other fuels [8]. Hydrogen can also be used in Compression Ignition (CI) engines, where different injector types are employed to introduce high-pressure hydrogen into the cylinder [13]. Thus, in CI engines, injector design is as critical as engine structure [14]. Hydrogen use in CI engines has been shown to reduce CO_2, CO, HC, and smoke levels by over 50% under optimal conditions. Another approach involves using liquid hydrogen, which requires minimal modification to conventional ICEs. In this system, liquefied hydrogen is converted to cold hydrogen gas in an expansion chamber before injection into the combustion chamber. Cold hydrogen injection reduces NO_x emissions and prevents pre-ignition [15],[16].

2. MATERIALS AND METHODS

In this study, a single-cylinder, air-cooled gasoline engine was modified to operate with both gasoline and gaseous fuels. Various measuring devices and sensors were installed on the engine to monitor and record experimental data. The hydrogen gas used in the experiments was supplied in 150-bar pressure tubes, with a pressure-regulating device attached to ensure consistent pressure during testing. Pressure gauges (Figure 1, A-B) display both the gas pressure within the tube and the regulated pressure supplied to the engine. A flow meter connected to the pressure regulator allows measurement of the gas flow rate fed to the engine. To prevent hazards from backfiring in the combustion chamber, a water safety system was installed after the flow meter. Both gasoline and hydrogen gas were tested as fuels in the same engine, with comparisons made between engine performance and efficiency for each fuel type. Intake air to the engine was measured using a tank-orifice setup (Figure 1). For gasoline testing, Specific Fuel Consumption (SFC) was measured with a scaled glass tube and a 3-way valve connected to the fuel line (Figure 1, B-F). A water brake mechanism and torque meter, linked to the engine crankshaft, were used to measure engine brake power and torque, while engine speed was monitored via a tachometer connected to the same system. To prevent overheating, deformation, or jamming of the hydrogen injector, its body was cooled with externally supplied mains water. Additionally, the temperatures of the engine oil and exhaust gases were monitored with separate thermometers (Figure 1, U). Figure 1 provides a detailed schematic of the experimental setup. To address premature ignition issues with hydrogen, as noted in the literature, a novel solution was developed. In this approach, the engine cylinder head was redesigned, and a specialized injector was added to directly inject hydrogen into the combustion chamber [17].
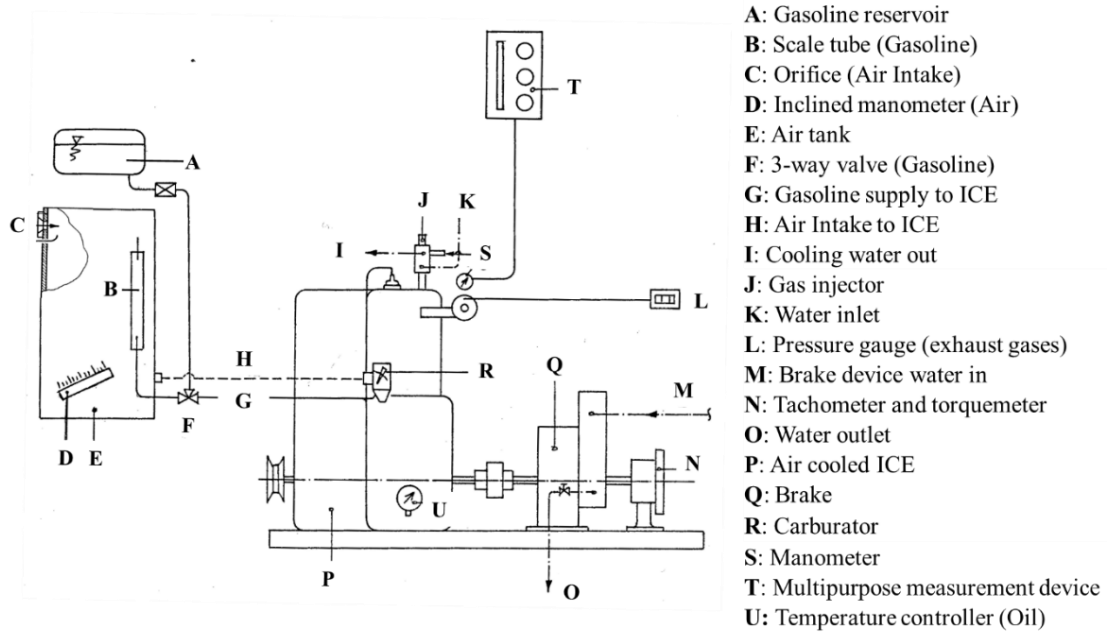
A: Gasoline reservoir
B: Scale tube (Gasoline)
C: Orifice (Air Intake)
D: Inclined manometer (Air)
E: Air tank
F: 3-way valve (Gasoline)
G: Gasoline supply to ICE
H: Air Intake to ICE
I: Cooling water out
J: Gas injector
K: Water inlet
L: Pressure gauge (exhaust gases)
M: Brake device water in
N: Tachometer and torquemeter
O: Water outlet
P: Air cooled ICE
Q: Brake
R: Carburator
S: Manometer
T: Multipurpose measurement device
U: Temperature controller (Oil)

Figure 1. Schematic view of the experimental setup

In this study, a single-cylinder internal combustion, 4-stroke, air-cooled gasoline engine (Table 1) was modified and the compression ratio was increased from 1/7 to 1/8. A specially designed mechanical injector that would directly inject hydrogen in the gas phase into the combustion chamber was connected to the cylinder head of the engine (Figure 2). The technical specifications of the engine used in the experiments are given in Table 1.

Table 1. The technical specifications of the test engine

Specification	Unit
Producer Name and Model	Briggs Stratton, 1972 (USA)
Number of the Piston	1
Piston Diameter and Stroke (mm)	66.45- 66.68
Compression Rate	1/8
Power (Kw)	3 (3000 rpm)
Engine Speed (rpm)	1000-4500
Cooling	Air
Valve Type	L
Ignition Type	SI
Stroke Number	4

A: Single cylinder ICE
B: Top View of ICE without cylinder head
C: Cylinder head with Injector
D: Cylinder head, injector and the gasket
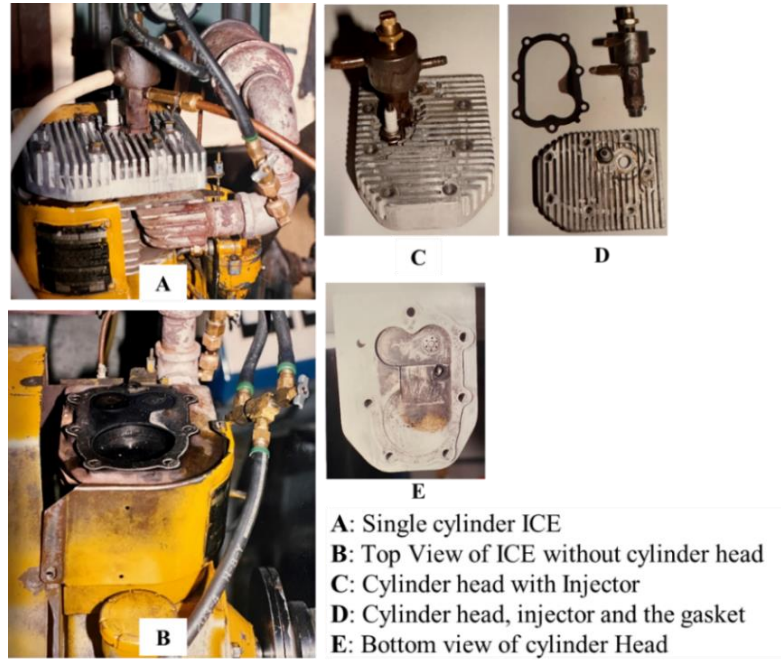**E**: Bottom view of cylinder Head

Figure 2. Single piston ICE, cylinder head, ınjector, and the gasket

The injector is mounted on the engine cylinder head and driven by the intake valve (Figure 2). The injector's timing for intake valve opening can be adjusted by modifying its connection height to the cylinder head (Figure 3, H-K). A pressure spring (Figure 3, I) closes the injector, and the spring pressure can be fine-tuned to completely seal the hydrogen path (Figure 3, J). To ensure complete closure of the gas path, the valve in the injector (Figure 3, A) blocks both the hydrogen inlet (Figure 3, D) and the gas flow channels (Figure 3, C). A water jacket (Figure 3, G) surrounds the upper part of the injector to prevent blockage due to engine heat. By adjusting the injector's height concerning the intake valve, the timing of hydrogen injection can be optimized, thereby eliminating early ignition issues noted in the literature through testing different height settings.

A: Injector Valve
B: Gas Injection Holes
C: Gas Feeding
D: Hydrogen Inlet
E: Cooling Water In
F: Cooling Water Out
G: Cooling Jacket
H: Adjusting Bolt
I: Spring
J: Spring Force Adjusting Screw
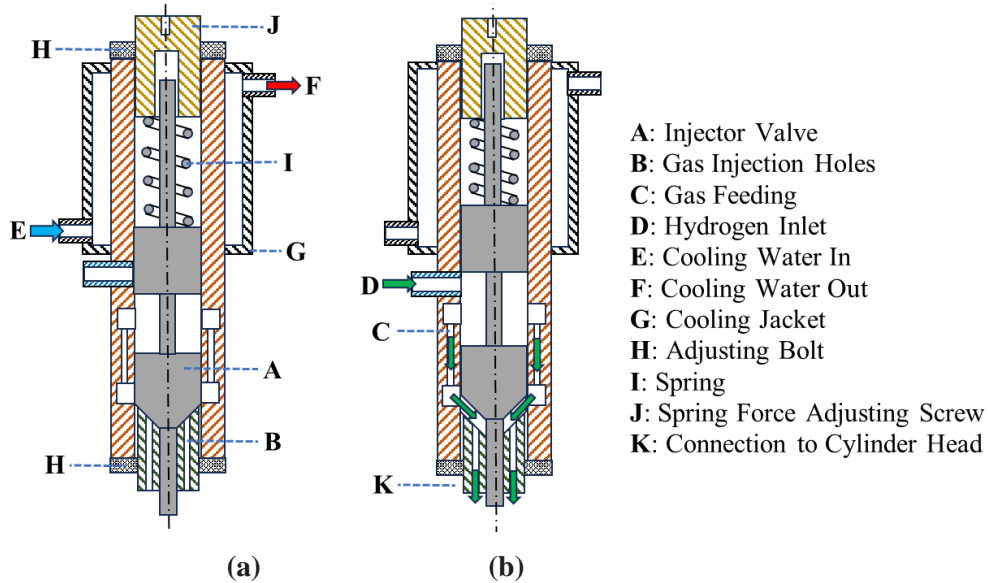**K**: Connection to Cylinder Head

(a) **(b)**

Figure 3. Hydrogen injector and working principle (a: Closed, b: Open)

A mechanically actuated hydrogen injector (MAHI) was designed and implemented for direct hydrogen injection into the combustion chamber. The closed (Figure 3, a) and open (Figure 3, b) positions of the injector are shown schematically in Figure 3. The injector is driven by the intake valve (Figure 4, B); it opens when the intake valve opens (Figure 4, b) and closes when the intake valve closes, aided by the spring mechanism (Figure 4, a).
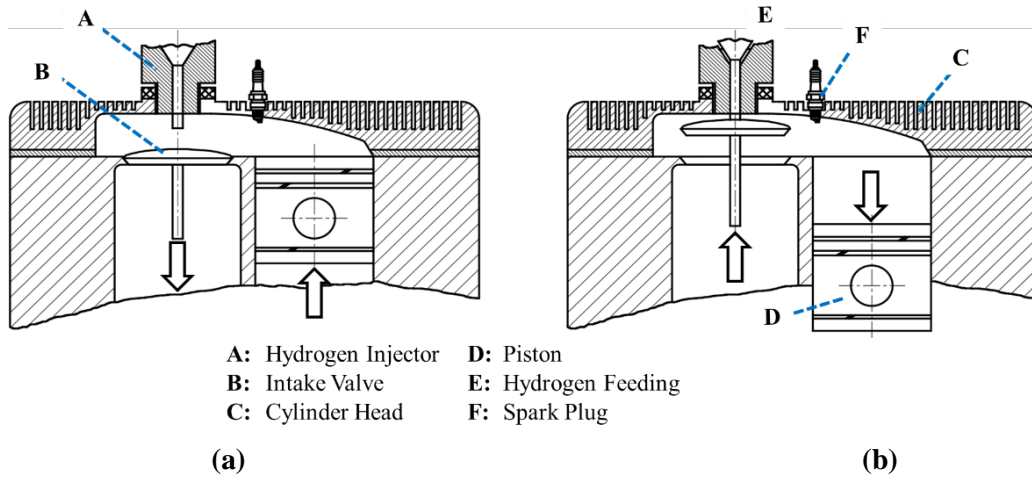

A: Hydrogen Injector   D: Piston
B: Intake Valve   E: Hydrogen Feeding
C: Cylinder Head   F: Spark Plug

(a)   **(b)**

Figure 4. The cross-section of the combustion chamber and injection principle.

The final design and main components of the hydrogen injector, shown in Figure 3 as a technical drawing, are presented in Figure 5. The injector consists of five main parts: the body, which attaches to the cylinder head (Figure 5, D); the injector valve, which opens and closes the hydrogen flow path (Figure 5, A); the spring, which keeps the valve in the closed position (Figure 5, I); the screw for adjusting the spring pressure (Figure 5, J); and the nipple that facilitates hydrogen entry (Figure 5, D).
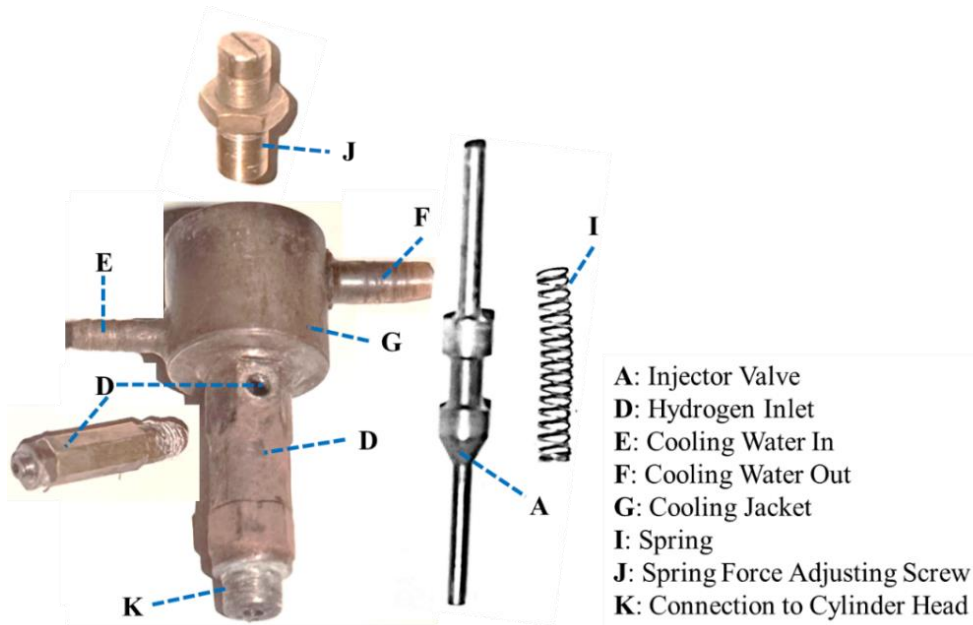

A: Injector Valve
D: Hydrogen Inlet
E: Cooling Water In
F: Cooling Water Out
G: Cooling Jacket
I: Spring
J: Spring Force Adjusting Screw
K: Connection to Cylinder Head

Figure 5. Mechanically Activated Hydrogen Injector and main parts

The modified engine was first tested with gasoline, and all experimental data were recorded. During testing, the combustion air throttle angle was adjustable from 20º to 90º in 10º increments. The fuel

quantity entering the engine was varied at each throttle angle, and the engine was tested at speeds ranging from 1000 to 4100 rpm. For each combination of throttle angle and engine speed, data on brake torque, brake power, specific fuel consumption, combustion airflow, exhaust gas temperature, and engine oil temperature were continuously recorded. Each experimental condition was repeated three times, and the average values were tabulated. Using the experimental data, engine TE and VE were also calculated. The recorded and calculated data were then compared to assess the engine's performance when operating with gasoline versus hydrogen.

3. RESULTS AND DISCUSSION

3.1. Experimental Analysis and Results of GICE

To establish a baseline with gasoline for the modified engine, experiments were conducted at throttle openings of 30º-90º and engine speeds between 2000 and 3900 rpm, with all experimental data recorded. Key parameters such as brake torque, combustion airflow rate, and fuel flow rate were measured at various throttle angles and engine speeds using torque and speed measurement devices connected to the engine crankshaft (Figure 1, Q-N). Additional data, including exhaust gas temperature and engine oil temperature, were also recorded. Based on the collected data, performance metrics such as engine brake power, TE, VE, SFC, and excess air coefficient were calculated. In Figure 6, from left to right, the power curves for torque values obtained at engine speeds of 1300-3500 rpm for throttle openings of 30º, 40º, 50º, 60º, 70º, 80º, and 90º are shown.
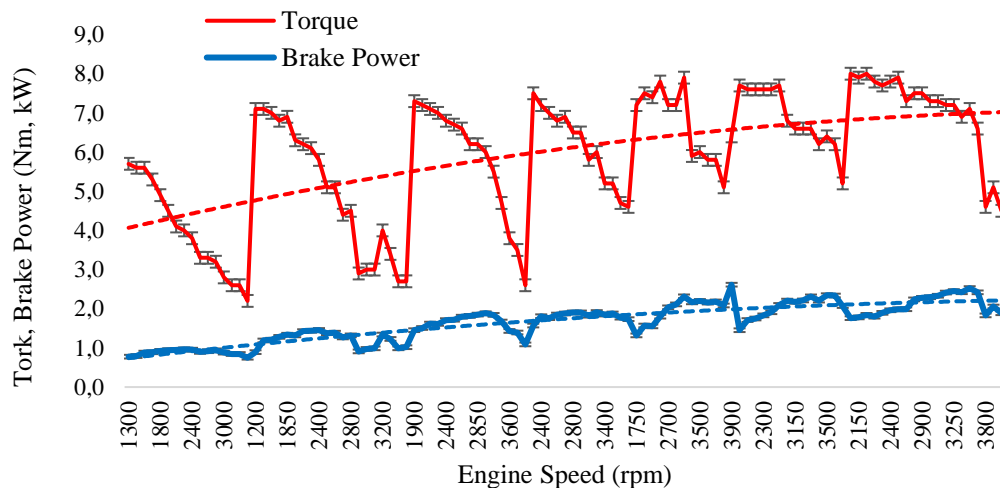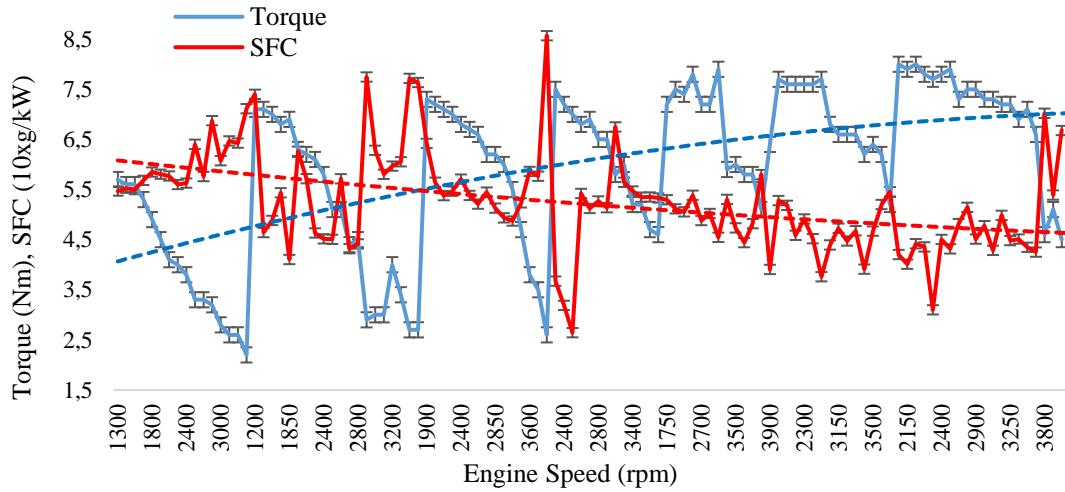

Figure 6. GICE Engine speed, torque, and Brake power

In Figure 6, the peaks in the curves from left to right correspond to the degree of throttle opening (30-90º). The summary table derived from the data tables (Table 2, lines 1, 3, 5, 6, 7) indicates that the engine achieves optimal torque performance at throttle openings of 60º, 80º, and 90º, within the speed range of 2350-2600 rpm.

Table 2. Optimum performance variables of GICE

Test No	Throttle Angle (°)	Engine Speed (rpm)	Torque (Nm)	Brake Power (kW)	SFC (gr/kW)	VE (%)	TE (%)
1	80	2600	7.7	2.10	376.0	22.0	42.8
2	80	3400	6.2	2.21	391.1	21.1	43.3
3	60	2400	7.2	1.81	318.8	25.7	43.6
4	90	3500	6.6	2.42	425.1	19.4	43.7
5	90	3400	7.1	2.53	434.8	19.0	44.6
6	90	2350	7.7	1.89	309.9	21.1	47.0
7	60	2400	7.0	1.76	264.3	31.3	51.1

It was found that TE also reaches high values at the optimum engine torque. The region marked in green in the graph in Figure 6 represents the range where both engine torque and power are at their optimum. The SFC data for the engine operating with gasoline, measured at air throttle openings of 30-90º (9 angles) and engine speeds from 1200 to 3900 rpm, are presented in Figure 7. The graph highlights the experimental conditions where the highest engine torque and the lowest fuel consumption occur. It was determined that the operating conditions that yield optimum engine torque also correspond to the lowest specific fuel consumption, as shown in Figure 7.

Figure 7. GICE Engine speed, torque, SFC

TE and VE values, calculated using fuel consumption, fuel lower heating value, and engine air flow data, are presented in Figure 8. Based on the data summarized in Figure 8 and Table 2, the optimum operating conditions for the engine running on gasoline are found at air throttle openings of 60º, 80º, and 90º, and within the speed range of 2350-2600 rpm. The engine's TE was determined to range from 42.8% to 51.1%, while its VE ranged from 21.1% to 31.3% (Table 2).
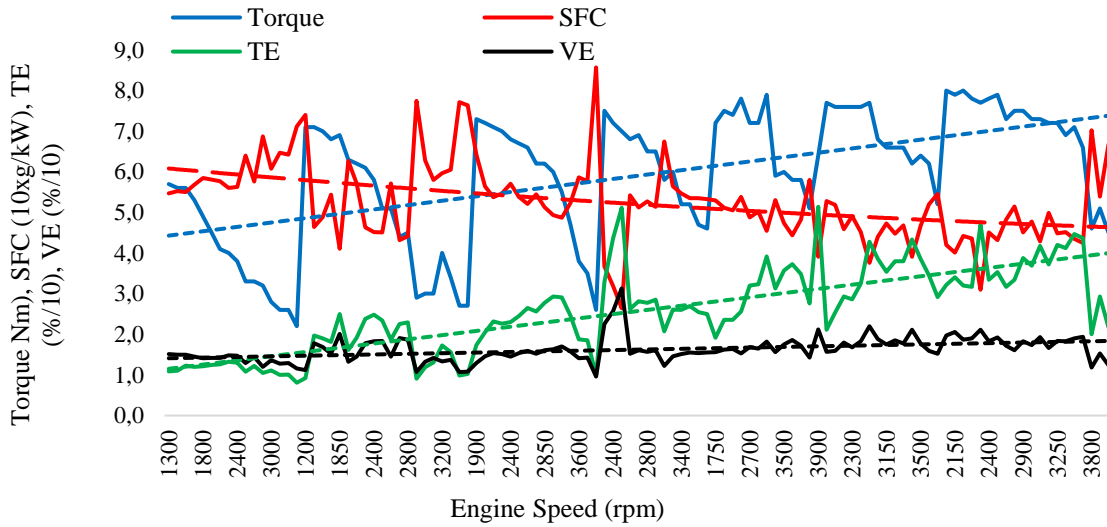
Figure 8. GICE Engine speed, Torque, SFC, TE, VE

In the experiments conducted with gasoline, the most optimal operating conditions were found at air throttle openings of 60º to 90º and engine speeds between 2350 and 3400 rpm. The highest torque of 6.4 Nm was achieved at 90º throttle opening and 3900 rpm, with a brake power of 2.61 kW and a SFC of 390.5 g/kWh. The highest brake power of 1.76 kW was observed at 70º throttle opening and 2100 rpm, with a torque of 8 Nm and an SFC of 420.3 g/kWh. The highest TE of 51.4% was recorded at 70º throttle opening and 3900 rpm, with a torque of 6.4 Nm and a brake power of 2.61 kW. The highest VE of 31.3% was achieved at 60º throttle opening and 2400 rpm, with a torque of 7 Nm, brake power of 1.76 kW, and a TE of 51.1%.

3.2. Experimental Analysis and Results of H$_2$ICE

After the experiments with the modified gasoline engine, which was redesigned to accommodate the hydrogen injector, additional tests were conducted using the direct injection method into the combustion chamber with the specially developed injector (Figure 5). To facilitate comparisons with the gasoline engine, data on engine torque, brake power, specific fuel consumption, TE, and VE were considered. The specially designed mechanical injector (Figure 5) was created to inject hydrogen directly into the combustion chamber. Hydrogen, supplied from a cylinder at 150 bar pressure, was reduced to 0.25 bar by a pressure regulator before being fed into the engine. This pressure was maintained constant throughout the experiments. The injector, which is normally in the closed position due to the spring pressure (Figure 4, a), is mechanically opened by the intake valve (Figure 4, b), and hydrogen at 0.25 bar is injected into the combustion chamber using the suction effect of the piston (Figure 4, b).
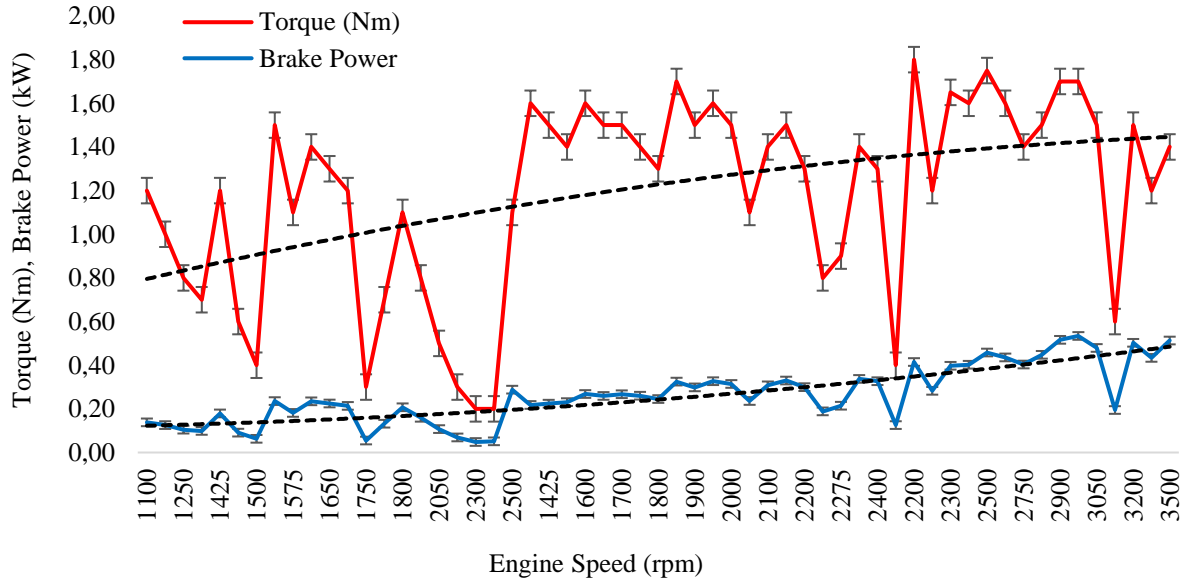
Figure 9. H$_2$ICE Engine speed; Torque, Brake power

In the experiments conducted with hydrogen, Figure 9 shows that the engine produces the highest torque in the range of 2300-2850 rpm at air throttle openings of 20° and 30°, and the highest brake power between 2850-3200 rpm. However, experiments at air throttle openings above 40° were not studied, as the engine exhibited low performance under these conditions. The cause of this was determined to be the insufficient amount of hydrogen fed into the combustion chamber in the gas phase at throttle openings above 40°.
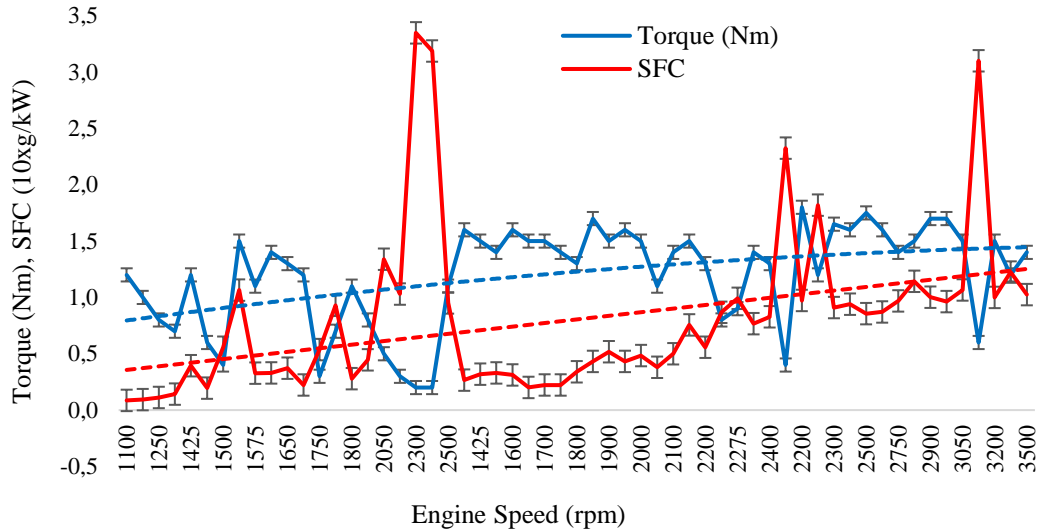

Figure 10. H$_2$ICE Engine speed, torque, SFC

As shown in the summary data in Table 3, the lowest SFC values, in contrast to the maximum torque and power values of the engine, occur in the range of 1350-1800 rpm. The optimum operating conditions are observed at 1300-1775 rpm with 20° and 30° air throttle angles.

Table 3. Optimum performance variables of H$_2$ICE

Test No	Throttle Angle (°)	Engine Speed (rpm)	Torque (Nm)	Brake Power (kW)	SFC (kg/kW)	TE (%)	VE (%)
1	30	1425	1.50	0.224	0.319	9.40	53.07
2	30	1600	1.60	0.268	0.312	9.59	52.23
3	30	1300	1.60	0.218	0.266	11.28	54.05
4	30	1775	1.40	0.260	0.223	13.43	44.71
5	30	1700	1.50	0.267	0.223	13.43	48.06
6	30	1650	1.50	0.259	0.201	14.92	48.81

The VE and TE data obtained by operating the modified engine with hydrogen are given in Figure 11. It is seen from the graphs given in Figure 11 that the optimum operating range of VE and TE occurs in the range of 20 and 30° air throttle angle at 1300-1800 rpm engine speed.
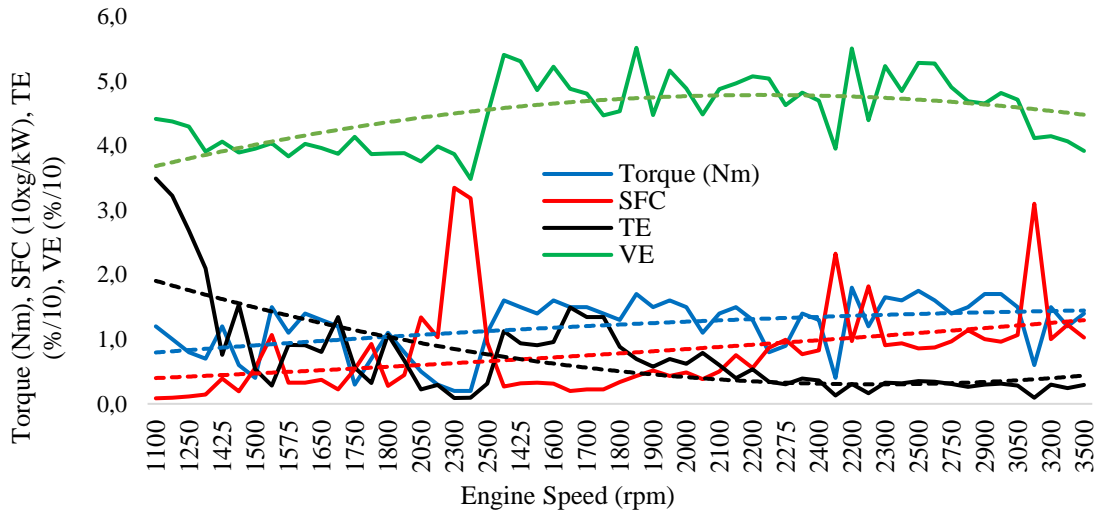

Figure 11. H$_2$ICE Engine speed, torque, SFC, TE, VE

Table 3 shows that under optimum conditions, the VE ranges from 44.71% to 54.05%, while the TE varies between 9.4% and 14.92%. The TE decreases inversely with the increase in VE. This is because the hydrogen/air mixture in the gas phase is limited by an upper bound. In other words, assuming ideal combustion conditions for the engine (piston diameter: 66.45 mm, stroke: 66.68 mm), a theoretical power calculation was made for the 1800 rpm experimental condition (Table 4, line 3). Under hydrogen/air mixture conditions (2 moles H$_2$, 1 mole O$_2$), the theoretical power was calculated to be 0.1473 kW. Given that the measured power for this experimental condition was 0.207 kW, it is evident that the mixture is being supercharged into the combustion chamber. The experimental data corresponding to this theoretical power value is 0.207 kW, as shown in Table 4, line 3. Considering the combustion efficiency, it can be concluded that the engine is operating with rich mixtures and is supercharged. Therefore, the TE is low, while the VE is high.

Table 4. Optimum performance variables of H$_2$ICE

Test No	Throttle Angle (°)	Engine Speed (rpm)	Torque (Nm)	Brake Power (kW)	SFC (kg/kW)	TE (%)	VE (%)
1	30	1425	1.50	0.224	0.319	9.40	53.07
2	30	1600	1.60	0.268	0.312	9.59	52.23
3	20	1800	1.10	0.207	0.279	10.74	38.78
4	30	1300	1.60	0.218	0.266	11.28	54.05
5	20	1700	1.20	0.214	0.223	13.43	38.72
6	30	1775	1.40	0.260	0.223	13.43	44.71
7	30	1700	1.50	0.267	0.223	13.43	48.06
8	30	1650	1.50	0.259	0.201	14.92	48.81

In the experiments conducted with hydrogen, the most optimal values were achieved in the range of 1300-1775 rpm with a 30º air throttle opening. The highest brake power of 0.534 kW was measured at 40º, 3000 rpm, with 1.7 Nm torque, 0.414 kW brake power, and a SFC of 0.93. TE was found to be 34.91% at 20º, 1100 rpm, with 1.2 Nm torque and 0.138 kW brake power. At 30º, 1825 rpm, with 1.7 Nm torque and 0.325 kW brake power, TE was 6.94%, while VE was 55.16%. A summary of the comparison of the key parameters is presented in Table 5.

3.3. Comparative Performance Analysis of GICE and H$_2$ICE

The important performance data obtained as a result of operating the engine with gasoline and hydrogen were compared. The data obtained by using the mechanical injector driven by the intake valve, specific to the engine used in the experiment, are summarized in Table 5. Compared to gasoline, hydrogen's Engine Torque was 25.56%, and Engine Brake Power was 20.46%. TE was 67.92%, and VE was 176%.

Table 5. Comparisons of critical engine parameters.

Specifications	Unit	GICE	H$_2$ICE	%
Torque	Nm	6.4	1.7	26.56
Brake Power	kW	2.61	0.534	20.46
SFC	g/kW	390.5	0.93	
TE	%	51.4	34.91	67.92
VE	%	31.3	55.16	176.2

There have been several studies and applications exploring hydrogen mixing with air before feeding it into the intake manifold and directly injecting it into the combustion chamber at various pressures [18],[19],[20]. However, no studies have utilized MAHI driven by the intake valve, as used in this experimental research. Some studies have explored hydrogen gas compression chambers to increase the hydrogen pressure fed to the intake air, thereby boosting engine power in pressure-augmented H$_2$ICE systems. Additionally, hybrid systems employing both intake manifold and combustion chamber direct injection methods have been proposed to reduce exhaust emissions and enhance engine efficiency [21]. Another study compared gasoline and hydrogen in spark SI engines with timed injections into the intake manifold via electronic control units. This study observed a 19.06% decrease in power but a 3.16% improvement in thermal brake efficiency, along with reduced NO$_x$ emissions at higher engine speeds

[22]. Further research has investigated Laser Ignition (LI) systems for hydrogen-air mixtures, showing that LI engines outperform traditional SI systems. It was reported that hydrogen-fueled engines convert fuel energy into useful work at a 35.74% higher rate than gasoline engines [23],[24]. Another study found that due to the lower calorific value of the hydrogen/air mixture, theoretical engine power was 14% lower, but there was a 95% reduction in NO_x emissions, and 45% brake thermal power could be achieved [25]. These results align with the findings of this study. Hydrogen-fueled engines in transportation systems have been reported to operate at 20-25% efficiency compared to fossil-fueled vehicles, offering advantages such as high energy conversion efficiency, low noise, and zero exhaust emissions, although challenges in storage and infrastructure remain [15] Another study recommended direct injection into the combustion chamber to achieve 45% TE and lower exhaust emissions, stating that this method prevents issues like knocking, pre-ignition, and backfire, which are common in intake manifold injection. However, it also identified technical problems such as high oil consumption and hydrogen leakage into the crankcase during combustion chamber injection [26]. A numerical analysis of the H_2/diesel fuel mixture in compression ignition engines showed that varying hydrogen doses (0.05% to 50% by volume), engine speed (1000-4000 rpm), and air/fuel ratios (10-80%) improved engine performance and reduced emissions [27].

4. CONCLUSION

Experiments were conducted on a modified single-cylinder, 4-stroke, air-cooled spark-ignition (SI) internal combustion engine (ICE) using both gasoline and hydrogen as fuels. The tests were carried out at air throttle angles ranging from 20º to 90º and engine speeds between 1000 and 3900 rpm. When comparing the performance of gasoline and hydrogen on the same engine, it was found that the use of gaseous hydrogen resulted in a significant loss of engine power (79.54%) and torque (73.44%). This reduction is attributed to the lower calorific value of hydrogen in its gaseous phase, which is approximately 0.010 MJ/l at 1 bar and 20ºC, compared to gasoline's calorific value of around 34 MJ/l [28]. During the tests, issues such as knocking, pre-combustion, and backfire commonly encountered when hydrogen is injected into the intake manifold were not observed. Based on these findings, it seems unlikely to achieve the same torque and power with gaseous hydrogen unless the hydrogen pressure is increased within the same cylinder volume. An alternative solution could be to increase the cylinder volume. In these experiments, hydrogen was injected into the combustion chamber at a pressure of 0.25 bar for safety reasons; however, testing with higher hydrogen pressures could provide additional insights.

NOMENCLATURE

ICE: Internal Combustion Engine
CI: Compression Ignition
SI: Spark Ignition
LI: Laser Ignition
UHC: Unburned Hydrocarbons
PM: Particle Materials
GICE: Gasoline-fueled Fueled Internal Combustion Engine

H₂ICE: Hydrogen Fueled Internal Combustion Engine
H₂CIE: Hydrogen Fueled Compression Ignition Engine
H₂SIE: Hydrogen Fueled Spark Ignition Engine
MAHI: Mechanically Activated Hydrogen Injector
SFC: Specific Fuel Consumption
TE: Thermal Efficiency
VE: Volumetric Efficiency
RES: Renewable Energy Sources
HHV: Higher Calorific Value
LHV: Lower Calorific Value
GHG: Greenhouse Gases

CONFLICT OF INTEREST

The author stated that there are no conflicts of interest regarding the publication of this article.

CRediT AUTHOR STATEMENT

Ahmet Görgülü: Formal analysis, Writing-original draft, Visualization, Conceptualization, Validation Investigation, Supervision, Writing-Review and Editing, Funding acqusition.

REFERENCES

[1]   Luo Q he, Sun B gang. Inducing factors and frequency of combustion knock in hydrogen internal combustion engines. Int J Hydrogen Energy 2016;41:16296–305. https://doi.org/10.1016/J.IJHYDENE.2016.05.257.

[2]   Wróbel K, Wróbel J, Tokarz W, Lach J, Podsadni K, Czerwiński A. Hydrogen Internal Combustion Engine Vehicles: A Review. Energies (Basel) 2022;15:8937. https://doi.org/10.3390/en15238937.

[3]   Dash SK, Chakraborty S, Elangovan D. A Brief Review of Hydrogen Production Methods and Their Challenges. Energies (Basel) 2023;16:1141. https://doi.org/10.3390/en16031141.

[4]   Cetinkaya E, Dincer I, Naterer GF. Life cycle assessment of various hydrogen production methods. Int J Hydrogen Energy 2012;37:2071–80. https://doi.org/10.1016/J.IJHYDENE.2011.10.064.

[5]   Herdem MS, Mazzeo D, Matera N, Baglivo C, Khan N, Afnan, et al. A brief overview of solar and wind-based green hydrogen production systems: Trends and standardization. Int J Hydrogen Energy 2024;51:340–53. https://doi.org/10.1016/J.IJHYDENE.2023.05.172.

[6]   Yu M, Wang K, Vredenburg H. Insights into low-carbon hydrogen production methods: Green, blue and aqua hydrogen. Int J Hydrogen Energy 2021;46:21261–73. https://doi.org/10.1016/J.IJHYDENE.2021.04.016.

[7]   Zainal BS, Ker PJ, Mohamed H, Ong HC, Fattah IMR, Rahman SMA, et al. Recent advancement and assessment of green hydrogen production technologies. Renewable and Sustainable Energy Reviews 2024;189:113941. https://doi.org/10.1016/J.RSER.2023.113941.

[8]   Mulky L, Srivastava S, Lakshmi T, Sandadi ER, Gour S, Thomas NA, et al. An overview of hydrogen storage technologies – Key challenges and opportunities. Mater Chem Phys 2024;325:129710. https://doi.org/10.1016/J.MATCHEMPHYS.2024.129710.

[9]   Cui X, Su H-Y, Chen R, Yu L, Dong J, Ma C, et al. Room-temperature electrochemical water–gas shift reaction for high purity hydrogen production. Nat Commun 2019;10:86. https://doi.org/10.1038/s41467-018-07937-w.

[10]   Reitz RD. Directions in internal combustion engine research. Combust Flame 2013;160:1–8. https://doi.org/10.1016/J.COMBUSTFLAME.2012.11.002.

[11]   Schlapbach L, Züttel A. Hydrogen-storage materials for mobile applications. Nature 2001;414:353–8. https://doi.org/10.1038/35104634.

[12]   Bradley D, Lawes M, Liu K, Verhelst S, Woolley R. Laminar burning velocities of lean hydrogen–air mixtures at pressures up to 1.0 MPa. Combust Flame 2007;149:162–72. https://doi.org/10.1016/J.COMBUSTFLAME.2006.12.002.

[13]   Naber JD, Siebers DL. Hydrogen combustion under diesel engine conditions. Int J Hydrogen Energy 1998;23:363–71. https://doi.org/10.1016/S0360-3199(97)00083-9.

[14]   Gomes Antunes JM, Mikalsen R, Roskilly AP. An experimental study of a direct injection compression ignition hydrogen engine. Int J Hydrogen Energy 2009;34:6516–22. https://doi.org/10.1016/J.IJHYDENE.2009.05.142.

[15]   Hosseini SE, Butler B. An overview of development and challenges in hydrogen powered vehicles. Int J Green Energy 2020;17:13–37. https://doi.org/10.1080/15435075.2019.1685999.

[16]   Gurz M, Baltacioglu E, Hames Y, Kaya K. The meeting of hydrogen and automotive: A review. Int J Hydrogen Energy 2017;42:23334–46. https://doi.org/10.1016/J.IJHYDENE.2017.02.124.

[17]   Görgülü A. Hidrojenin Yakıt Olarak İçten Yanmalı Motorlarda Kullanımı ve Diğer Yakıtlarla Mukayesesi. Yök Tez 1994:1–261. https://tez.yok.gov.tr/UlusalTezMerkezi/tezDetay.jsp?id=CY4OWm88FIK9HX-Q31ydNg&no=CY4OWm88FIK9HX-Q31ydNg (accessed November 1, 2024).

[18]   He L, Jingyuan L, Xiumin Y, Mengliang L, Tian Y. Numerical Study on Combustion and Emission Characteristics of a PFI Gasoline Engine with Hydrogen Direct-Injection. Energy Procedia 2019;158:1449–54. https://doi.org/10.1016/J.EGYPRO.2019.01.348.

[19]   Boretti A. Hydrogen internal combustion engines to 2030. Int J Hydrogen Energy 2020;45:23692–703. https://doi.org/10.1016/J.IJHYDENE.2020.06.022.

[20]   Hari Ganesh R, Subramanian V, Balasubramanian V, Mallikarjuna JM, Ramesh A, Sharma RP. Hydrogen fueled spark ignition engine with electronically controlled manifold injection: An experimental study. Renew Energy 2008;33:1324–33. https://doi.org/10.1016/J.RENENE.2007.07.003.

[21]   White CM, Steeper RR, Lutz AE. The hydrogen-fueled internal combustion engine: a technical review. Int J Hydrogen Energy 2006;31:1292–305. https://doi.org/10.1016/J.IJHYDENE.2005.12.001.

[22]   Navale SJ, Kulkarni RR, Thipse SS. An experimental study on performance, emission and combustion parameters of hydrogen fueled spark ignition engine with the timed manifold

injection system. Int J Hydrogen Energy 2017;42:8299–309. https://doi.org/10.1016/J.IJHYDENE.2017.01.059.

[23] Nieminen J, Dincer I. Comparative exergy analyses of gasoline and hydrogen fuelled ICEs. Int J Hydrogen Energy 2010;35:5124–32. https://doi.org/10.1016/J.IJHYDENE.2009.09.003.

[24] Verhelst S, Wallner T. Hydrogen-fueled internal combustion engines. Prog Energy Combust Sci 2009;35:490–527. https://doi.org/10.1016/J.PECS.2009.08.001.

[25] Verhelst S, Sierens R. Aspects concerning the optimisation of a hydrogen fueled engine. Int J Hydrogen Energy 2001;26:981–5. https://doi.org/10.1016/S0360-3199(01)00031-3.

[26] Stępień Z. A Comprehensive Overview of Hydrogen-Fueled Internal Combustion Engines: Achievements and Future Challenges. Energies (Basel) 2021;14:6504. https://doi.org/10.3390/en14206504.

[27] Ghazal OH. Performance and combustion characteristic of CI engine fueled with hydrogen enriched diesel. Int J Hydrogen Energy 2013; 38:15469–76. https://doi.org/10.1016/j.ijhydene.2013.09.037.

[28] Habib MA, Abdulrahman GAQ, Alquaity ABS, Qasem NAA. Hydrogen combustion, production, and applications: A review. Alexandria Engineering Journal 2024;100:182–207. https://doi.org/10.1016/J.AEJ.2024.05.030.

ERRATUM

Erratum to: End-to-End Automatic Music Transcription of Polyphonic Qanun and Oud Music Using Deep Neural Network

In the article titled "End-to-End Automatic Music Transcription of Polyphonic Qanun and Oud Music Using Deep Neural Networks," **published in the third issue of the 25th volume (Volume: 25 / Number: 3 / September – 2024)** of the Eskişehir Technical University Journal of Science and Technology A - Applied Sciences and Engineering in 2024, the corresponding author included incomplete information regarding the institutional affiliations and contact details. This oversight may require clarification to ensure proper attribution and communication.

Erratum Statement: In addition to the contact details and institutional affiliations of the corresponding author, Emin Germen, as presented in the article mentioned above, the following correction is hereby noted:

[1] Electrical & Electronics Engineering Dept. Engineering Faculty Eskisehir Technical University, Eskişehir, Türkiye
egermen@eskisehir.edu.tr

[2] MIAM Center of Advanced Studies in Music, State Conservatory, Istanbul Technical University, Istanbul, Türkiye
germen20@itu.edu.tr

This amendment serves to ensure the accuracy of the information provided.